
Doctoral Dissertations

Student Theses and Dissertations

Fall 2017

Experimental and computational investigation of multi-principal element alloys

Mohsen Beyramali Kivy

Follow this and additional works at: https://scholarsmine.mst.edu/doctoral_dissertations



Part of the [Materials Science and Engineering Commons](#)

Department: **Materials Science and Engineering**

Recommended Citation

Beyramali Kivy, Mohsen, "Experimental and computational investigation of multi-principal element alloys" (2017). *Doctoral Dissertations*. 2739.

https://scholarsmine.mst.edu/doctoral_dissertations/2739

This thesis is brought to you by Scholars' Mine, a service of the Missouri S&T Library and Learning Resources. This work is protected by U. S. Copyright Law. Unauthorized use including reproduction for redistribution requires the permission of the copyright holder. For more information, please contact scholarsmine@mst.edu.

EXPERIMENTAL AND COMPUTATIONAL INVESTIGATION OF
MULTI-PRINCIPAL ELEMENT ALLOYS

by

MOHSEN BEYRAMALI KIVY

A DISSERTATION

Presented to the Faculty of the Graduate School of the
MISSOURI UNIVERSITY OF SCIENCE AND TECHNOLOGY

In Partial Fulfillment of the Requirements for the Degree

DOCTOR OF PHILOSOPHY
in
MATERIALS SCIENCE AND ENGINEERING

2017

Approved:
Mohsen Asle Zaeem, Advisor
Joseph W. Newkirk
Jeffrey D. Smith
Caizhi Zhou
Julia E. Medvedeva

© 2017

Mohsen Beyramali Kivy

All Rights Reserved

PUBLICATION DISSERTATION OPTION

This dissertation consists of the following five papers which have been published or will be submitted for publications as follows:

Paper I: Pages 14-41 “Investigating phase formations in cast AlFeCoNiCu high entropy alloys by combination of computational modeling and experiments” has been published in *Materials & Design* 127 (2017) 224-232.

Paper II: Pages 42-56 “Generalized stacking fault energies, ductilities and twinnabilities of CoCrFeNi-based face-centered cubic high entropy alloys” has been published in *Scripta Materialia* 139 (2017) 83-86.

Paper III: Pages 57-72 “Current capabilities in thermodynamic calculations of phase diagrams of high entropy alloys” has been prepared for submission to *CALPHAD* journal (2017).

Paper IV: Pages 73-83 “Investigation of interstitial carbon impact in microstructures of $\text{Al}_x\text{CoCrFeNiCu}$ ($x=0.3, 1.5, 2.8$) high entropy alloys” has been prepared for submission to *Metals* journal (2017).

Paper V: “Effect of alloying elements on unstable and intrinsic stacking fault energies and phase transformations of Fe-Mn-Si-Al-C high strength steel” has been prepared for submission to *Physica B: Condensed Matter* (2017); this paper has been included in the appendix A of this dissertation.

ABSTRACT

Multi-principal element (MPE) alloys, unlike traditional alloys, consist of five or more principal elements with near equi-atomic compositions creating a large new compositional space for exploring new alloy possibilities. However, designing MPE alloys with the desired phases, microstructures and properties is a challenging task, and there is a demand for basic research for a better understanding of structure-processing-property relations in these alloys.

In this Ph.D. research, different computational models and experiments were integrated to study phase formations, and mechanical properties of different MPE alloys. Density functional theory (DFT) and *ab initio* molecular dynamics (AIMD) simulations were used to determine crystal structures, phase stability, and plastic deformation mechanisms. A modified thermodynamic approach was developed to calculate the phase diagrams of MPE alloys, and the accuracy of this approach was tested against commercial software. Experimental casting and characterization, and literature data were used to validate modeling predictions.

The phase diagram calculations of AlFeCoNiCu HEA showed coexistence of two phases at room temperature and stabilization of one phase above 1070 K at the equiatomic composition. The characterization experiments confirmed the crystal structures and composition of phases. To investigate the plastic deformation mechanisms and ductilities of CoCrFeNi-based HEAs, unstable and intrinsic stacking fault and unstable twinning energies were determined by DFT calculations. Finally, the effects of interstitial carbon on the phase formations in Al_xFeCoCrNiCu HEAs were investigated, showing formation of different possible carbides and inter-granular graphite.

ACKNOWLEDGMENTS

I would like to start by thanking my Advisor, Dr. Mohsen Asle Zaeem. He patiently helped me to learn how to conduct scientific research and become a productive graduate student. Also, he has been a great role model to me to pursue excellence in teaching and research.

I would like to thank my Ph.D. dissertation committee members for their sincere help and suggestions during my Ph.D. work. They were very encouraging, understanding, supportive and always available to help me whenever I had any questions. I also appreciate everything I have learned from my committee members in the classroom.

I would like to thank my friends, my colleagues and the faculty and staff in the Department of Materials Science and Engineering who have helped me to achieve my research goals during my Ph.D. studies.

Finally, I would like to thank my family, who has totally supported me throughout my entire studies. My especial appreciation goes to my wife, Caitlin, who has always had faith in my abilities and has supported me through my Ph.D. study.

TABLE OF CONTENTS

	Page
PUBLICATION DISSERTATION OPTION	iii
ABSTRACT	iv
ACKNOWLEDGMENTS	v
LIST OF ILLUSTRATIONS	ix
LIST OF TABLES	xi
 SECTION	
1. INTRODUCTION	1
1.1. CURRENT STATE OF THE ART OF MPE ALLOYS	3
1.1.1. Selection of Principal Elements	5
1.1.2. Manufacturing Methods	7
1.2. MODELING OF MPE ALLOYS	8
1.2.1. Phase Diagram Calculations	8
1.2.2. Atomistic Simulation (Molecular Dynamics)	9
1.2.3. Electronic Scale Simulation (First Principle)	10
2. RESEARCH OBJECTIVES AND IMPACT	12
 PAPER	
I. INVESTIGATING PHASE FORMATIONS IN CAST AlFeCoNiCu HIGH ENTROPY ALLOYS BY COMBINATION OF COMPUTATIONAL MODELING AND EXPERIMENTS	14
ABSTRACT	14
1. INTRODUCTION	15
2. METHODS AND PROCEDURES	20

2.1.	AB INITIO MOLECULAR DYNAMICS.....	20
2.2.	PHASE DIAGRAM CALCULATION	21
2.3.	CASTING AND CHARACTERIZATION	23
3.	RESULTS AND DISCUSSIONS.....	24
3.1.	CRYSTAL STRUCTURES AND PHASES DETERMINED BY AB INITIO MOLECULAR DYNAMICS SIMULATIONS	24
3.2.	PHASE DIAGRAMS OF AlCoFeNiCu	26
3.3.	PHASES AND MICROSTRUCTURES	30
4.	CONCLUSION.....	35
	ACKNOWLEDGEMENT.....	36
	REFERENCES	36
II.	GENERALIZED STACKING FAULT ENERGIES, DUCTILITIES, AND TWINNABILITIES OF CoCrFeNi-BASED FACE-CENTERED CUBIC HIGH ENTROPY ALLOYS	42
	ABSTRACT.....	42
	ACKNOWLEDGMENTS.....	53
	REFERENCES	53
III.	CURRENT CAPABILITIES IN THERMODYNAMIC CALCULATIONS OF PHASE DIAGRAMS OF HIGH ENTROPY ALLOYS	57
	ABSTRACT.....	57
1.	INTRODUCTION	57
2.	METHODOLOGY	59
3.	RESULTS AND DISCUSSION	62
4.	CONCLUSION.....	69

ACKNOWLEDGMENTS.....	69
REFERENCES	70
IV. INVESTIGATION OF INTERSTITIAL CARBON IMPACT IN MICROSTRUCTURES OF $Al_xCoCrFeNiCu$ ($X=0.3, 1.5, 2.8$) HIGH ENTROPY ALLOYS	73
ABSTRACT	73
1. INTRODUCTION	73
2. METHODOLOGY	75
3. RESULTS AND DISCUSSION.....	76
REFERENCES	82
SECTION	
3. SUMMARY, CONCLUSION, AND RECOMMENDATIONS FOR FUTURE WORK	84
APPENDICES	
A. EFFECT OF ALLOYING ELEMENTS ON TWO-STAGE PHASE TRANSFORMATION IN Fe-Mn-Si-Al-C ADVANCED HIGH STRENGTH STEEL.....	87
B. DETAILS OF FIRST PRINCIPLES CALCULATIONS AND SUPPLEMENTAL INFORMATION	105
BIBLIOGRAPHY.....	114
VITA	121

LIST OF ILLUSTRATIONS

SECTION	Page
Figure 1.1.	The number of occurrences of different phases of 648 HEAs reported in Ref. [1]. 4
Figure 1.2.	(a) Fracture toughness-yield strength profile from Ref. [20], and (b) strength-ductility profiles from Ref. [21], for different pure metals and metallic alloys including HEAs. 5
PAPER I	
Figure 1.	Schematic illustration of AlFeCoNiCu bcc lattice distortion. 17
Figure 2.	Calculated formation energies of (a) selected fcc supercell crystals and (b) selected bcc supercell crystals with different compositions at zero K... 25
Figure 3.	Calculated formation energy for equiatomic AlFeCoNi, FeCoCu and AlFeCoNiCu systems at 0 K, 873 K and 1,073 K. 26
Figure 4.	Molar fraction of the stable phases as a function of temperature for equiatomic composition of AlFeCoNiCu HEA. 27
Figure 5.	Calculated phase diagram of Al _x FeCoNiCu. 28
Figure 6.	Calculated phase diagrams of AlFeCoNiCu with changing molar fractions of different elements.. 29
Figure 7.	SEM micrographs of as cast equiatomic AlFeCoNiCu. 31
Figure 8.	XRD patterns of as cast equiatomic AlFeCoNiCu at (a) room temperature, and (b) 1,170K. 33
Figure 9.	EBSD images. 34
Figure 10.	EDS elemental map of equiatomic AlFeCoNiCu.. 35
PAPER II	
Figure 1.	The investigated HEAs in the present work. 44

Figure 2.	(a) Fcc supercell structure used for calculating the GSFE curves and surface energies (visualized by VESTA [43]). (b) Calculated GSFE curves for CoCrFeNi and CoCrFeNiAl _{0.3} Ti _{0.1} by considering two different fault planes shown in panel (a); subset pictures show twin boundary formation for the two cases.....	46
-----------	---	----

PAPER III

Figure 1.	Binary phase diagrams of Co-Cr system.	63
Figure 2.	Ternary phase diagrams of Cr-Fe-Ni system.	64
Figure 3.	Phase diagrams of Fe _{0.2} Mn _{0.2} Ni _{0.2} Cr _x Co _(0.4-x) HEA systems.....	66
Figure 4.	Phase diagrams of AlCo _v CrFeMo _{0.5} Ni HEA.	67
Figure 5.	(a) Experimentally determined phase diagram from Ref. [28] and (b) Calculated phase diagram of Al _u CoCrFeMo _{0.5} Ni HEAs, (c) Experimentally determined phase diagram from Ref. [28] and (b) Calculated phase diagram of AlCoCr _w FeMo _{0.5} Ni HEAs, (e) Experimentally determined phase diagram from Ref. [28] and (f) Calculated phase diagram of AlCoCrFeMo _y Ni HEAs.....	68

PAPER IV

Figure 1.	Strength-ductility profiles (at room temperature) for different metallic materials including HEAs.....	75
Figure 2.	Calculated carbide formations considering addition of different alloying elements to Cr-Al from ternary to six elements HEA.	77
Figure 3.	EDS elemental map of Al _{0.3} CoCrFeNiCu.....	79
Figure 4.	EDS elemental map of Al _{1.5} CoCrFeNiCu.....	80
Figure 5.	EDS elemental map of Al _{2.8} CoCrFeNiCu.....	81

LIST OF TABLES

PAPER I		Page
Table 1.	Measured properties of as cast equiatomic AlFeCoNiCu alloy.....	33
Table 2.	EDS composition analysis of AlFeCoNiCu (at. %).....	35
PAPER II		
Table 1.	Lattice constants (a) and calculated USFE (γ_{USF}), ISFE (γ_{ISF}) and UTE.....	50
Table 2.	Calculated relative barrier height (δ_{usf}^{rel}), theoretical twinnability (τ_a) , ₍₁₁₁₎ surface energy (γ_s), and Rice-criterion ductility (D).	51
PAPER IV		
Table 1.	Structures and solidification temperatures of aluminum and chromium carbides.....	76
Table 2.	Quantitative elemental EDS analysis.....	82

1. INTRODUCTION

Multi-principal element (MPE) alloys, also known as high entropy alloys (HEAs), are a new class of metallic alloys that emerged in the last two decades. The first articles on MPE alloys were published in 2004; however, these alloys were invented earlier in the 1990's [1]. Several definitions of HEAs have been used in the literature but the most common one defines these alloys as high disorder degree multicomponent alloys consisting of five or more alloying elements with near equi-atomic (equi-molar) compositions [1, 2]. For the last thirteen years, several research articles have been published in the literature investigating different aspects of microstructures and properties of HEAs. These research articles have tried to provide a better conceptual understanding of HEAs. For instance, Guo *et. al.* [3] proposed that the microstructures of most HEAs can be predicted by their valence electron concentrations (VEC). This model shows that the HEAs with $VEC \leq 6.7$ will stabilize a bcc structure while the HEAs with $VEC \geq 7.8$ form a fcc structure [3].

However, due to the unique characteristics of HEAs such as sluggish diffusion, intense lattice distortions, cocktail effect and high order of elemental interactions in these alloys, prediction of phase formations and properties of HEAs is a challenging tasks [1, 2]. The calculated phase diagrams published in the literature have revealed the shortcomings of capabilities of the commercial software packages in accurately predicting the phase formations of MPE alloys [4]. In addition to the limited information on phase formations in HEAs, to the best of our knowledge, only a very few studies have been done to investigate the deformation mechanisms of HEAs [1]. Thus, more studies are required for determining the effects of alloying elements and stable/metastable phases on

deformation mechanisms of [1]. Therefore, the design of the HEAs to achieve desired phases and properties has basically involved costly experimental trial and error.

In this Ph.D. research project, computational models based on thermodynamic and first principle calculations are integrated into experimental castings and characterizations to provide a better understanding of phase formations, phase diagrams, phase formations and mechanical properties of some HEAs. A general literature review on MPE alloys including experimental and computational works is included in Section 1.1. Then, the results of this Ph.D. research project are presented in five journal manuscripts, four included in the body of this dissertation (Paper I to IV) and one in Appendix A. In the first journal paper, microstructure and phase transformation in cast AlFeCoNiCu HEA were investigated using a combination of experiment, thermodynamic methods and first principle approach including density functional theory (DFT) and *ab initio* molecular dynamics (AIMD). The second journal paper, studied the plastic deformation mechanisms and ductilities of thirteen CoCrFeNi-based fcc HEAs focusing on the elemental impacts. Following this procedure, a project was completed to investigate the elemental effects on martensitic phase transformations in AHSS (Appendix A). In the third paper, a CALPHAD thermodynamic approach was integrated with a first principle method to calculate the phase diagrams of different metallic alloys from binary phase diagrams to HEAs along with the commercial thermodynamic databases. Finally, in the last paper a project is undertaken to investigate the effects of interstitial carbon on $\text{Al}_x\text{CoCrFeNiCu}$ ($x=0.3, 1.5, 2.8$) microstructures. The following section presents a general literature review on HEAs. More detailed literature reviews about the studied topics in this Ph.D. research project are provided as part of five journal

manuscripts. Four included in the body of this dissertation (Paper I to IV) and one in Appendix A.

1.1. CURRENT STATE OF THE ART OF MPE ALLOYS

Specific standard principles including high mixing entropy ($\Delta S_{mix} \geq 1.6R$, where R is the gas constant), small enthalpy of mixing ($-40 \leq \Delta H_{mix} \leq 15$ kJ mol⁻¹), and small atomic radii difference between the alloying elements (less than 12%), differentiate HEAs from other multicomponent alloys [2, 5, 6]. These standard principles aid in stabilizing random solid solutions (RSS) with least tendency for intermetallic phase formations or elemental segregations [1]. Based on these principles, several HEAs have been developed. Unique microstructures and outstanding properties of some of these HEAs have resulted in recent increase in development of these alloys. HEAs have wide range of applications in the aerospace and other industries because of their exclusive properties such as high corrosion resistance (e.g., Al_{0.5}CoCrCuFeNiB_x [7]), impressive strength and hardness (e.g., Al_xCrFe_{1.5}MnNi_{0.5} [8]), high ductility (e.g. Al_{0.3}CoCrFeNi [9]), excellent wear resistance (e.g., Al_xCo_{1.5}CrFeNi_{1.5}Ti_y [10]), oxidation resistance (TiVCrAlSi [11]), and some other properties for different applications [12, 13], but more importantly, some of HEAs show promising mechanical properties at higher temperatures [14] (e.g., Al_{0.5}CrFe_{1.5}MnNi_{0.5} [15]). Most of the developed HEAs in the literature tend to form simple microstructures with generally cubic crystal structures [16].

Figure 1.1. shows the number of occurrences of different phases in 648 studied HEAs reported by Miracle and Senkov [1]. In this figure, σ phase is D8b crystal structure (Pearson symbol tP30), C14 is hexagonal (Pearson symbol hP12), L1₂ is cubic (Pearson symbol cP4), C15 is cubic Laves phase (Pearson symbol cF24), E9₃ is cubic (Pearson

symbol cF96), $D0_2$ is cubic (Pearson symbol cF16) and $L2_1$ is cubic (Pearson symbol cF16) [1].

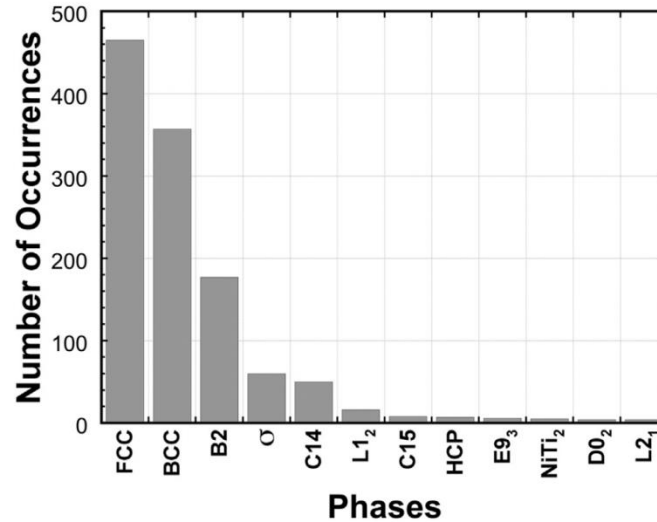


Figure 1.1. The number of occurrences of different phases of 648 HEAs reported in Ref. [1].

HEAs can be designed to have outstanding mechanical, thermal and chemical properties due to certain characteristics of these alloys such as sluggish diffusion, lattice distortion, and cocktail effect [17]. The possible sluggish diffusion in the HEAs is due to different neighboring atoms in each lattice site during the atom/vacancy jumps. This leads to different bonding and therefore different local energies. The sluggish diffusion in HEAs can have advantageous such as finer precipitates, higher recrystallization temperature, slower grain growth, lower particle coarsening rate, slower phase transformation, and higher creep resistance compared to the conventional multicomponent alloys [18]. The severe lattice distortion in HEAs can restrain the dislocation movements and increase the solid solution strengthening. Moreover, it can

made based on 3d transition metals (TM) such as Co, Fe, and Ni [22, 23] (e.g., $\text{Al}_x\text{CoCrCuFeNi}$ [24]). In some cases non-metallic elements such as silicon were added to alloying systems to enhance some properties such as corrosion resistance (e.g., $\text{Ni}_x\text{Co}_{0.6}\text{Fe}_{0.2}\text{Cr}_y\text{Si}_z\text{AlTi}_{0.2}$ [25]). These kinds of HEAs are anticipated to have promising properties at intermediate temperatures (less than 1200°C), but to have HEAs with reliable properties at higher temperatures, researchers have recently suggested refractory alloying elements such as Nb, Ti and Mo to cast refractory HEAs (e.g., WNbMoTaV [26]). Refractory HEAs usually produce stable BCC phases [27, 28], and their alloying elements have lower valence electron concentration (VEC) [3]. In 2013, a low density alloy with excellent high-temperature properties was obtained by Senkov *et al.* using light alloying elements with high melting temperatures (CrNbTiVZr) [29]. The equiatomic compositions in HEAs can result in stability of solid solutions due to the highest entropy of mixing compared to non-equiatomic compositions [18]. Therefore, any changes in fractions of the alloying elements can impact the microstructures and properties. For instance, increasing the amounts of aluminum in $\text{Al}_x\text{CoCrFeNiCu}$ ($x=0.3$ to 3) changes the microstructures from single phase fcc to a mixture of fcc and bcc and then to single phase bcc [30]. adding vanadium to NbMoTaW refractory HEA increases the yield strength of this alloy at high temperatures; both NbMoTaW and VNbMoTaW HEAs show higher yield strength than Inconel-718 and Haynes-230 alloys at temperatures between 700°C and 1600°C [31]. Addition of aluminum, especially in refractory HEAs, has beneficial effects on properties, such as reducing the density and increasing the Vickers hardness and strength of the alloy, because the volume fraction of the bcc phase increases as aluminum concentration increases [32]. In some cases highest

hardness was achieved at equiatomic combination of aluminum and other elements [33]. Cobalt and titanium help to stabilize the fcc structure in HEAs; Cobalt addition slightly decreases yield stress, but hardness increases as titanium concentration increases [34, 35]. Chromium and zirconium enhance the yield strength, ductility, fracture strength and corrosion resistance of refractory HEA [36]. Moreover, niobium addition was reported to improve wear and corrosion resistance of CoCrCuFeNi [37]. It has been shown that copper has positive enthalpy of mixing with other alloying elements in MPE alloys that results in segregating a Cu-rich phases in the inter-dendrite phases [38]. To resolve this problem, it is suggested to replace Cu with Mo [39, 40]. Recently, the addition of interstitial elements such as carbon and boron has shown to improve the strengths of $\text{Fe}_{44.4}\text{Ni}_{11.3}\text{Mn}_{34.8}\text{Al}_{7.5}\text{Cr}_6$ [41] and $\text{Fe}_{49.63}\text{Co}_{11.65}\text{Mn}_{27.27}\text{Cr}_{10.86}\text{C}_{0.59}$ [21]. Overall, the selection of alloying elements and their compositions in HEAs have heavily involved a trials and errors strategy, which have made the production of new HEAs a very slow and rather expensive process.

1.1.2. Manufacturing Methods. In addition to alloying elements and their compositions, the manufacturing process and the process parameters can also influence the properties of HEAs. Casting has been recognized as the primary material processing method in producing HEAs. However, other methods such as laser cladding and laser/electro deposition methods have been successfully applied for preparing some HEAs [42-45]. Induction melting and arc melting are widely used for casting of HEAs [46]. Very rapid solidification is recommended to prevent forming undesired phases in HEAs. Furthermore, some crystallization methods such as Bridgman or Czochralski can be used to control crystal growth [47, 48]. It is desired to have the least number of phases

in HEAs [49, 50], this can be achieved by controlling alloying elements and compositions as well as process parameters.

1.2. MODELING OF MPE ALLOYS

Phase diagram calculations, molecular dynamics and first principle simulations are included in this section.

1.2.1. Phase Diagram Calculations. Calculating the phase diagrams and predicting the crystal structures of HEAs are challenging tasks, because HEAs, unlike traditional alloys, do not have one dominating principal element that can control the microstructure; therefore, the effects of all the elements must be considered. Current available databases do not include the interactions between all the elements in HEAs; for example, phase diagrams of some HEAs (e.g., CoCrFeMnNi) recently calculated based on the current database by Pandat software [4] do not show good agreement with experimental results. CALPHAD and Muggianu methods [51], which are based on Gibb's free energy calculation, are suggested in the literature to calculate the phase diagram of multi-principal element alloys. However, due to the limitations of the individual methods in considering high order interactions [52], it is necessary to combine different methods and develop a general approach to calculate phase diagrams of HEAs.

In Gibb's free energy calculations, the significant role of entropy in stabilizing solid solutions has been addressed in the literature [53], where more negative entropy in association with total enthalpy lead to more stable phase formations [54]. Vibrations of electrons with temperature cause electronic entropy, while lattice vibrations of atoms cause vibrational entropy. Since contributions of electronic and vibrational entropies are very small, only configurational mixing entropy can be assumed in calculating the phase

diagrams of HEAs [55]. For HEAs containing iron, nickel or cobalt, magnetic entropy should be added as well. The principle of maximum entropy combining Shannon's entropy and Boltzmann-Gibbs entropy is suggested to calculate the distribution of atoms in the crystal structures of some HEAs, e.g., AlCoCrFeNi [55]. However, the maximum entropy method can be only applied for the ideal state of multi-principle systems in an equilibrium condition; moreover, this method is not feasible to calculate all crystal structures. The accuracy of this method decreases as the number of alloying elements increases. Therefore, other computational methods such as atomistic simulations or electronic scale calculations may be more suitable for determining crystal structures of HEAs.

1.2.2. Atomistic Simulation (Molecular Dynamics). Only a few molecular dynamic (MD) simulations have been reported in the literature to study atomic structures and properties of some HEAs. Recently, crystal growth and some properties such as thermal stability of AlCoCrCuFeNi [56] and radiation behavior of Al_xCoCrFeNi [57] were calculated using MD simulations. In another study, rapid solidification was considered to prevent the formation of unanticipated structures in predicting phase formations during cooling [58]. Separately, a hybrid MD/Monte Carlo simulation was developed to study refractory HEAs; where temperature-dependent chemical order was calculated, then with considering the structural energy minimization for a particular crystal structure (e.g., bcc), a distribution of refractory alloying elements was determined [59]. All these studies used only pair potentials, including Embedded, Tersoff and Lennard-Jones.

Despite the recent advancements made in MD simulations of HEAs, the current MD models for HEAs cannot provide reliable results, because by using pair potentials, only binary interactions can be considered, however, HEAs having multi-principle elements in each unit cell need consideration of higher order interactions. Due to the unavailability of interatomic potentials suitable for HEA systems, density functional theory (DFT) calculations based on first principles could be a more appropriate method to study crystal structures and properties of HEAs.

1.2.3. Electronic Scale Simulation (First Principle). DFT approach is the most common first principles methods to study the electronic structures and atomic interactions at their fundamental level. This approach is capable of calculating large and complex systems with reasonable computational expenses [60]. Since there is not an exact (absolute) solution of the exchange-correlation interactions for the universal ground state functional, some approximations such as local-density approximations (LDA) and generalized-gradient approximations (GGA) are introduced to solve the functional accurately [61, 62]. DFT calculations can predict atomic distribution in solid solutions by calculating the lattice parameter of perfect cells and computing cohesive energies (or bonding energies). DFT pseudo-potential calculations can predict atomic arrangement in the cells as well as the stability of the crystal structures. The energies of vacancy formation as a function of crystal binding energies can explain the lattice stability of HEAs (e.g., CoCrFeNi [63]). Moreover, first principle calculations based on DFT using CASTEP software, are reported to compute the lattice constant, cohesive energy, elastic constants and enthalpy of formation of intermetallic compounds in FeTiCoNiVCrMnCuAl HEA at zero Kelvin [64]. Results of DFT calculations are

accurate at zero Kelvin, and *ab initio* molecular dynamics (AIMD) (DFT at high temperatures) is needed for calculations at higher temperatures [49]. In a recent work, primary phase formation during solidification was explained by investigating partial pair correlations of elements, self-diffusion constants and calculation of bond length of binaries in some HEAs, such as HfNbTaTiZr [49]. Atomic distributions in crystal structures and high order interactions of elements cannot be predicted by considering pair correlations. In another work, Tian et al. intended to calculate the mechanical properties such as Young's and shear modulus of refractory HEAs with single bcc structure such as TiZrNbMoV_x by using an *ab initio* exact muffin-tin orbital (EMTO) method [65]; however, EMTO can only provide properties at zero K. Finally, intrinsic stacking fault energies of some HEAs has been calculated utilizing first principles approaches [38, 66].

The main weaknesses of the current DFT and AIMD calculations for HEAs are: 1) all the principal elements are assumed to exist in different phases, and 2) random positions of atoms in crystal structures are considered not the stable positions. Based on our experiments and AIMD calculations both of these assumptions have flaws and can influence the predicted results.

The details of the first principles methods including DFT and AIMD that used in this Ph.D. research project are included in Appendix B.

2. RESEARCH OBJECTIVES AND IMPACT

The goal of this research project is to provide a better understanding of phase formations in high entropy alloys (HEAs). First principle atomistic/electronic approach is applied to study the crystal structures and mechanical properties of some HEAs, and thermodynamic methods and experimental investigations are used to determine phases of HEAs. The objectives are outlined below:

- Objective 1: Predicting phase diagrams of HEAs
 - ❖ Calculate the phase diagrams of HEAs utilizing sublattice CALPHAD thermodynamic approach integrated with Muggianu's extrapolation method utilizing experimental databases
 - ❖ Integrate the CALPHAD thermodynamic approach with first principle atomistic approach to calculate the phase diagrams of HEAs overcoming the complexity of the sublattice method in determining complex crystal structures
 - ❖ The stability of different phases using the first principle approach including density functional theory and *ab initio* molecular dynamics
 - ❖ Evaluate the modeling results by experimental casting and characterizations
- Objective 2: Studying the effects of addition of alloying elements on deformation mechanisms of CoCrFeNi-based FCC HEAs
 - ❖ Calculate generalized stacking fault energies to investigate the plastic deformation mechanisms including martensitic transformation, mechanical twinning or dislocation mediated slip
 - ❖ Determine the ductilities of the selected HEAs

- ❖ Follow the same procedure to study the effects of alloying elements on stacking fault energies and phase transformation of Fe-Mn-Si-Al-C high strength steel
- Objective 3: Evaluate the effects of interstitial carbon on the microstructures of $\text{Al}_x\text{CoCrFeNiCu}$ HEAs

The results of this research project may guide designing of HEAs with desired phases, which can consequently help in predicting properties. The first principle methods, thermodynamic approaches and experimental characterizations in this work were integrated trying to provide fundamental understanding of elemental effects on the microstructures and properties of some HEAs, and these techniques can be extended to study of other MPE alloy systems.

PAPER**I. INVESTIGATING PHASE FORMATIONS IN CAST AlFeCoNiCu HIGH ENTROPY ALLOYS BY COMBINATION OF COMPUTATIONAL MODELING AND EXPERIMENTS**

M. Beyramali Kivy, M. Asle Zaeem*, and S. Lekakh

Department of Materials Science and Engineering, Missouri University of Science and Technology, 1400 N. Bishop Ave, Rolla, MO 65409, USA

(Materials & Design 127 (2017) 224-232)

ABSTRACT

Selection and thermal stability of phases are important in design of high entropy alloys (HEA). In this study, phase formations in cast AlFeCoNiCu HEA were investigated. *Ab initio* molecular dynamics (AIMD) simulations were used to determine crystal structures of phases at different temperatures in equiatomic composition of AlFeCoNiCu. The AIMD results showed a possible coexistence of a face-centered cubic (fcc) phase and a body-centered cubic (bcc) phase at the room temperature and indicated stabilization of a single fcc phase above 1,070 K at the equiatomic composition of AlFeCoNiCu. The phase diagrams of AlFeCoNiCu system were calculated using a modified thermodynamic approach based on CALPHAD and Muggianu's methods. The calculated phase diagrams showed formation of the same two phases at the room temperature, and a phase transformation at about 1,010 K to form a single fcc phase. The characterization experiments utilizing scanning electron microscopy (SEM), X-ray diffraction (XRD), and electron backscatter diffraction (EBSD) confirmed the crystal structures and composition of phases determined by AIMD simulations and phase

diagram calculations. High temperature XRD (HTXRD) analysis showed a significant increase in weight fraction of the fcc phase at high temperatures confirming the predicted phase transformation.

Keywords: High Entropy Alloys; AlFeCoNiCu; ab-initio Molecular Dynamics; Phase Diagram; Electron Backscatter Diffraction; X-ray diffraction.

1. INTRODUCTION

High Entropy Alloys (HEAs), which are also known as high disorder degree alloys [1], are formed by combining five or more elements of approximately equiatomic ratios (5 to 20% each) [2]. HEAs were first created in the 1990s [3], and the first research articles about HEAs were published in 2004 [4, 5]. HEAs are defined based on some standard principles which distinguish them from other multi-component alloys such as metallic glasses [6]. These principles are: a) HEAs have high entropy of mixing ($\Delta S_{mix} \geq 1.6R$, where R is the gas constant), which requires having at least five components in the alloy system; b) there is only a small difference between atomic sizes of alloying elements (less than 12%), because large difference in atomic radii causes large lattice distortion as well as low atomic diffusion rate in the liquid state [7]; and c) alloying elements have a small enthalpy of mixing ($-40 \leq \Delta H_{mix} \leq 15$ kJ mol⁻¹), because a large positive enthalpy of mixing will result in elemental segregation, and a large negative enthalpy of mixing will result in the formation of intermetallic compounds [8, 9]. Several HEAs have been developed and studied based on these principles.

Most of the developed HEAs have simple microstructures and tend to form simple random solid solution (RSS) phases [10], mainly cubic crystal structures, rather than

complex intermetallics [11, 12]. In the case of simple crystal structures (such as cubic structures), choosing elements with large atoms stabilize the crystals with lower packing density such as body-centered cubic (bcc), while smaller atoms tend to relax into higher packing density structures such as face-centered cubic (fcc) [13]. Similar to other metallic alloys, microstructures of HEAs determine the properties of HEAs; for example in some HEAs, the right mixture of cubic crystals (bcc+fcc) is expected to produce balanced mechanical properties, e.g., having high strength and good ductility [14-17]. Recently, eutectic HEAs were suggested as a way to design the alloys with proper composite structure. These type HEAs are also claimed to have improved high temperature properties [18].

Equiatomic compositions of HEAs have the highest entropy of mixing which results in stability of solution phases [19]. On the other hand, experiments confirm that slight changes in concentration of elements can significantly affect microstructures and properties of HEAs. In most of the non-refractory HEAs (3d HEAs), iron is the solvent and forms the matrix phase (primary phase) due to its high melting temperature and relatively large atomic radius [20]. As shown schematically in Figure 1, different constituent elements cause lattice distortion which increases the solution hardening and decreases the degree of crystallinity and x-ray scattering [21]. Cobalt and titanium help stabilize fcc structure in HEAs; cobalt addition slightly decreases true stress, and hardness increases as titanium concentration increases [22, 23]. Addition of nickel increases the operation temperature and decreases the brittleness, thus it helps reducing cracking during solidification [24]. In addition to the above effects, the ferromagnetic moments of iron, cobalt and nickel will result in high magnetic properties of alloying

systems [10, 25, 26]; other alloying elements can be added to this mixture to enhance some other properties. For example, addition of copper can stabilize fcc phase and enhance the ductility of the alloys [27]. Addition of aluminum has also beneficial effects on properties such as reducing the density and increasing the hardness and strength of the alloys, by increasing the lattice strain, elastic energy and bcc phase ratio [28]. Furthermore, segregation of elements may happen by addition of aluminum due to different composition of dendritic and interdendritic regions [29]. In this work, we study the atomistic and micro structures of AlFeCoNiCu HEAs. Taking into account the possible effects of alloying elements, determining the crystal structures and phase diagrams of HEAs are required to be able to predict the stable phases and the subsequent microstructures and properties of cast HEAs.

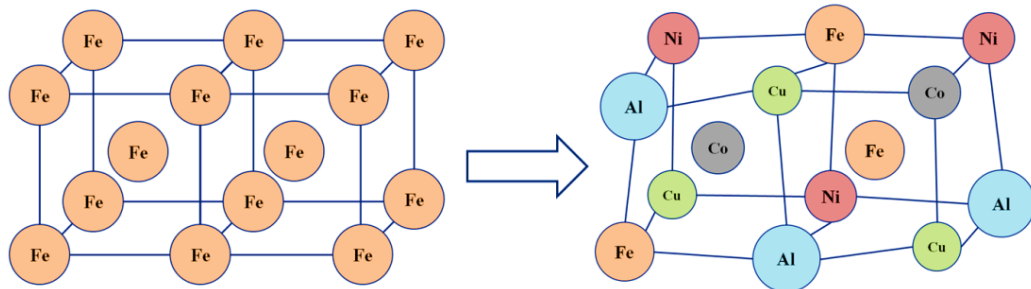


Figure 1. Schematic illustration of AlFeCoNiCu bcc lattice distortion.

The crystallographic investigation of HEAs is a challenging task. For instance, during atomic diffusion and phase transformation in HEA systems, different type of neighboring atoms may form because of jumping of vacancies. Although this phenomenon leads to smaller grains of HEAs [12], slow diffusion and phase

transformations in these alloys may lead to formation of undesirable phases. Because of insufficient available experimental data, computational modeling at small scales may be useful to study the crystal structures of HEAs [30]. There are some work in the literature those utilized molecular dynamic (MD) simulations to study atomic structures and properties of some HEAs [31-33]. Also, a hybrid MD/Monte Carlo simulation has been developed to study refractory HEAs, where temperature-dependent chemical order was calculated, then with considering the structural energy minimization for a particular crystal structure (e.g., bcc), distribution of refractory alloying elements was determined [34]. Despite the recent advancements made in MD simulations of HEAs, the current MD models cannot provide reliable results for HEAs, because they mostly use pair potentials, such as Embedded, Tersoff and Lennard-Jones potentials, therefore they can only consider binary interactions [35]. HEAs have multi-principle elements in each unit cell and accurate MD simulations need to consider higher order interactions which are computationally complex and expensive to develop the required potentials. To overcome this limitation of MD simulations, electronic scale simulations using first principle methods can be used to gain insights on the effects of higher order interactions in HEAs.

First principle studies including density functional theory (DFT) and ab-initio molecular dynamics (AIMD) calculations can predict atomic distribution in solid solutions and determine the stability of the crystal structures. In this work, we utilize AIMD calculations to determine the lattice constants and stable crystal structures of equiatomic AlFeCoNiCu at different temperatures. Since classical DFT calculations are only applicable at ground state for many-body systems, AIMD (DFT at high temperatures) was used for calculations at elevated temperatures [36].

There are few works that used only experiments for calculating phase diagrams of HEAs. For example, empirical calculations of phase diagrams of AlCoCrFeMoNi system were performed by Chin-You Hsu in 2013 [37], in which they combined SEM, transmission electron microscopy (TEM), XRD, HTXRD and differential thermal analysis (DTA) data to calculate the phase diagram. Experimental determination of phase diagrams is very valuable, but it is very time-consuming and expensive.

Another way to determine the stable phases of HEAs at different temperatures is to utilize semi-empirical thermodynamic approaches to calculate phase diagrams of HEAs, however there are some challenges to accomplish this. Current available databases do not include the complete interactions between all the elements in HEAs [38, 39]. For example, the principle of maximum entropy combining Shannon's entropy and Boltzman-Gibbs entropy was suggested in the literature to calculate the distribution of atoms in the crystal structures of some HEAs, e.g., AlCoCrFeNi [40]. However, the maximum entropy method can be applied only for the ideal state of multi-principle systems in an equilibrium condition; moreover, this method is not feasible to calculate all kinds of crystal structures. The accuracy of this method decreases as the number of alloying elements increases. To address this, we employ a multi-component system thermodynamic approach based on CALPHAD method to calculate the phase diagrams of AlFeCoNiCu more accurately. This method considers regular solutions instead of ideal state to calculate the free energy of formation of different crystal structures [41]; also quaternary interaction functions are used utilizing the Muggianu's extrapolation method [42].

In this work, AIMD simulations, phase diagram calculations, and experimental characterizations are utilized to study phase formations and microstructures of cast AlFeCoNiCu HEAs. The rest of this article is organized in three sections. First section explains the details of modeling processes and experimental techniques that were utilized in this work. Second section presents the results and discussions; first DFT and AIMD simulation results for predicting the crystal structures and phases are presented and discussed, then the calculated phase diagram of AlFeCoNiCu by the thermodynamic modeling approach is described, and lastly the experimental results for microstructures and properties of equiatomic AlFeCoNiCu alloy are presented to verify the modeling predictions. Finally, in the last section, the results are summarized and a short conclusion is included.

2. METHODS AND PROCEDURES

2.1. AB INITIO MOLECULAR DYNAMICS

In order to better understand the crystal structures and atomic compositions of AlFeCoNiCu, we performed ab-initio DFT and AIMD simulations. For this purpose, at first, formation energy of bcc and fcc crystals with different atomic compositions and different lattice constants were calculated using Vienna *ab initio* Simulation Package (VASP) [43] and considering generalized gradient approximation (GGA). In this task, both fcc and bcc supercells were made of 96 atoms along three primary axes ($\langle 100 \rangle$ family of axes) considering the symmetries along $\langle 100 \rangle$, $\langle 111 \rangle$ and $\langle 110 \rangle$ directions. Periodic boundary conditions in all three perpendicular directions and Monkhorst pack automatic mesh were assumed [43]. All the structures were relaxed until the ionic optimization convergence was within $0.01 \text{ eV atom}^{-1}$. Because of the variety of the

elemental characteristics and lattice distortions, random distributions of the atoms cannot result in the minimum formation energies, therefore the considered crystals were relaxed, and the equilibrium lattice constants and the most stable atomic compositions were calculated.

2.2. PHASE DIAGRAM CALCULATION

The significant role of entropy in stabilizing solid solutions has been addressed in the literature [44], where more negative entropy (high entropy) in association with total enthalpy leads to formation of more stable phases [10, 45]. Since contributions of electronic and vibrational entropies are very small, one can only use the configurational mixing entropy (Eq. 1) in calculating the regular Gibbs free energies of different phases of HEAs [40]:

$$S_{config} = k_B \left[\frac{3}{2}(\xi - 1)y_1 + \frac{3}{2}(\xi - 1)^2 y_2 - \left[\frac{1}{2}(\xi - 1)(\xi - 3) + \ln \xi \right] (1 - y_3) \right], \quad (1)$$

where k_B is Boltzman constant, ξ is packing fraction parameter and y_1 , y_2 and y_3 are dimensionless parameters described in the literature [46]. However, for multi-component systems with n-elements such as HEAs, it is possible to use the mixing entropy definition

$$(S_{config} = -R \sum_{i=1}^n x_i \ln x_i) \text{ to describe the configurational entropy [40].}$$

CALPHAD and Muggianu methods [42], which are based on Gibbs free energy calculations, are suggested in the literature to calculate the phase diagram of multi-principal element alloys [42]. However, due to the limitations of the individual methods in considering high order interactions [47], it is necessary to combine different methods and develop a more accurate approach to calculate phase diagrams of HEAs. We applied

the sublattice model of the CALPHAD method [41, 44] to investigate the phase equilibria of AlFeCoNiCu HEAs with different compositional molar fractions. The Gibbs free energies of possible combinations of alloying elements (e.g., pure, binary, ternary, etc.) in each system were determined considering different crystal structures (fcc, bcc and hcp) and temperatures by employing the Factsage software database [48]. Then, these Gibbs free energies are inserted in the CALPHAD sublattice model. Since CALPHAD includes only binary and ternary interactions, Muggianu method [42] is used to extrapolate CALPHAD results for considering quaternary interactions between alloying elements in AlFeCoNiCu HEAs. The following equations show the procedure of Gibbs free energy calculations for different phases.

$$G^{Phase} = G^{reference} + G^{ideal} + G^{excess}, \quad (2)$$

$$G^{Phase-Ternary} = \sum x_i G_i^0 + RT \sum x_i \ln(x_i) + \sum \sum x_i x_j \sum_{m=0}^n G_m^{ij} (x_i - x_j)^m, \quad (3)$$

where x_i is the molar fraction of component i , R is the gas constant, T is the temperature, $\sum_{m=0}^n G_m^{ij} (x_i - x_j)^m$ is Redlich-Kister polynomial which n is the number of elements [49]. In this equation, G_i^0 is the standard-state free energy of component i that can be written as polynomial functions of temperature. The configurational mixing entropy explained in Eq. 1 was used in calculation of the excess free energy ($G_m^{ij} = H_m^{ij} - TS_m^{ij}$, where H_m^{ij} is the enthalpy of binary systems and $S_m^{ij} = S_{config}$). For higher order phases with five elements, more terms should be added in Eq. 3 according to the Muggianu extrapolation:

$$G^{Phase} = \sum x_i G_i^0 + RT \sum x_i \ln(x_i) + \sum \sum x_i x_j \sum_{m=0}^n G_m^{ij} (x_i - x_j)^m + \sum \sum \sum x_i x_j x_k G^{Phase - Ternary} \quad (4)$$

$$+ \sum \sum \sum \sum x_i x_j x_k x_l G^{Phase - Quaternary} .$$

For alloying systems with more than five elements, higher order phases (more than quaternary phases) should be considered. Eq. 4 describes the Gibbs free energy of formation of different phases used in this work as a function of molar fractions of alloying elements and temperature.

2.3. CASTING AND CHARACTERIZATION

Casting has been recognized as the primary material processing method in producing HEAs, while some other methods such as laser cladding and electro-deposition methods can be potentially applied for preparing HEAs [50]. In our casting experiments, small ingots of AlFeCoNiCu alloy were prepared using Miller vacuum arc-melting furnace with equiatomic composition of the corresponding elements. Small granules (< 2 mm) of ~99.9% pure alloying elements were stirred with ethanol for dehydration purposes before arc melting process. Remelting of ingots was performed multiple times (3-5 times) and molten material stayed in the liquid state for almost 4 minutes during each melting step to enhance the homogeneity. Arc melting of the alloy was conducted on a water circulation cooled copper plate. 70 kW Inductotherm induction furnace was used to make larger specimens (~200 g) for further experiments. Pure silica (quartz) crucibles and a graphite coated steel mixer were used in preparation of the alloys. All specimens were fast cooled (~110 K.min⁻¹) to prevent the formation of intermetallics. The samples were polished and etched with an etching solution containing 90 vol.% ethanol and 10 vol.% aqua-regia.

As cast microstructures were analyzed using Scanning Electron Microscopy (SEM) (FEI Helios NanoLab 600 FIB/FESEM). Elemental compositions of the phases as well as atomic distributions were studied using Oxford Energy Dispersive Spectrometer (EDS). Crystal structures and orientations were determined by Electron Backscatter Diffraction (EBSD) system. X-Ray Diffraction (XRD) analyses were performed by using a Philips X-Pert Diffractometer. The tensile properties were measured using MTS809 testing machine with 0.02 mm.s^{-1} strain rate. Three cylindrical specimens with 6 mm diameter and 40 mm gauge length were tested at room temperature. Vickers hardness was measured with 100 g load.

3. RESULTS AND DISCUSSIONS

3.1. CRYSTAL STRUCTURES AND PHASES DETERMINED BY AB INITIO MOLECULAR DYNAMICS SIMULATIONS

To determine the composition and lattice constants of fcc and bcc crystal structures in the AlFeCoNiCu alloying system, the formation energy versus lattice parameter was calculated considering different combinations of alloying elements. Results in Figure 2 were determined using DFT calculations. After completing several simulations considering different combinations of alloying elements and crystal structures, the most stable composition for the fcc phase was determined to be FeCoCu, while the most stable composition of bcc crystals was AlFeCoNi (these results are in agreement with SEM-EDS results). The equilibrium lattice constants of fcc and bcc phases were calculated to be 3.6 \AA and 2.9 \AA , respectively (which are in good agreement with XRD results). The formation energy of both fcc and bcc crystals at their stable lattice constants were the same (-32.5 eV), which means both fcc and bcc phases can

coexist at low temperatures. DFT calculations indicated that not all the five elements in the AlFeCoNiCu system are present in the fcc and bcc phases based on the principle of minimum formation energy.

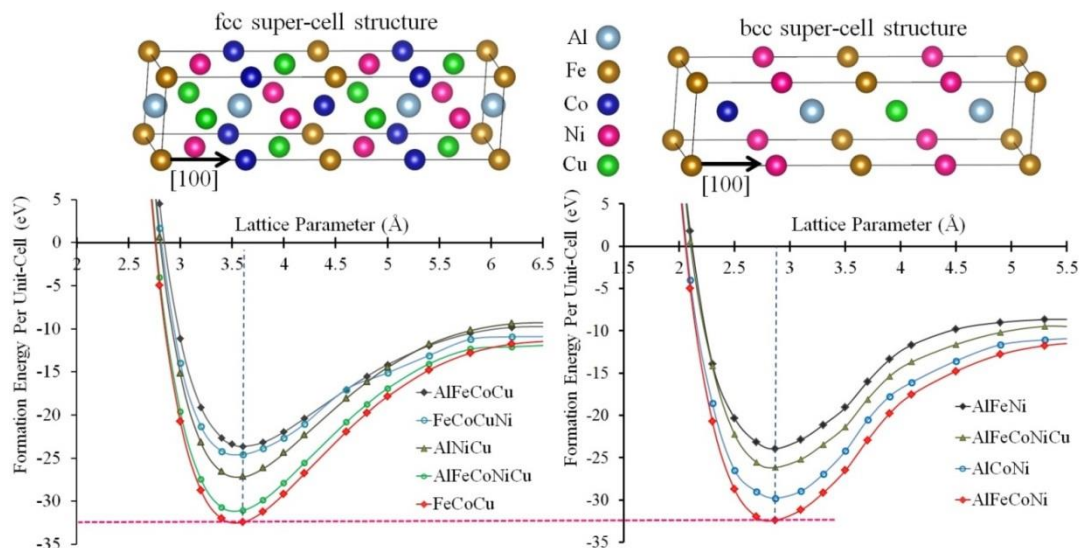


Figure 2. Calculated formation energies of (a) selected fcc supercell crystals and (b) selected bcc supercell crystals with different compositions at zero K. A slice of a supercell (total of 96 atoms visualized with VESTA [51]) for equiatomic AlFeCoNiCu is shown above each graph.

Since DFT calculations provide only the ground state (0 K) properties of a system, to calculate the crystal structures and associated composition at higher temperatures ($0\text{K} < T < 1100\text{K}$), and also determine possible solid-state phase transformations, AIMD simulations were conducted at elevated temperatures for both fcc and bcc crystal structures with different compositions. The results of the AIMD simulations at three different temperatures are presented in Figure 3 for equiatomic AlFeCoNi-bcc, FeCoCu-fcc and AlFeCoNiCu-fcc phases. Results show that the quaternary bcc phase (AlFeCoNi) and ternary fcc phase (FeCoCu) which are stable at

ground state, are not stable at higher temperatures. By increasing the temperature, a solid-state phase transformation from a dual phase (fcc+bcc) structure to a single equiatomic fcc phase is predicted to start at around 1,073 K.

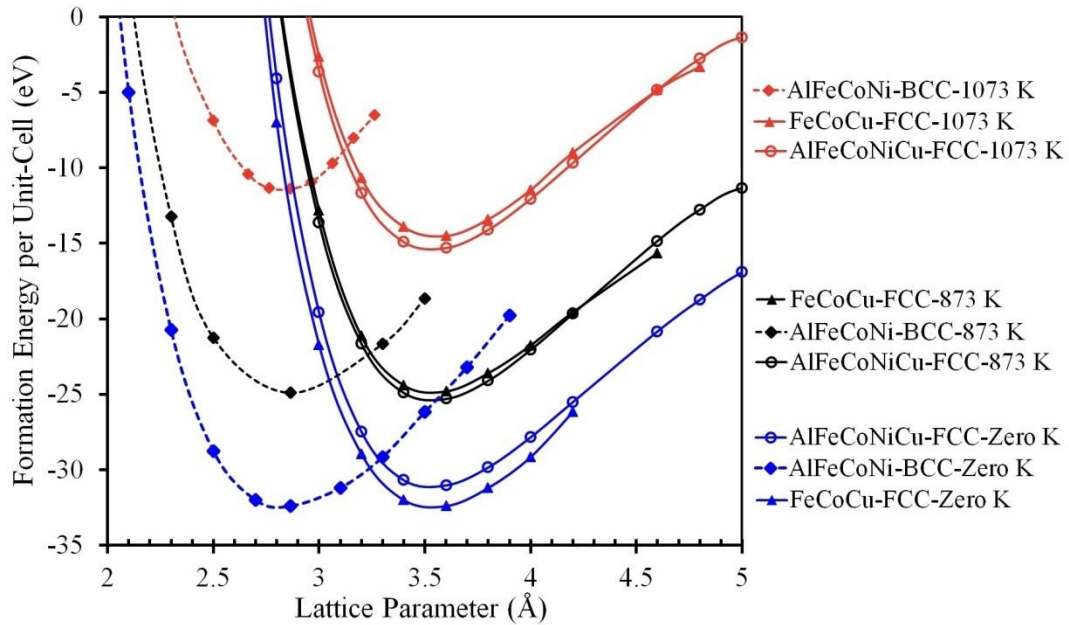


Figure 3. Calculated formation energy for equiatomic AlFeCoNi, FeCoCu and AlFeCoNiCu systems at 0 K, 873 K and 1,073 K.

3.2. PHASE DIAGRAMS OF AlFeCoNiCu

Eq. 4 was used to determine the effects of alloying elements and temperature change on the Gibbs free energy of formation of different phases in AlFeCoNiCu alloy system. Molar fraction of each element was changed from 0 to 1 using a molar fraction step of 0.05, and the most stable phases were determined as a function of molar fraction of alloying elements and temperature. As an example, Figure 4 was calculated for equiatomic composition of AlFeCoNiCu. Initially at lower temperatures ($T \leq 950$ K) bcc and fcc phases are formed, and then by increasing the temperature ($1,010$ K $\leq T \leq 1,320$ K)

K), only one single fcc phase is stabilized. These results are in good agreement with the AIMD calculations in Section 3.1.3.1. At about 1,320 K, the alloy eventually starts to melt and finally at around 1573 K it is almost completely liquid.

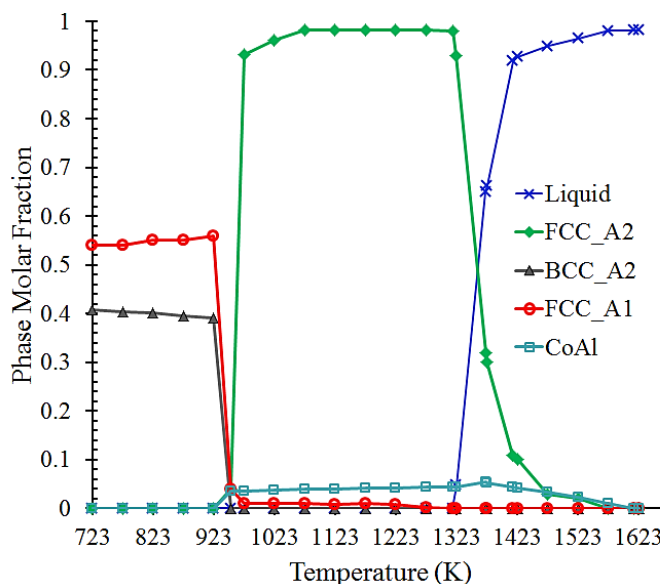


Figure 4. Molar fraction of the stable phases as a function of temperature for equiatomic composition of AlFeCoNiCu HEA.

As mentioned before there is a phase molar fraction diagram similar to Figure 4 for each composition of the alloying system. The final complete phase diagram of $\text{Al}_x\text{CoFeCuNi}$ was calculated by combining all of the phase fraction data for different elemental compositions at different temperatures considering the Gibbs-Helmholtz rule [52]. Due to the free energy minimizations, some minor phases can stabilize with very low fractions (e.g., CoAl in Figure 4) at some specific temperatures and compositions but are not stable at slightly different temperatures and compositions. These insignificant phases were neglected in the phase diagram calculations.

Figure 5 shows the calculated phase diagram for $\text{Al}_x\text{CoFeCuNi}$ HEA system with variation in Al molar fraction (x) at equal molar fractions of the other components, $y=0.25*(1-x)$, by combining all the thermodynamic data. This phase diagram shows that fcc and bcc phases coexist in wide ranges of temperature and aluminum molar fraction, x . The equiatomic composition line for all elements ($x=0.2$) shows that a transformation from a two-phase (fcc+bcc) microstructure at the room temperature to a single fcc phase occurs at higher temperatures ($>1,010$ K).

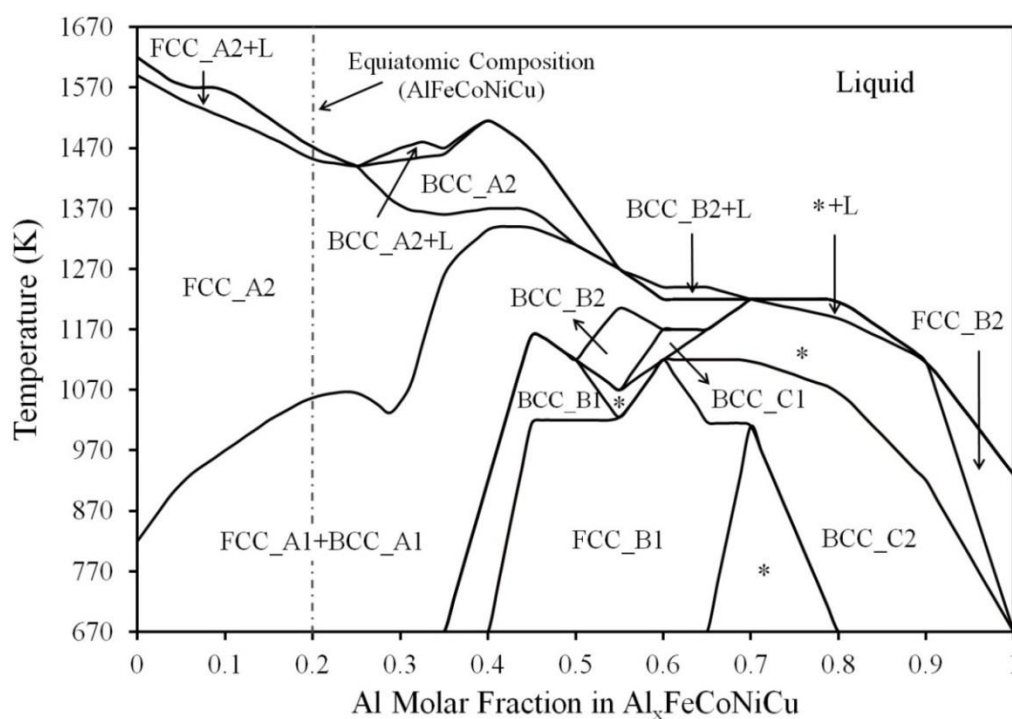


Figure 5. Calculated phase diagram of $\text{Al}_x\text{FeCoNiCu}$. FCC_A1 phase has Fe, Co, Cu elements, and BCC_A1 phase has Al, Fe, Co, and Ni elements. All the five elements are present in FCC_A2, FCC_B1, FCC_B2, BCC_A2, BCC_B1, BCC_B2, BCC_C1, and BCC_C2 phases. Fields designated by * have several intermetallic phases with different crystal structures.

Using the same procedure for the other alloying elements, the phase diagrams in Figure 6 were calculated. The dashed-lines on the phase diagrams in Figure 5 and Figure 6 show the equi-atomic composition with the same phase evolution in all calculated phase diagrams. It is seen in Figure 5 that as the Al molar fraction increases, the ratio of bcc phases increase in the phase diagram and the melting temperature of the alloy decreases. As shown in Figure 6, increasing the amounts of Cu, Ni and Co stabilized the fcc structure instead of duplex fcc-bcc structure.

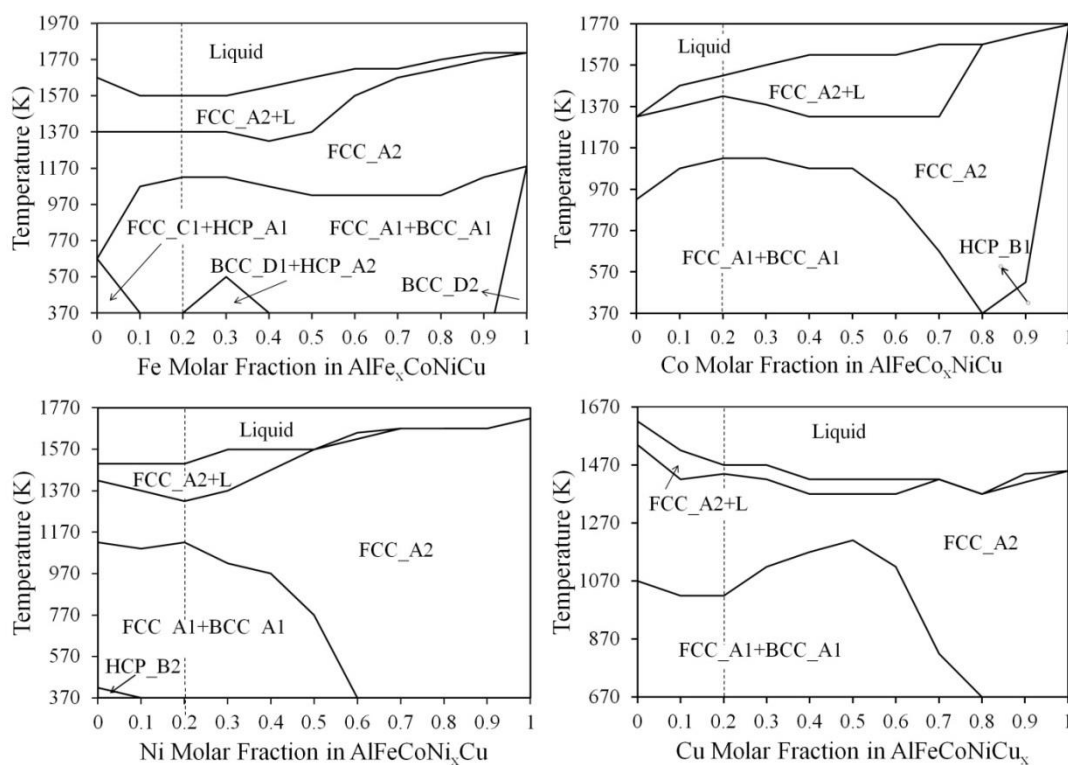


Figure 6. Calculated phase diagrams of AlFeCoNiCu with changing molar fractions of different elements. FCC_A1 phase has Fe, Co, Cu elements, and BCC_A1 phase has Al, Fe, Co, and Ni elements. All the five elements are present in FCC_A2, BCC_D2, HCP_B1 and HCP_B2 phases. FCC_C1 phase contains Al, Fe, Ni and Cu elements. HCP_A1 phase has Co and Cu elements and HCP_A2 has Co, Cu, and Ni. BCC_D1 contains Al, Fe and Ni.

The calculated phase diagrams of HEA, available in the literature, are mostly carried out by Pandat software [53]. However, those calculations have some limitations. For instance, Zhang et al. work [38] only considered binary and some of the ternary interactions, e.g., the interaction parameters higher than 3rd order (described in Eq. 3 and Eq. 4) were not considered [9]. Also, the molar fractions of only two components were varied while the molar fractions of the rest of the elements in alloying systems were kept constant [38]. Furthermore, the phase diagram was calculated for temperatures 1,270 K and above, but the equilibrium phase fraction calculation was reported for the temperatures below 1200 K also showed formation of different phases; therefore, some of the phases that form at low temperatures are not shown in the phase diagram [9].

The thermodynamic approach presented in this work considers the effects of all the alloying elements in the HEAs, however it should be noted that the accuracy of the calculations decreases as the number of components increases.

3.3. PHASES AND MICROSTRUCTURES

To verify the simulation results presented in this paper, the microstructure of equiatomic AlFeCoNiCu HEA was characterized. SEM micrographs presented in Figure 7 showed two randomly distributed phases (α and β).

Accordingly to Eq. 5 [67, 68], the higher entropy of the alloy system leads to a lower viscosity values:

$$\log \eta = A_e + \frac{B_e}{TS_{config}}, \quad (5)$$

where η is viscosity ($\text{kg s}^{-1}.\text{m}^{-1}$), S_{config} is configurational entropy ($\text{kg.m}^2 \text{s}^{-2}.\text{K}^{-1}$), T is temperature (K), and A_e and B_e are constants which reflect the Gibbs free energy

barriers. The low viscosity and the associated high atomic mobility in HEAs result in a better component mixing in the melt and consequently result in random phase distributions (Figure 7) [56]. Experimental crystal structures of α and β phases were identified using thin-film XRD, Cu $K\alpha$ radiation and the 2θ range from 5° to 90° ; XRD patterns are shown in Figure 8. One bcc (marked as “ β ” in Figure 7) and one fcc (marked as “ α ” Figure 7) phases were identified by XRD at the room temperature.

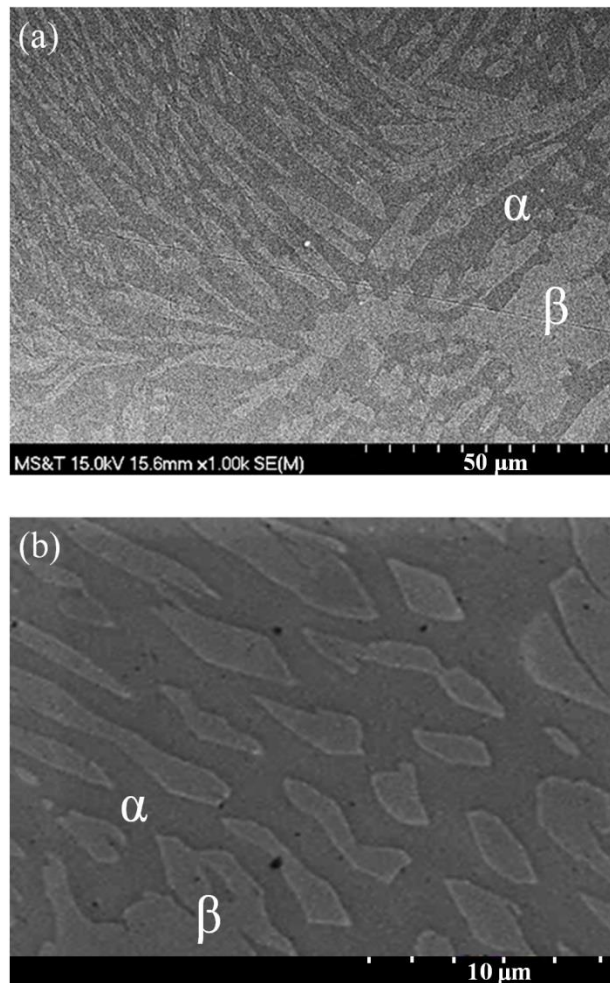


Figure 7. SEM micrographs of as cast equiatomic AlFeCoNiCu: (a) back-scattered electron, and (b) secondary electron pictures.

Rietveld quantitative analysis by HTXRD shows that the weight fraction ratio of fcc to bcc phase increases at 1,170K, however there is still about 10% bcc phase remained in the system. AIMD and phase diagram calculations in previous sections of this article predicted the formation of single fcc phase at this temperature; this can be explained through the sluggish diffusion of atoms in HEAs reported by previous experiments [30], which restrains a complete phase transformation from bcc to fcc. Small amounts of an ordered bcc phase with the same compositions as formed bcc phases (β) are also visible in both XRD patterns in Figure 8. It should be noted that some changes in composition of such HEAs may result in formation of a single phase HEA; for example, recently Zhiqiang Fu et al. reported successful design of $\text{Al}_{7.5}\text{Fe}_{25}\text{Co}_{25}\text{Ni}_{25}\text{Cu}_{17.5}$ HEA with single fcc structure [57].

Figure 9 presents the EBSD maps of as cast equiatomic AlFeCoNiCu alloy. Since there was no available data for indexing the EBSD, the information that was provided by XRD was used. According to the XRD patterns, the lattice parameter of bcc structure in the alloy system was 2.865\AA with Im-3m space group while fcc has 3.603\AA lattice constant and Fm-3m space group (Table 1); these results are in very good agreements with those calculated by AIMD.

The mechanical properties including tensile properties and micro-hardness are also presented in Table 1. The strength (YS and UTS) of AlFeCoNiCu were comparable to chromium-vanadium steels with much less ductility [58]. This shows the brittle behavior of as-cast AlFeCoNiCu alloy. The measured micro-hardness showed a relatively high value with respect to the average of metallic alloys.

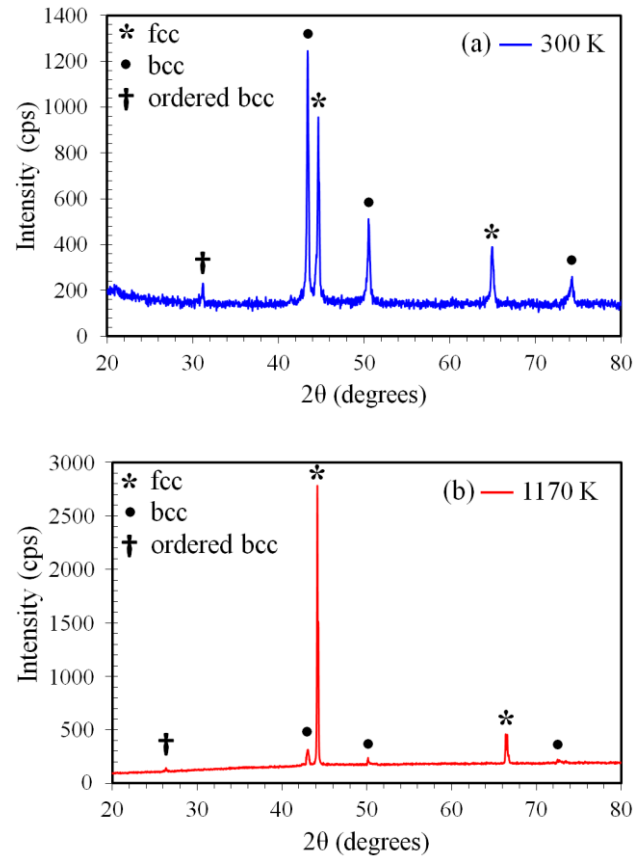


Figure 8. XRD patterns of as cast equiatomic AlFeCoNiCu at (a) room temperature, and (b) 1,170K.

Table 1. Measured properties of as cast equiatomic AlFeCoNiCu alloy.

Phase	Density (g.cm ⁻³)	Lattice (Å)	Yield Strength (MPa)	Ultimate Strength (MPa)	Ultimate Strain (%)	Hardness (HV)
bcc	6.67	2.865	780 ±10	907 ±10	8.2 ±0.2	585 ±5
fcc	8.44	3.603				

The EBSD phase map (Figure 9 (b)) indicated the co-existence of fcc and bcc phases in the microstructure. Furthermore, EBSD inverse pole figure (IPF) coloring map

shows relatively low angel orientation arrangements with respect to the normal direction in Figure 9 (c).

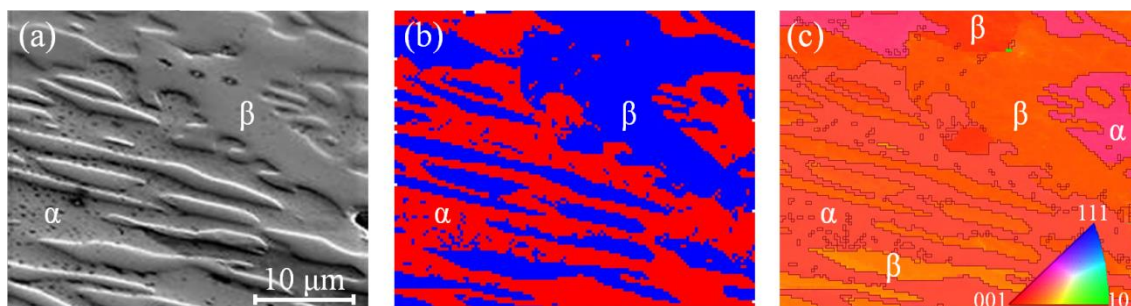


Figure 9. EBSD images: (a) 70° tilt SEM micrograph, (b) fcc (red)/bcc (blue) phase map, and (c) orientation map.

After determining the crystal structures that formed in the alloy system, the question is how the alloying elements are distributed between the different phases. Figure 10 shows the elemental EDS map of equiatomic AlFeCoNiCu HEA providing a qualitative sense of elemental distribution in each phase. According to the chemical composition of phases characterized by EDS analysis presented in Table 2, Fe and Co are almost uniformly distributed in both phases compared to the other elements. Ni and Al have much higher concentrations in bcc phase than fcc phase, while Cu concentration in the fcc phase (α) is much higher than in the bcc phase. The presence of Al in bcc phase and Cu in fcc phase confirms the previous experimental results which report that Al stabilizes bcc phases while Cu stabilizes fcc phases in HEAs [69, 70]; these results also validate the DFT calculations reported in Figure 2.

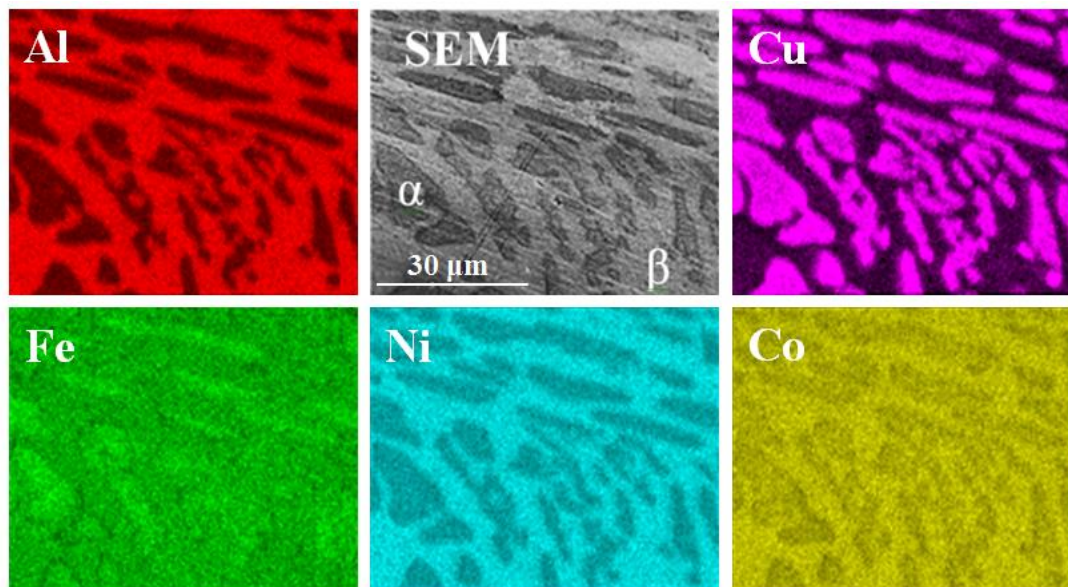


Figure 10. EDS elemental map of equiatomic AlFeCoNiCu. β is the bcc phase and α is the fcc phase.

Table 2. EDS composition analysis of AlFeCoNiCu (at. %)

Phase	Al	Fe	Co	Ni	Cu
α	1.3	29.2	28.5	2.6	38.4
β	25.9	23.1	24.1	24.8	2.1

4. CONCLUSION

Different computational modeling and experimental techniques were utilized to study phase formations in cast AlFeCoNiCu HEAs. DFT and AIMD simulation results predicted the coexistence of one fcc (FeCoCu) phase and one bcc (AlFeCoNi) phase at low temperatures for the equiatomic composition of AlFeCoNiCu. These results also indicated that not all the elements were existed in both phases, such that Cu was present in the fcc phase only, and Al and Ni were present in the bcc phase. This two-phase

coexistence at room temperature was confirmed by phase diagram calculations and experiments (SEM, EBSD and XRD). The EDS elemental map also confirmed the theoretically predicted partitioning of elements in these two phases. AIMD simulation results predicted a polymorphic phase transformation at 1,073 K from the two-phase coexistence to a single fcc phase with the equiatomic composition of AlFeCoNiCu. This phase transformation was also predicted in the calculated phase diagram. However, the HTXRD results also showed a small fraction of retained bcc phase above 1,073 K which is believed to be the result of the sluggish diffusion of atoms in HEAs.

ACKNOWLEDGEMENT

The authors would like to acknowledge the funding support provided by the University of Missouri Research Board. The authors are grateful for the computer time allocation provided by the Extreme Science and Engineering Discovery Environment (XSEDE), award number TG-DMR140008.

REFERENCES

- [1] X.-W. Qiu, Microstructure and properties of AlCrFeNiCoCu high entropy alloy prepared by powder metallurgy, *Journal of Alloys and Compounds* 555 (2013) 246-249.
- [2] Y. Zhang, T.T. Zuo, Z. Tang, M.C. Gao, K.A. Dahmen, P.K. Liaw, Z.P. Lu, Microstructures and properties of high-entropy alloys, *Progress in Materials Science* 61 (2014) 1-93.
- [3] M. Chen, S.-J. Lin, J.-W. Yeh, S.-K. Chen, Y.-S. Huang, C.-P. Tu, Microstructure and Properties of Al_{0.5}CoCrCuFeNiTi_x (x = 0-2) High-Entropy Alloys, (2006).
- [4] J.W. Yeh, S.K. Chen, S.J. Lin, J.Y. Gan, T.S. Chin, T.T. Shun, C.H. Tsau, S.Y. Chang, Nanostructured High-Entropy Alloys with Multiple Principal Elements: Novel Alloy Design Concepts and Outcomes, *Advanced Engineering Materials* 6(5) (2004) 299-303.

- [5] B. Cantor, I. Chang, P. Knight, A. Vincent, Microstructural development in equiatomic multicomponent alloys, *Materials Science and Engineering: A* 375 (2004) 213-218.
- [6] G. Sheng, C.T. LIU, Phase stability in high entropy alloys: formation of solid-solution phase or amorphous phase, *Progress in Natural Science: Materials International* 21(6) (2011) 433-446.
- [7] Y. Zhang, T. Zuo, Y. Cheng, P.K. Liaw, High-entropy alloys with high saturation magnetization, electrical resistivity, and malleability, *Scientific reports* 3 (2013).
- [8] K. Zhang, Z. Fu, J. Zhang, J. Shi, W. Wang, H. Wang, Y. Wang, Q. Zhang, Annealing on the structure and properties evolution of the CoCrFeNiCuAl high-entropy alloy, *Journal of Alloys and Compounds* 502(2) (2010) 295-299.
- [9] C. Zhang, F. Zhang, S. Chen, W. Cao, Computational thermodynamics aided high-entropy alloy design, *JOM* 64(7) (2012) 839-845.
- [10] C. Niu, A. Zaddach, A. Oni, X. Sang, J. Hurt III, J. LeBeau, C. Koch, D. Irving, Spin-driven ordering of Cr in the equiatomic high entropy alloy NiFeCrCo, *Applied Physics Letters* 106(16) (2015) 161906.
- [11] A. Li, X. Zhang, Thermodynamic analysis of the simple microstructure of AlCrFeNiCu high-entropy alloy with multi-principal elements, *Acta Metallurgica Sinica (English Letters)* 22(3) (2009) 219-224.
- [12] M.-H. Tsai, J.-W. Yeh, High-Entropy Alloys: A Critical Review, *Materials Research Letters* (ahead-of-print) (2014) 1-17.
- [13] F. Wang, Y. Zhang, G. Chen, Atomic packing efficiency and phase transition in a high entropy alloy, *Journal of Alloys and Compounds* 478(1) (2009) 321-324.
- [14] X. Yang, H. Yu, Z. Lai, Effects of annealing on microstructure, mechanical and electrical properties of AlCrCuFeMnTi high entropy alloy, *Journal of Wuhan University of Technology-Mater. Sci. Ed.* 28(6) (2013) 1196-1200.
- [15] U. Hsu, U. Hung, J. Yeh, S. Chen, Y. Huang, C. Yang, Alloying behavior of iron, gold and silver in AlCoCrCuNi-based equiatomic high-entropy alloys, *Materials Science and Engineering: A* 460 (2007) 403-408.
- [16] Y.-S. Huang, L. Chen, H.-W. Lu, M.-H. Caid, J.-W. Yeh, Microstructure, hardness, resistivity and thermal stability of sputtered oxide films of AlCoCrCu0.5NiFe high-entropy alloy, (2007).

- [17] X. Ye, M. Ma, Y. Cao, W. Liu, X. Ye, Y. Gu, The Property Research on High-entropy Alloy $\text{Al}_x\text{FeCoNiCuCr}$ Coating by Laser Cladding, *Physics Procedia* 12 (2011) 303-312.
- [18] Y. Lu, Y. Dong, S. Guo, L. Jiang, H. Kang, T. Wang, B. Wen, Z. Wang, J. Jie, Z. Cao, A Promising New Class of High-Temperature Alloys: Eutectic High-Entropy Alloys, *Scientific reports* 4 (2014).
- [19] J.-W. Yeh, Alloy Design Strategies and Future Trends in High-Entropy Alloys, *JOM* 65(12) (2013) 1759-1771.
- [20] É. Fazakas, V. Zadorozhnyy, D. Louzguine-Luzgin, Effect of iron content on the structure and mechanical properties of $\text{Al}_{25}\text{Ti}_{25}\text{Ni}_{25}\text{Cu}_{25}$ and $(\text{AlTi})_{60-x}\text{Ni}_{20}\text{Cu}_{20}\text{Fe}_x$ ($x=15, 20$) high-entropy alloys, *Applied Surface Science* 358 (2015) 549-555.
- [21] A. Pogrebnjak, A.A.e. Bagdasaryan, I. Yakushchenko, V.M. Beresnev, The structure and properties of high-entropy alloys and nitride coatings based on them, *Russian Chemical Reviews* 83(11) (2014) 1027.
- [22] F. Wang, Y. Zhang, Effect of Co addition on crystal structure and mechanical properties of $\text{Ti}_{0.5}\text{CrFeNiAlCo}$ high entropy alloy, *Materials Science and Engineering: A* 496(1) (2008) 214-216.
- [23] T.-T. Shun, C.-H. Hung, C.-F. Lee, The effects of secondary elemental Mo or Ti addition in $\text{Al}_{0.3}\text{CoCrFeNi}$ high-entropy alloy on age hardening at 700°C , *Journal of Alloys and Compounds* 495(1) (2010) 55-58.
- [24] H.R. Sistla, J.W. Newkirk, F.F. Liou, Effect of Al/Ni ratio, heat treatment on phase transformations and microstructure of $\text{Al}_x\text{FeCoCrNi}_{2-x}$ ($x=0.3, 1$) high entropy alloys, *Materials & Design* 81 (2015) 113-121.
- [25] M. Alde' n, S. Mirbt, H.L. Skriver, N. Rosengaard, Surface magnetism in iron, cobalt, and nickel, *Physical Review B Condensed Matter* 46(10) (1992) 6303-6312.
- [26] J.F. Dillinger, R.M. Bozorth, Heat Treatment of Magnetic Materials in a Magnetic Field I. Survey of Iron-Cobalt-Nickel Alloys, *Journal of Applied Physics* 6(9) (1935) 279-284.

- [27] N. Krapivka, S. Firstov, M. Karpets, A. Myslivchenko, Features of phase and structure formation in high-entropy alloys of the AlCrFeCoNiCu x system ($x= 0, 0.5, 1.0, 2.0, 3.0$), *The Physics of Metals and Metallography* 116(5) (2015) 467-474.
- [28] O. Senkov, S. Senkova, C. Woodward, Effect of aluminum on the microstructure and properties of two refractory high-entropy alloys, *Acta Materialia* 68 (2014) 214-228.
- [29] K. Zhang, Z. Fu, J. Zhang, W. Wang, H. Wang, Y. Wang, Q. Zhang, J. Shi, Microstructure and mechanical properties of CoCrFeNiTiAl x high-entropy alloys, *Materials Science and Engineering: A* 508(1) (2009) 214-219.
- [30] K.-Y. Tsai, M.-H. Tsai, J.-W. Yeh, Sluggish diffusion in Co–Cr–Fe–Mn–Ni high-entropy alloys, *Acta Materialia* 61(13) (2013) 4887-4897.
- [31] L. Xie, P. Brault, A.-L. Thomann, J.-M. Bauchire, AlCoCrCuFeNi high entropy alloy cluster growth and annealing on silicon: A classical molecular dynamics simulation study, *Applied Surface Science* 285 (2013) 810-816.
- [32] P. Liaw, T. Egami, Y. Zhang, Radiation Behavior of High-Entropy Alloys for Advanced Reactors, US department of Energy, University of tennessee/ Oak Ridge national Laboratory.
- [33] S.-W. Kao, J.-W. Yeh, T.-S. Chin, Rapidly solidified structure of alloys with up to eight equal-molar elements—a simulation by molecular dynamics, *Journal of Physics: Condensed Matter* 20(14) (2008) 145214.
- [34] M. Widom, W.P. Huhn, S. Maiti, W. Steurer, Hybrid Monte Carlo/molecular dynamics simulation of a refractory metal high entropy alloy, *Metallurgical and Materials Transactions A* 45(1) (2014) 196-200.
- [35] G. Duan, D. Xu, Q. Zhang, G. Zhang, T. Çağın, W.L. Johnson, W.A. Goddard III, Molecular dynamics study of the binary Cu₄₆Zr₅₄ metallic glass motivated by experiments: Glass formation and atomic-level structure, *Physical Review B* 71(22) (2005) Art. No. 224208.
- [36] M.C. Gao, D.E. Alman, Searching for next single-phase high-entropy alloy compositions, *Entropy* 15(10) (2013) 4504-4519.
- [37] C.-Y. Hsu, C.-C. Juan, S.-T. Chen, T.-S. Sheu, J.-W. Yeh, S.-K. Chen, Phase Diagrams of High-Entropy Alloy System Al-Co-Cr-Fe-Mo-Ni, *JOM* 65(12) (2013) 1829-1839.

- [38] F. Zhang, C. Zhang, S.L. Chen, J. Zhu, W.S. Cao, U.R. Kattner, An understanding of high entropy alloys from phase diagram calculations, *CALPHAD* 45 (2014) 1-10.
- [39] Y. Zhang, X. Yang, P. Liaw, Alloy design and properties optimization of high-entropy alloys, *Jom* 64(7) (2012) 830-838.
- [40] S. Wang, Atomic Structure Modeling of Multi-Principal-Element Alloys by the Principle of Maximum Entropy, *Entropy* 15(12) (2013) 5536-5548.
- [41] C.E. Campbell, U.R. Kattner, Z.-K. Liu, The development of phase-based property data using the CALPHAD method and infrastructure needs, *Integrating Materials and Manufacturing Innovation* 3(1) (2014) 1-23.
- [42] U.R. Kattner, The thermodynamic modeling of multicomponent phase equilibria, *JOM* 49(12) (1997) 14-19.
- [43] G. Kresse, J. Furthmüller, Vienna ab initio simulation package (VASP), Vienna: Vienna University (2001).
- [44] C. Ng, S. Guo, J. Luan, S. Shi, C. Liu, Entropy-driven phase stability and slow diffusion kinetics in an Al_{0.5}CoCrCuFeNi high entropy alloy, *Intermetallics* 31 (2012) 165-172.
- [45] F. Otto, Y. Yang, H. Bei, E.P. George, Relative effects of enthalpy and entropy on the phase stability of equiatomic high-entropy alloys, *Acta Materialia* 61(7) (2013) 2628-2638.
- [46] A. Takeuchi, K. Amiya, T. Wada, K. Yubuta, W. Zhang, A. Makino, Entropies in Alloy Design for High-Entropy and Bulk Glassy Alloys, *Entropy* 15(9) (2013) 3810-3821.
- [47] R. Raghavan, K. Hari Kumar, B. Murty, Analysis of phase formation in multi-component alloys, *Journal of Alloys and Compounds* 544 (2012) 152-158.
- [48] C. Bale, E. Bélisle, P. Chartrand, S. Decterov, G. Eriksson, K. Hack, I.-H. Jung, Y.-B. Kang, J. Melançon, A. Pelton, FactSage thermochemical software and databases—recent developments, *Calphad* 33(2) (2009) 295-311.
- [49] J. Tomiska, Mathematical conversions of the thermodynamic excess functions represented by the Redlich-Kister expansion, and by the Chebyshev polynomial series to power series representations and vice-versa, *Calphad* 8(4) (1984) 283-294.

- [50] X. Ye, M. Ma, W. Liu, L. Li, M. Zhong, Y. Liu, Q. Wu, Synthesis and Characterization of High-Entropy Alloy A1 Advances in Materials Science and Engineering 2011 (2011).
- [51] K. Momma, F. Izumi, VESTA: a three-dimensional visualization system for electronic and structural analysis, *Journal of Applied Crystallography* 41(3) (2008) 653-658.
- [52] B. Nestler, H. Garcke, B. Stinner, Multicomponent alloy solidification: Phase-field modeling and simulations, *Physical Review E* 71(4) (2005) 041609.
- [53] L. CompuTherm, Pandat 8.0-phase diagram calculation software for multi-component systems, CompuTherm LLC, Madison, WI 53719 (2008).
- [54] P. Richet, Viscosity and configurational entropy of silicate melts, *Geochimica et Cosmochimica Acta* 48(3) (1984) 471-483.
- [55] A.G. Whittington, M.A. Bouhifd, P. Richet, Amorphous materials: Properties, structure, and durability. The viscosity of hydrous NaAlSi₃O₈ and granitic melts: Configurational entropy models, *American Mineralogist* 94(1) (2009) 1-16.
- [56] Y. Zhang, Y.J. Zhou, J.P. Lin, G.L. Chen, P.K. Liaw, Solid-Solution Phase Formation Rules for Multi-component Alloys, *Advanced Engineering Materials* 10(6) (2008) 534-538.
- [57] Z. Fu, W. Chen, H. Wen, D. Zhang, Z. Chen, B. Zheng, Y. Zhou, E.J. Lavernia, Microstructure and strengthening mechanisms in an FCC structured single-phase nanocrystalline Co₂₅ Ni₂₅ Fe₂₅ Al_{7.5} Cu_{17.5} high-entropy alloy, *Acta Materialia* 107 (2016) 59-71.
- [58] G. Schlieper, F. Thummler, High strength heat-treatable sintered steels containing manganese, chromium, vanadium and molybdenum, *Powder Metall. Int.* 11(4) (1979) 172-176.
- [59] C.-C. Tung, J.-W. Yeh, T.-t. Shun, S.-K. Chen, Y.-S. Huang, H.-C. Chen, On the elemental effect of AlCoCrCuFeNi high-entropy alloy system, *Materials letters* 61(1) (2007) 1-5.
- [60] J.-M. Wu, S.-J. Lin, J.-W. Yeh, S.-K. Chen, Y.-S. Huang, H.-C. Chen, Adhesive wear behavior of Al_xCoCrCuFeNi high-entropy alloys as a function of aluminum content, *Wear* 261(5) (2006) 513-519.

II. GENERALIZED STACKING FAULT ENERGIES, DUCTILITIES, AND TWINNABILITIES OF CoCrFeNi-BASED FACE-CENTERED CUBIC HIGH ENTROPY ALLOYS

M. Beyramali Kivy and M. Asle Zaeem*

Department of Materials Science and Engineering, Missouri University of Science and Technology, 1400 N. Bishop Ave, Rolla, MO 65409, USA

(*Scripta Materialia* 139 (2017) 83-86)

ABSTRACT

Effects of Cu, Mn, Al, Ti, Mo on generalized stacking fault energies, Rice-criterion ductilities, and twinabilities of CoCrFeNi-based face-centered cubic high entropy alloys were investigated using density functional theory calculations. The calculated barrier energies and twinabilities revealed that the addition of Ti, Mo increased the tendency of dislocation glide and deformation twinning, while addition of Mn, Cu and relatively high amount of Al facilitated dislocation gliding and martensitic transformation. Low amount of Al resulted in only dislocation gliding. Furthermore, the addition of Mn and Cu increased the calculated Rice-criterion ductility while other elements decreased it.

Keywords: Generalized stacking fault energy; Twinability; High Entropy Alloys.

High entropy alloys (HEAs), which consist of at least five alloying elements with near equi-atomic compositions, are new class of metallic alloys emerged in the last decade [1, 2]. The majority of the work in this area have tried to develop HEAs with simple microstructures that form few simple random solid solution (RSS) phases (mainly cubic crystal structures) avoiding complex intermetallics or terminal phases [2-7]. HEAs can be designed to have outstanding mechanical, thermal and chemical properties due to

the high entropy effect, intense lattice distortion effect (solution hardening), cocktail effect, and sluggish atomic diffusion effect [1, 2, 8, 9].

Similar to other materials systems, to study the mechanical behavior of HEAs, it is necessary to investigate their deformation mechanisms. Since HEAs, unlike conventional alloys, do not have any dominating element that mainly controls the microstructures, investigating mechanical behaviors of these alloys with respect to the effect of alloying elements is a challenging task. To the best of our knowledge and according to a new review article on HEAs by Miracle and Senkov, there is only one study in the literature that investigated the deformation mechanisms of an specific HEA [1]; Otto et al. showed experimentally that a planar dislocation glide in CoCrFeNiMn system occurs similar to the conventional face-centered cubic (fcc) metals mediating the deformation [10]. There are certainly needs for studies on how the composition of alloys control the deformation mechanisms of HEAs [1]. One practical way to gain knowledge on deformation behavior of materials is to determine their generalized stacking fault energies (GSFE), and in this work we utilize density functional theory (DFT) calculations to determine GSFE of some selected fcc HEAs and study their deformation mechanisms.

There are around 30 different HEA systems reported in the literature which form a single fcc phase [11-17]. In this work, 13 different HEAs with experimentally identified fcc microstructures were selected from the literature in order to study their plastic deformation mechanisms [11-17]. These alloys are listed in Figure 1. It is known that different modes of plastic deformations for fcc metals including dislocation glide, mechanical twinning, and martensitic transformation can be predicted by measuring their GSFE [18, 19].

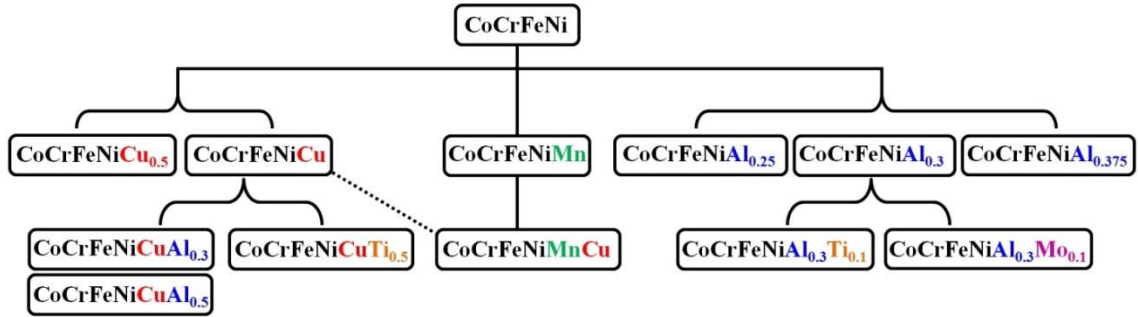


Figure 1. The investigated HEAs in the present work.

Stacking faults are planar defects that can be generated in materials by mechanical deformations [20]. The GSFE of a material is the total energy per unit area to create a complete stacking fault. The first local maximum point in a GSFE curve is the unstable stacking fault energy (USFE) (energy at γ_{USF}) which is the lowest required energy for dislocation nucleation, and the first local minimum energy is the intrinsic stacking fault energy (ISFE) (energy at γ_{ISF}) [21]. Since a material has to overcome the USFE before the occurrence of crystal lattice shearing, calculating both USFE and ISFE is essential to accurately predict the deformation behavior of materials [22, 23]. The second local maximum in a GSFE curve is the unstable twinning energy (UTE) associated with the energy barrier for a rigid displacement along fcc partial dislocation direction on the preexisting ISF [23].

The ISFE can be measured experimentally using different techniques such as transmission electron microscopy (TEM) and x-ray powder diffraction (XRD) [24-26], but USFE and UTE can be determined only by using first principle or atomistic methods such as density functional theory (DFT) and molecular dynamics simulations [27-29]. Both explicit and implicit DFT calculations can be used to determine GSFE, where the

explicit method determines the total energy difference between the perfect and faulted crystals [28, 30, 31], and the implicit method calculates the energies of the fcc, hcp and double hcp to define the SFE of the fcc structures [32, 33]. To the best of our knowledge only ISFE of some HEAs has been studied in previous works [9, 34-36].

In this work, the explicit DFT calculations were employed to study the effects of addition of different alloying elements on the USFE, ISFE, and UTE of CoCrFeNi HEA system. Moreover, the relative energy barrier between USFE and UTE, the Rice-criterion ductilities, and the tendency of twinning (theoretical twinnability) were calculated to further investigate the deformation mechanisms and mechanical properties of the selected fcc HEAs.

The DFT simulations in this work were performed using the Vienna ab initio simulation package (VASP) [37]. Projector augmented wave (PAW) potentials [38, 39], instead of ultra-soft pseudopotentials, and the generalized gradient approximation (GGA) [40, 41] were used to enhance the accuracy of the calculations. The structures were relaxed until the ionic optimization convergence was within 0.001 eV/atom, and then simulations were converged considering the quasi-Newton algorithm and Fermi smearing [42]. The stacking fault, surface and twinning energies were calculated using fcc supercell structures consisted of 108 atoms in total with 9 layers along [111] axis (3 layers of A, B and C stacking sequences) and 12 atoms on each layer (Figure 2). It should be mentioned that the supercell size (atomic number) could slightly vary based on the alloying compositions. The experimental lattice constants (a) for CoCrFeNi, CoCrFeNiCuAl_{0.3}, and CoCrFeNiCuAl_{0.5} are not available, therefore we used the average of the lattice constants of other alloys listed in Table 1: $a = 3.59 \text{ \AA}$; it should be noted that

we ran DFT calculations to test the validity of this assumption, and the results indicated that the lattice constants for these alloys vary between 3.56\AA and 3.59\AA . The atoms of alloying elements were distributed randomly in the fcc supercell structures, and to determine the possible variations in formation energies caused by random position of atoms in the super cell, for each alloy system five to nine random structures were generated and the uncertainty (average deviation) of formation energies was calculated (uncertainty-I). The most stable structure for each alloy was used to determine the GSFE, and to calculate the total uncertainty for each DFT calculated quantity the uncertainty-I was considered as well.

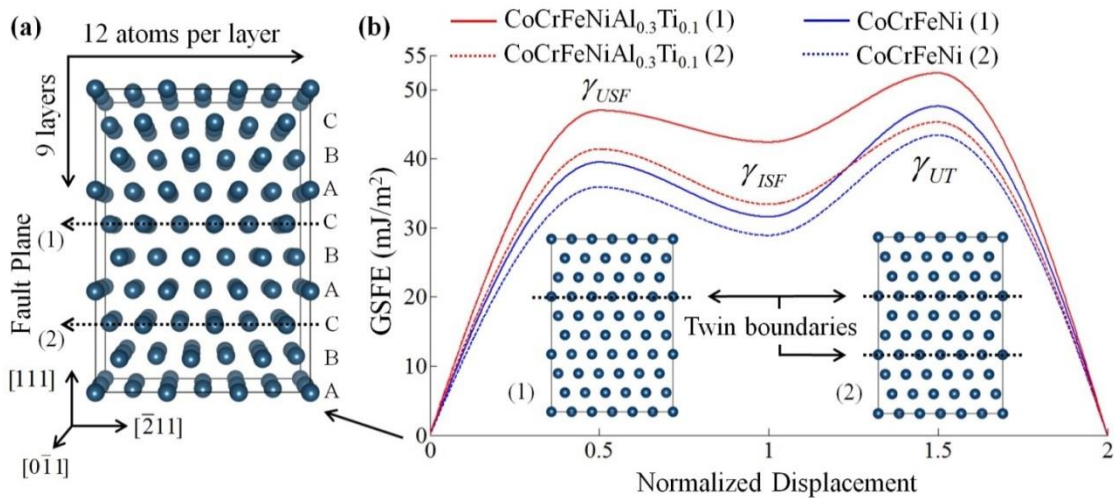


Figure 2. (a) Fcc supercell structure used for calculating the GSFE curves and surface energies (visualized by VESTA [43]). (b) Calculated GSFE curves for CoCrFeNi and CoCrFeNiAl_{0.3}Ti_{0.1} by considering two different fault planes shown in panel (a); subset pictures show twin boundary formation for the two cases.

The stacking faults were imposed to the defect-free fcc structure by a rigid displacement of the atoms above the stacking fault plane along $\langle 211 \rangle$ direction within $\{111\}$ slip plane [44, 45], which results in a $b_p = 1/6 \langle 211 \rangle \{111\}$ partial Burgers vector (a Shockley partial dislocation) [26-28, 46]. Two $b_p = 1/6 \langle 211 \rangle \{111\}$ Shockley partial dislocations form a $a/2 \langle 110 \rangle$ perfect dislocation. An unstable stacking fault (USF) forms due to the shear displacement through half of that Burgers vector, $\gamma_{USF} = a/2 \langle 211 \rangle \{111\}$ [47].

Initially USFE and ISFE were calculated by displacing the atoms on the layers 7th-9th along $[\bar{2}11]$ direction within (111) slip plane, and UTE was calculated by displacing the atoms on the 8th and 9th layers resulting in the creation of a twin region [48]. When different layers along $[\bar{2}11]$ direction within (111) slip plane were considered as fault planes, the calculated GSFE curve was altered due to different compositions of the fault planes. For instance, two examples of the considered stacking fault planes in this work with their corresponding GSFE curves are presented in Figure 2(b). In the previous works to determine the GSFE curve only one layer of atoms in the supercell structure is usually chosen to be the fault plane [28, 48, 49]; the same process was also used for calculating the ISFE of some HEAs [9]. However, since random positions of atoms are generated to construct the supercell for HEAs, choosing a different layer of atoms as the fault plane can influence the GSFE calculation. In this work to determine the effect of selection of different layers as the fault plane on GSFE calculations, for each alloy system GSFE was calculated five times considering five different layers of atoms along $[\bar{2}11]$ direction as fault planes, and the uncertainty (average deviation) of fault energies was calculated

(uncertainty-II). The total uncertainty of DFT calculations was determined by multiplying uncertainty-I and uncertainty-II for different quantities and properties for each alloy system.

Utilizing the DFT explicit approach for non-magnetic state, fault energies were calculated to be the total formation energy difference between defect-free lattice and faulted lattice per unit area:

$$FE (mJ / m^2) = \frac{1.6 \times 10^{-16} (E_0 - E_f)}{A}, \quad (1)$$

where FE is the fault energy (USFE, ISFE, or UTE), E_0 (eV) is the formation energy of the perfect undistorted lattice, E_f (eV) is the total energy of the sheared lattice, and A is the area perpendicular to the stacking fault [27, 50]. Finally, the surface energies were calculated by using a defect-free supercell similar to the Figure 2(a) with an addition of $3a$ vacuum on top of the (111) plane.

USFE, ISFE and UTE were calculated for the HEAs in Figure 1 and the results are presented in Table 1. The total uncertainties varied depending on the alloying compositions. For instance, the alloying elements of CoCrFeNi were almost uniformly distributed on the planes of fcc supercells (Figure 2 (a)), and this resulted in lower values for both uncertainty types (uncertainty-I and uncertainty-II). On the other hand, additions of Al and Ti to CoCrFeNi system led to some differences in compositions of different fault layers resulting in slightly higher amounts of calculated uncertainties (Figure 2 (b)).

According to the calculated stacking fault energies presented in Table 1, addition of Mn and/or Cu to CoCrFeNi decreased both USFE and ISFE which can aid the dislocation mediated slip and martensitic transformation to be the plasticity deformation

mechanism [18]. Addition of relatively high amounts of Al to CoCrFeNi (CoCrFeNiAl_{0.3/0.375}) and CoCrFeNiCu systems (CoCrFeNiCuAl_{0.3/0.5}) slightly decreased the USFE but increased the ISFE higher than that of CoCrFeNi. Addition of relatively low amount of Al (CoCrFeNiAl_{0.25}) increased both USFE and ISFE. Addition of low amounts of Ti and Mo to CoCrFeNiAl_{0.3} and CoCrFeNiCu systems increased the relative USFE and ISFE significantly. To further investigation the plastic deformation mechanisms of these selected HEAs, we calculated the relative barrier energy (difference between UTE and USFE) and twinnability. Therefore, the UTE (γ_{UT}) of these alloys was first calculated, and the results including the uncertainty values are listed in Table 1. The results indicate that additions of all the considered alloying elements to CoCrFeNi system increased the UTE. Additions of Cu (CoCrFeNiCu) and Mn (CoCrFeNiMn) resulted in larger increase in UTE, while additions of Cu-Al (CoCrFeNiCuAl_{0.3}) and Cu-Ti (CoCrFeNiCuTi_{0.5}) led to lower increase in UTE. The relative barrier height ($\delta_{usf}^{''}$) was calculated by [48]:

$$\delta_{usf}^{''} = \gamma_{UT} - \gamma_{USF} . \quad (2)$$

$\delta_{usf}^{''}$ offers an expression to determine whether the partial dislocations can lead to formation of full dislocations causing dislocation mediated slip to be the plastic deformation mechanism, or mechanical twinning become the preferred plasticity mechanism [23, 48]. The results in Table 2 show that the calculated $\delta_{usf}^{''}$ values were positive for all the investigated HEAs meaning energy barriers of unstable twinning formations were larger than energy barriers for nucleation of dislocations.

Table 1. Lattice constants (a) and calculated USFE (γ_{USF}), ISFE (γ_{ISF}) and UTE (γ_{UT}).

alloy	a (Å)	γ_{USF} (mJ/m ²)	γ_{ISF} (mJ/m ²)	γ_{UT} (mJ/m ²)
CoCrFeNi	3.59 ^a	39.5 ± 1.2	31.6 ± 0.9	47.6 ± 1.4
CoCrFeNiCu _{0.5}	3.56 [71]	37.3 ± 2.4	29.0 ± 1.9	51.8 ± 3.3
CoCrFeNiCu	3.58 [72]	34.5 ± 1.6	27.5 ± 1.3	55.2 ± 2.5
CoCrFeNiCuAl _{0.3}	3.59 ^a	39.6 ± 2.6	33.8 ± 2.2	49.3 ± 3.2
CoCrFeNiCuAl _{0.5}	3.59 ^a	38.0 ± 2.5	32.0 ± 2.1	52.1 ± 2.9
CoCrFeNiCuTi _{0.5}	3.58 [72]	45.0 ± 2.9	37.4 ± 2.4	48.7 ± 2.6
CoCrFeNiAl _{0.25}	3.59 [73]	40.1 ± 2.7	38.7 ± 2.6	50.0 ± 3.3
CoCrFeNiAl _{0.3}	3.60 [74]	38.2 ± 2.5	35.2 ± 2.3	53.0 ± 3.5
CoCrFeNiAl _{0.375}	3.60 [73]	35.2 ± 2.4	33.7 ± 2.3	54.1 ± 3.7
CoCrFeNiAl _{0.3} Ti _{0.1}	3.60 [74]	47.0 ± 3.3	42.4 ± 3.0	52.4 ± 3.7
CoCrFeNiAl _{0.3} Mo _{0.1}	3.60 [74]	45.5 ± 3.2	37.2 ± 2.6	51.2 ± 3.6
CoCrFeNiMn	3.59 [75]	38.5 ± 1.5	29.7 ± 1.2	56.6 ± 2.3
CoCrFeNiMnCu	3.59 [75]	36.8 ± 1.5	27.0 ± 1.2	54.0 ± 1.9

^aThe lattice constants for these alloys were not reported in the literature; however since other CoCrFeNi-based alloy systems have very similar lattice constants, the average of their lattice constants (3.59 Å) is used.

This suggests possible domination of plastic deformation by dislocation mediated slip; however, at low positive values of $\delta_{usf}^{'''}$ (e.g., CoCrFeNiCuTi_{0.5}, CoCrFeNiAl_{0.3}Ti_{0.1} and CoCrFeNiAl_{0.3}Mo_{0.1}), the alloys could still form mechanical micro-twins [48]. To further study the possibility of mechanical twinning, theoretical twinnabilities were calculated using Tadmor and Bernstein derivation [51]. This theory measures the propensity of polycrystalline fcc metals to form deformation twinning.

$$\tau_a = \left[1.136 - 0.151 \frac{\gamma_{ISF}}{\gamma_{USF}} \right] \sqrt{\frac{\gamma_{USF}}{\gamma_{UT}}}. \quad (3)$$

Table 2. Calculated relative barrier height (δ_{usf}^{ut}), theoretical twinnability (τ_a),₍₁₁₁₎ surface energy (γ_s), and Rice-criterion ductility (D).

alloy	δ_{usf}^{ut} (mJ/m ²)	τ_a	γ_s (mJ/m ²)	D
CoCrFeNi	8.1 ± 0.3	0.83 ± 0.09	156.9 ± 11	1.19 ± 0.03
CoCrFeNiCu _{0.5}	14.5 ± 0.9	0.76 ± 0.10	211.2 ± 24	1.69 ± 0.08
CoCrFeNiCu	20.7 ± 0.9	0.71 ± 0.07	193.8 ± 14	1.68 ± 0.05
CoCrFeNiCuAl _{0.3}	9.6 ± 0.7	0.83 ± 0.07	197.5 ± 23	1.49 ± 0.07
CoCrFeNiCuAl _{0.5}	14.1 ± 0.4	0.79 ± 0.07	160.2 ± 18	1.27 ± 0.09
CoCrFeNiCuTi _{0.5}	3.6 ± 0.3	0.89 ± 0.08	195.1 ± 22	1.30 ± 0.07
CoCrFeNiAl _{0.25}	9.9 ± 0.6	0.87 ± 0.02	153.9 ± 18	1.15 ± 0.06
CoCrFeNiAl _{0.3}	14.8 ± 1.0	0.81 ± 0.04	136.3 ± 16	1.07 ± 0.06
CoCrFeNiAl _{0.375}	18.9 ± 1.2	0.78 ± 0.02	123.4 ± 16	1.05 ± 0.05
CoCrFeNiAl _{0.3} Ti _{0.1}	5.4 ± 0.4	0.90 ± 0.05	159.6 ± 18	1.02 ± 0.06
CoCrFeNiAl _{0.3} Mo _{0.1}	5.7 ± 0.4	0.86 ± 0.09	153.7 ± 19	1.01 ± 0.09
CoCrFeNiMn	18.1 ± 0.7	0.73 ± 0.10	187.8 ± 15	1.46 ± 0.04
CoCrFeNiMnCu	17.2 ± 0.4	0.72 ± 0.10	183.5 ± 20	1.50 ± 0.05

Increasing τ_a increases the tendency of twinning formation [48]. The results in Table 2 revealed that addition of Cu, Mn and relatively high amounts of Al (CoCrFeNiAl_{0.3}, _{0.375}) decreased τ_a , while Ti or Mo increased the tendency to form mechanical twins. Addition of relatively low amount of Al (CoCrFeNiAl_{0.25}) increased both δ_{usf}^{ut} and τ_a . Addition of Cu and Al increased δ_{usf}^{ut} and decreased τ_a . Based on the calculated results, the alloys with higher δ_{usf}^{ut} had lower τ_a suggesting that dislocation mediated slip and martensitic transformation would likely dominate the plastic deformation of those alloys. High δ_{usf}^{ut} and low τ_a for CoCrFeNiMn system suggested that dislocation glide would probably dominate the deformation mechanism rather than

mechanical twinning which is consistent with experimental analysis available in the literature [10]. On the other hand, for the alloys with low positive δ_{usf}^{ut} and high τ_a , the stress intensity at nucleation sites of partial dislocations would be the determining factor for twinning to occur [48].

Finally to investigate how the addition of different alloying elements changes the ductility of CoCrFeNi system, Rice-criterion ductility analysis was utilized [52]. This analysis explains the competition between formation of dislocations from the crack tip and crack cleavage.

$$D = 0.3 \frac{\gamma_s}{\gamma_{USF}}, \quad (4)$$

where D is the ductility parameter and γ_s is the surface energy along [111] axis. According to this analysis, when $D > 1$, the material will be ductile under Mode I (opening mode) loading due to the smaller dislocation nucleation energy compared with the crack cleavage energy barrier; for $D < 0.3$ (or $\gamma_s < \gamma_{USF}$), the material will fail by crack cleavage instead of dislocation mediated slip [48, 53]. The calculated ductilities listed in Table 2 showed that $D > 1$ for all the alloys suggesting formation of dislocations from the crack tip. Addition of Cu and/or Mn in CoCrFeNi matrix increased the Rice-criterion ductilities, while Al, Ti and Mo decreased the ductilities. These results are consistent with the calculated or experimental results that have been published in literature for other alloy systems [54-56].

In conclusion, this work studied the effects of addition of Cu, Mn, Al, Ti, Mo alloying elements on plastic deformation mechanisms of selected CoCrFeNi-based HEAs which were reported in the literature to have a single fcc phase. The GSFE curves, Rice-

criterion ductilities, relative barrier heights, and theoretical twinnabilities were calculated.

The results are summarized as below:

- Addition of Mn, Cu, or relatively high amounts of Al (>0.3) promotes dislocation mediated slip and martensitic transformation. On the other hand, alloys containing Ti or Mo are likely to exhibit dislocation glide and mechanical twinning.
- Plastic deformation mechanism by addition of low amount of Al to CoCrFeNi (CoCrFeNiAl_{0.25}) is likely to be dislocation gliding.
- Addition of Mn and Cu increased the Rice-criterion ductilities aiding emission of dislocations from the crack tip, while Al, Mo or Ti decreased the Rice-criterion ductilities aiding crack cleavage.

ACKNOWLEDGMENTS

The authors would like to acknowledge the funding support provided by the University of Missouri Research Board to complete this work. The supercomputer time allocation for completing the DFT calculations was provided by the Extreme Science and Engineering Discovery Environment (XSEDE), award number TG-DMR140008. The authors are thankful for helpful suggestions provided by Dr. Amitva Moitra, Dr. Krista Limmer, and Prof. Michael Baskes.

REFERENCES

- [1] D. Miracle, O. Senkov, *Acta Materialia* 122 (2017) 448-511.
- [2] M.-H. Tsai, J.-W. Yeh, *Materials Research Letters* (ahead-of-print) (2014) 1-17.
- [3] C. Niu, A. Zaddach, A. Oni, X. Sang, J. Hurt III, J. LeBeau, C. Koch, D. Irving, *Applied Physics Letters* 106(16) (2015) 161906.

- [4] A. Li, X. Zhang, *Acta Metallurgica Sinica (English Letters)* 22(3) (2009) 219-224.
- [5] M. Beyramali Kivy, M. Asle Zaeem, S. Lekakh, *Materials & Design* (2017).
- [6] A. Marshal, K. Pradeep, D. Music, S. Zaefferer, P. De, J. Schneider, *Journal of Alloys and Compounds* 691 (2017) 683-689.
- [7] M. Gao, D. Alman, *Entropy* 15(10) (2013) 4504.
- [8] K.-Y. Tsai, M.-H. Tsai, J.-W. Yeh, *Acta Materialia* 61(13) (2013) 4887-4897.
- [9] S. Huang, W. Li, S. Lu, F. Tian, J. Shen, E. Holmström, L. Vitos, *Scripta Materialia* 108 (2015) 44-47.
- [10] F. Otto, A. Dlouhý, C. Somsen, H. Bei, G. Eggeler, E.P. George, *Acta Materialia* 61(15) (2013) 5743-5755.
- [11] X. Wang, Y. Zhang, Y. Qiao, G. Chen, *Intermetallics* 15(3) (2007) 357-362.
- [12] B. Cantor, *Entropy* 16(9) (2014) 4749-4768.
- [13] C.-M. Lin, H.-L. Tsai, *Journal of Alloys and Compounds* 489(1) (2010) 30-35.
- [14] H.-P. Chou, Y.-S. Chang, S.-K. Chen, J.-W. Yeh, *Materials Science and Engineering: B* 163(3) (2009) 184-189.
- [15] T.-T. Shun, C.-H. Hung, C.-F. Lee, *Journal of Alloys and Compounds* 495(1) (2010) 55-58.
- [16] T.-T. Shun, C.-H. Hung, C.-F. Lee, *Journal of Alloys and Compounds* 493(1) (2010) 105-109.
- [17] X. Yang, Y. Zhang, *Materials Chemistry and Physics* 132(2) (2012) 233-238.
- [18] D.T. Pierce, J.A. Jiménez, J. Bentley, D. Raabe, J.E. Wittig, *Acta Materialia* 100 (2015) 178-190.
- [19] F. Lécroisey, A. Pineau, *Metallurgical and Materials Transactions B* 3(2) (1972) 391-400.
- [20] W.D. Callister, D.G. Rethwisch, *Materials science and engineering: an introduction*, Wiley New York 2007.
- [21] C. Wang, H. Wang, T. Huang, X. Xue, F. Qiu, Q. Jiang, *Scientific reports* 5 (2015).
- [22] A. Hunter, I. Beyerlein, T. Germann, M. Koslowski, *Physical Review B* 84(14) (2011) 144108.

- [23] H. Van Swygenhoven, P. Derlet, A. Frøseth, *Nature materials* 3(6) (2004) 399-403.
- [24] L. Remy, *Acta metallurgica* 25(2) (1977) 173-179.
- [25] M. Moallemi, A. Zarei-Hanzaki, A. Mirzaei, *Journal of Materials Engineering and Performance* 24(6) (2015) 2335-2340.
- [26] A. Das, *Metallurgical and Materials Transactions A* 47(2) (2016) 748-768.
- [27] E. Asadi, M.A. Zaeem, A. Moitra, M.A. Tschopp, *Journal of Physics: Condensed Matter* 26(11) (2014) 115404.
- [28] K. Limmer, J. Medvedeva, D. Van Aken, N. Medvedeva, *Computational Materials Science* 99 (2015) 253-255.
- [29] R. Xiong, H. Peng, H. Si, W. Zhang, Y. Wen, *Materials Science and Engineering: A* 598 (2014) 376-386.
- [30] T. Hickel, A. Dick, B. Grabowski, F. Körmann, J. Neugebauer, *steel research international* 80(1) (2009) 4-8.
- [31] N. Medvedeva, M. Park, D.C. Van Aken, J.E. Medvedeva, *Journal of Alloys and Compounds* 582 (2014) 475-482.
- [32] P. Denteneer, W. van Haeringen, *Journal of Physics C: Solid State Physics* 20(32) (1987) L883.
- [33] A. Reyes-Huamantínco, P. Puschnig, C. Ambrosch-Draxl, O.E. Peil, A.V. Ruban, *Physical Review B* 86(6) (2012) 060201.
- [34] A. Zaddach, C. Niu, C. Koch, D. Irving, *Jom* 65(12) (2013) 1780-1789.
- [35] J. Liu, C. Chen, Y. Xu, S. Wu, G. Wang, H. Wang, Y. Fang, L. Meng, *Scripta Materialia* 137 (2017) 9-12.
- [36] N.L. Okamoto, S. Fujimoto, Y. Kambara, M. Kawamura, Z.M. Chen, H. Matsunoshita, K. Tanaka, H. Inui, E.P. George, *Scientific reports* 6 (2016).
- [37] J. Hafner, *Journal of computational chemistry* 29(13) (2008) 2044-2078.
- [38] P.E. Blöchl, *Physical Review B* 50(24) (1994) 17953.
- [39] G. Kresse, D. Joubert, *Physical Review B* 59(3) (1999) 1758.
- [40] J.P. Perdew, K. Burke, M. Ernzerhof, *Physical review letters* 77(18) (1996) 3865.
- [41] D.M. Ceperley, B. Alder, *Physical Review Letters* 45(7) (1980) 566.

- [42] G. Kresse, O. Marsman, J. Furthmuller, <http://cms.mpi.univie.ac.at/vasp/vasp.pdf> Retrieved April (2016).
- [43] K. Momma, F. Izumi, *Journal of Applied Crystallography* 41(3) (2008) 653-658.
- [44] J.A. Zimmerman, H. Gao, F.F. Abraham, *Modelling and Simulation in Materials Science and Engineering* 8(2) (2000) 103.
- [45] V. Vitek, *Philosophical Magazine* 18(154) (1968) 773-786.
- [46] J. Wang, H. Huang, *Applied physics letters* 85(24) (2004) 5983-5985.
- [47] S. Kibey, J. Liu, M. Curtis, D. Johnson, H. Sehitoglu, *Acta materialia* 54(11) (2006) 2991-3001.
- [48] D.J. Siegel, *Applied Physics Letters* 87(12) (2005) 121901.
- [49] S. Kibey, J. Liu, D.D. Johnson, H. Sehitoglu, *Applied Physics Letters* 89(19) (2006) 191911.
- [50] J.G. Lee, *Computational materials science: an introduction*, Crc Press 2011.
- [51] E. Tadmor, N. Bernstein, *Journal of the Mechanics and Physics of Solids* 52(11) (2004) 2507-2519.
- [52] J.R. Rice, *Journal of the Mechanics and Physics of Solids* 40(2) (1992) 239-271.
- [53] S. Shi, L. Zhu, H. Zhang, Z. Sun, *Materials Letters* 189 (2017) 310-312.
- [54] M.J. Mehl, D.A. Papaconstantopoulos, N. Kioussis, M. Herbranson, *Physical Review B* 61(7) (2000) 4894.
- [55] X. Li, D. Dou, Z. Zheng, J. Li, *Journal of Materials Engineering and Performance* 25(6) (2016) 2164-2169.
- [56] Z. Wang, M. Wu, C. Zhonghou, S. Chen, I. Baker, *Intermetallics* 75 (2016) 79-87

III. CURRENT CAPABILITIES IN THERMODYNAMIC CALCULATIONS OF PHASE DIAGRAMS OF HIGH ENTROPY ALLOYS

M. Beyramali Kivy¹, H. Waggoner¹, M.A. Allen², M. Asle Zaem^{1,2 *}

¹Department of Materials Science and Engineering, Missouri University of Science and Technology, 1400 N. Bishop Ave, Rolla, MO 65409, USA

²Department of Mechanical and Aerospace Engineering, Missouri University of Science and Technology, 400 W. 13th St, Rolla, MO 65409, USA

(This manuscript is under preparation for submission to *CALPHAD* journal)

ABSTRACT

Capabilities of different thermodynamic tools were investigated to calculate the phase diagrams of high entropy alloys. A modified CALPHAD approach combined with Muggianu's method and ab initio molecular dynamics (AIMD) simulations is developed in Matlab to calculate the phase diagrams of different HEAs. The results were compared to three different commercial software packages, FactSage, Thermo-Calc and Pandat, as well as experimental phase diagrams. The calculated binary and ternary phase diagrams using the three commercial software packages were fairly consistent with the experimental phase diagrams. However, for high entropy alloys, the results were not similar to the experimental phase diagrams. On the other hand, the proposed approach produced more reliable phase diagrams for high entropy alloys.

Keywords: High Entropy Alloys; Phase Diagram; Phase Formation, CALPHAD, *ab initio* molecular dynamics.

1. INTRODUCTION

High Entropy Alloys (HEAs) are a new concept of multicomponent metallic alloys and are defined as alloys containing five or more principal elements with near

equi-atomic compositions [1]. HEAs can be designed to exhibit favorable properties such as high strength/hardness, outstanding wear resistance, exceptional high-temperature strength, good structural stability, and good corrosion/oxidation resistance [2]. Though these alloys can be compositionally complex, they tend to form simple phases, mostly cubic [3]. High mixing entropy ($\Delta S_{mix} \geq 1.6R$) and low (near zero) mixing enthalpy ($-40 \leq \Delta H_{mix} \leq 15$ kJ/mol) in HEAs lowers the free energy of random solid solution (RSS) phases and facilitates their formation [1, 4]. Moreover, low atomic radii differences between the constituent elements endorse the atomic diffusion and demote the elemental segregations [2, 4, 5].

Due to the multiprinciple elements in HEAs, designing these alloys to achieve the desired properties is a challenging task. In addition to severe lattice distortions and very sluggish elemental diffusions due to different neighboring atomic sites in each lattice [6, 7], cocktail effects and high order elemental interactions make designing these alloys difficult [2, 4]. Therefore, fundamental studies on microstructure evolutions, phase formations and structural transformations of these alloys are required.

Similar to other multicomponent alloys, microstructures of HEAs essentially affect their mechanical, thermal, and chemical properties. Therefore, calculating the equilibrium phase diagrams of these alloys can provide necessary information for designing HEAs with preferred properties. Phase diagrams show which phases will form in a material with respect to temperature as composition changes. The stable phases in the phase diagrams describe distinct atomic bonding and arrangement of elements in a material with a chemical composition [8]. Phase diagrams can be produced experimentally; however, it is a costly procedure and is sensitive to the process factors

[9]. Therefore, theoretical calculations of the phase diagrams are necessary to study the phase formations of the materials at their equilibrium states [8, 10, 11].

In this work, the phase diagrams of metallic alloys including Co-Cr binary and Cr-Ni-Fe ternary, Co-Cr-Fe-Mn-Ni and Al-Co-Cr-Fe-Mo-Ni HEAs were studied utilizing FactSage [12], Thermo-Calc [13], and integrated multicomponent CALPHAD method [4, 14] with first principle approach.

2. METHODOLOGY

Phase diagram modules of FactSage 7.0 and Thermo-Calc 2017 with different databases were utilized to study the phase diagrams in this work. For each phase diagram, the pressure was set to one atmosphere and no gas phases were considered. The liquid phase was set to be a single phase, instead of possible two immiscible liquids. In FactSage 7.0, the database FSstel and For Thermo-Calc 2017, the databases TCFE9: Steels/Fe-Alloys V9.0 and TCHEA2: High Entropy Alloys V2.0 were considered. The selected phases for each phase diagram were the default phases in each database.

The thermodynamic method developed in this work uses combinations of the CALPHAD technique, and *ab initio* molecular dynamics approach. The phase diagrams of AlFeCoNiCu HEA were previously investigated using the sublattice CALPHAD methods and Muggianu's approach [4]. In this approach, the formation energies of different phases in multicomponent systems can be calculated considering reference, ideal solution, and thermodynamic extrapolation of excess Gibbs free energies of the constituent elements [4, 14]. Equation 2 shows the ternary free energy using this method [4, 14]:

$$G^{Phase} = G^{reference} + G^{ideal} + G^{excess} , \quad (1)$$

$$G^{Phase - Ternary} = \sum x_i G_i^0 + RT \sum x_i \ln(x_i) + \sum \sum x_i x_j \sum_{m=0}^n G_m^{ij} (x_i - x_j)^m , \quad (2)$$

where x_i is the molar fraction of component i , R is the gas constant (J/mol.K), T is the temperature (K), $\sum_{m=0}^n G_m^{ij} (x_i - x_j)^m$ is Redlich-Kister polynomial which n is the number of elements [15]. In Equation 2, different crystal structures can be taken into account considering local atomic arrangements such as short range ordering and order-disorder transitions. The Redlich-Kister polynomial can be written based on configurational entropy and binary interactions (L^m) [16].

The combination of sublattice CALPHAD and Muggianu's methods were utilized to study the phase diagrams of five-component AlFeCoNiCu HEA recently [4]. In the sublattice CALPHAD approach, the Gibbs free energies for different crystal structures are determined by [17]:

$$G = \sum_i y_i^1 G_{iz}^o + RT \sum_i y_i^1 \ln y_i^1 + \sum_i \sum_{j>i} y_i^1 y_j^1 \sum_v L_{ij}^v (y_i^1 - y_j^1)^v , \quad (3)$$

where y_i^1 is known as site fraction and describes the fractional site occupation of each of the components on different sublattices [17].

The accuracy of this approach significantly decreases as the number of constituent elements increases. Moreover, the complexity of this approach dramatically increases for considering more complex structures such as intermetallics or rhombohedral structures.

Electronic or atomistic simulation methods, including first principle approach and classical molecular dynamics (MD) simulations, can be utilized as alternative techniques

to calculate the formation of stable phases as functions of temperature and compositions. Due to the potential limitations in MD methods for multicomponent systems, first principle approach can be appropriately applied.

In this work, first principle approaches including density functional theory (DFT) and *ab initio* molecular dynamics (AIMD) were applied to calculate the formation energies of different phases at various temperatures. Since these approaches, especially AIMD, are computationally expensive, they were integrated with CALPHAD solution method and Muggianu's extrapolation to be able to calculate the formation energies of different phases with various constituent elements, compositions, and temperatures. The formation energies of binary phases were calculated using AIMD methods at different temperatures considering different crystal structures, and then the results were inserted into the Redlich-Kister part of the multicomponent CALPHAD method as excess Gibbs free energies. Therefore, the multicomponent CALPHAD method in this work utilized the formation energies calculated by AIMD to determine the Gibbs free energies of different phases at various temperatures considering reference Gibbs free energy, ideal solutions, and excess energies. In this proposed method, the reference Gibbs free energies were extracted from Factsage databases.

The DFT and AIMD simulations in this work were performed using the Vienna *ab initio* simulation package (VASP) [18] considering at least 40 atoms. Projector augmented wave (PAW) potentials [19, 20] were used, and exchange correlation functions were analyzed using the Perdew-Burke-Ernzerhof (PBE) generalized gradient approximation (GGA) [21-23] for increased results accuracy. In DFT calculations, the structures were relaxed until the ionic optimization convergence was within 0.001

eV/atom, and equilibrium lattice constants were determined. The AIMD calculations were performed considering NPT Langevin ensemble (constant number of atoms, isobar, isothermal) to allow the unit-cell volume to relax as the temperature rose [24].

3. RESULTS AND DISCUSSION

To investigate the capabilities of the tested commercial software and modified CALPHAD method in calculating the metallic alloys phase diagrams, various binary alloys were tested. The results for Co-Cr binary system as one example of the investigated binary systems have been presented in Figure 1. The calculated phase diagrams using Pandat [25], FactSage, and Thermo-Calc were consistent and resembled the experimental phase diagram [26]. FSteel and TCFE9: Steels/Fe-Alloys v9.0 databases were used in FactSage and Thermo-Calc respectively to calculate the phase diagrams shown in Figure 1. Ternary phase diagrams for number of metallic systems were also investigated. The results for Cr-Fe-Ni ternary alloy calculated using FactSage and Thermo-Calc are shown in Figure 2 for 700 °C and 1100 °C. As shown in Figure 2, the calculated results were consistent with the experiments for both temperatures. The calculated results for binary and ternary phase diagrams revealed the competence of the studied commercial databases in predicting the phase diagrams of binary and ternary systems. However, the calculated phase diagrams were not completely similar to the experimental phase diagrams. The phase diagrams of some HEAs as specific multicomponent metallic alloys were calculated as well. Due to the limitations of some of the phase diagram software to include more than three different elements as variable compositions, changing the compositions of only two elements with respect to one

another with constant concentrations of the other elements, have been suggested in the literature [25].

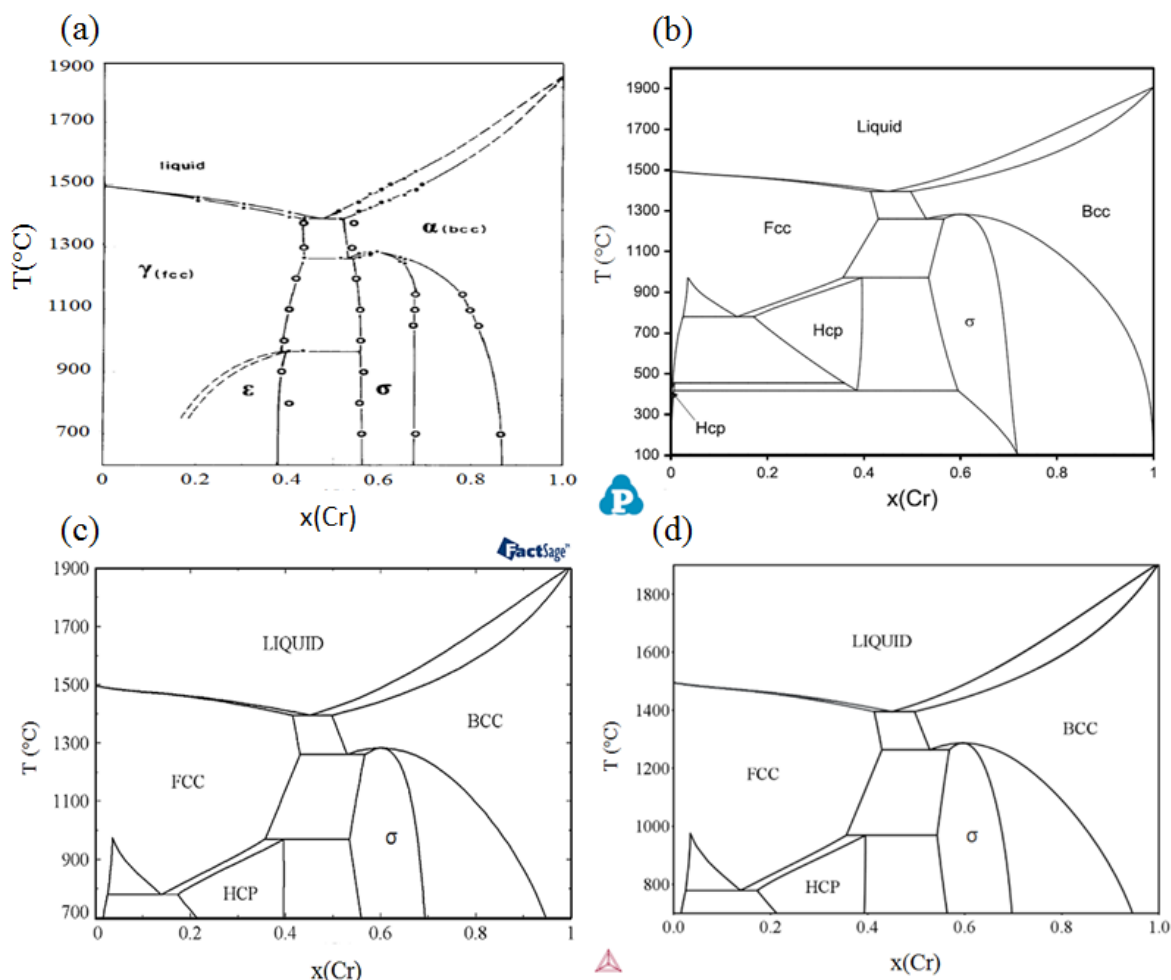


Figure 1. Binary phase diagrams of Co-Cr system, (a) experimental determined from [26], (b) calculated with Pandat from [25], (c) calculated in this work using FactSage and (d) calculated in this work using ThermoCalc.

Figure 3(a) shows the calculated phase diagram of $\text{Fe}_{0.2}\text{Mn}_{0.2}\text{Ni}_{0.2}\text{Cr}_x\text{Co}_{(0.4-x)}$ HEA systems published by F. Zhang *et. al.* [25]. The same HEA systems were studied in this work and the corresponding phase diagram were calculated using FactSage and ThermoCalc (Figure 3 (b) to (d)).

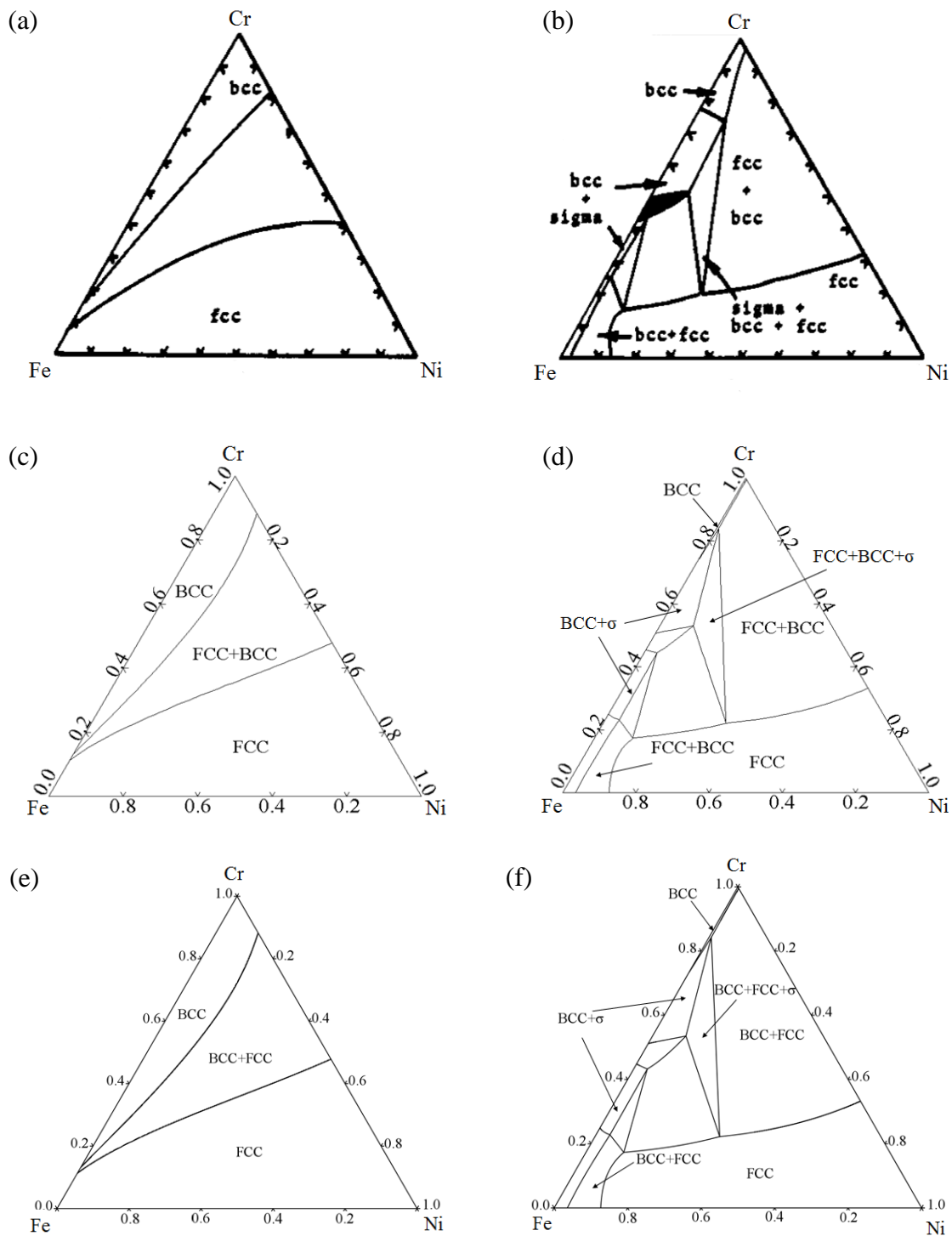


Figure 2. Ternary phase diagrams of Cr-Fe-Ni system, (a) and (b) experimentally determined at 1100 °C and 700 °C respectively from [27], (c) and (d) calculated in this work using FactSage at 1100 °C and 700 °C respectively, (e) and (f) calculated in this work using ThermoCalc at 1100 °C and 700 °C respectively.

The proposed thermodynamic method in this work was also applied to calculate the phase diagram (Figure 3 (e)). As shown in Figure 3, the predicted phases in the calculated phase diagrams were not consistent. Since the experimental phase diagram for the $\text{Fe}_{0.2}\text{Mn}_{0.2}\text{Ni}_{0.2}\text{Cr}_x\text{Co}_{(0.4-x)}$ HEA systems were not available, the accuracy of the calculated results was unidentified. Although all the compositions in the calculated phase diagrams in Figure 3 can fit into HEA principle standards, they do not represent the classical definition of the phase diagrams where the concentration of one element changes with respect to all other alloying elements.

Therefore, the $\text{AlCoCrFeMo}_{0.5}\text{Ni}$ HEA system was selected to calculate the phase diagrams, and the results were compared to the available experimentally determined phase diagrams [28]. TCHEA2: HEA v0.2 database of Thermo-Calc software was used for the illustrated results in Figure 4 (b) and (c). As seen in Figure 4 (b), the results calculated using Thermo-Calc did not resemble the experimental phase diagram. Thus, in Figure 4 (c), only the phases that existed in the experimental phase diagram (fcc, B2, and σ) were considered in the calculations. However, the resulted phase diagram was still not confirmable by the experiment (Figure 4 (a)). On the other hand, the calculated phase diagram using the proposed thermodynamic model showed more consistent result compared to the experimental phase diagram. The experimentally determined presented in Figure 4 (a) shows the microstructure consisted of B2 and σ phase at for up to ~28 at% of the cobalt concentration. Also, a partial solid state phase transformation can be seen at mid-melting temperature (800 °C) and medium concentrations of cobalt (~15 to ~28 at%).

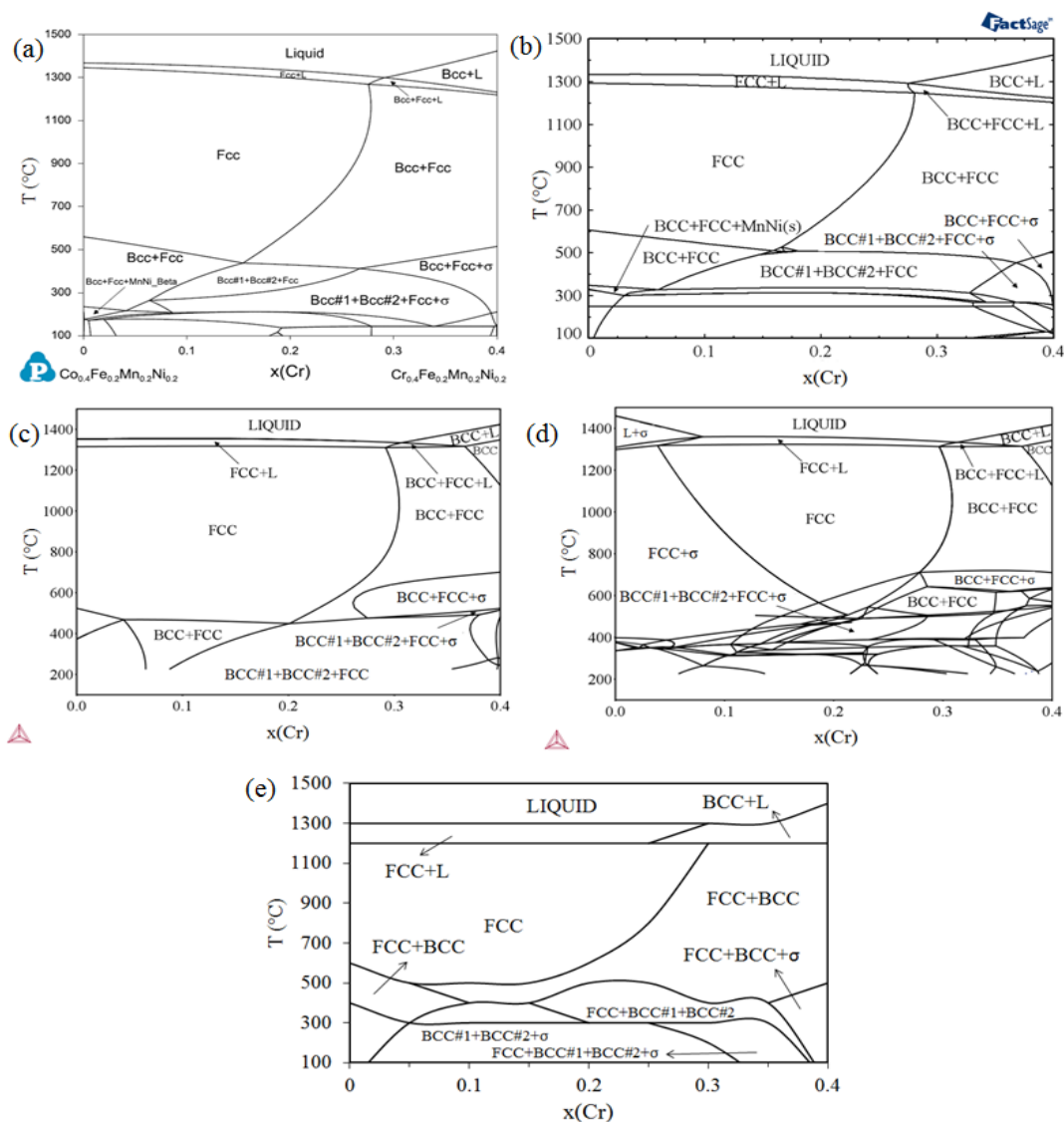


Figure 3. Phase diagrams of $\text{Fe}_{0.2}\text{Mn}_{0.2}\text{Ni}_{0.2}\text{Cr}_x\text{Co}_{(0.4-x)}$ HEA systems, (a) calculated with Pandat from [25], (b) calculated in this work using FactSage, (c) calculated in this work using ThermoCalc Fe-alloys database, (d) calculated in this work using ThermoCalc TCHEA: HEA v2.0 database, and (e) calculated utilizing the proposed thermodynamic method in this work.

However, in the calculated phase diagram illustrated in Figure 4 (d), a complete phase transformation from B2 to fcc and a partial phase transformation were predicted for low and medium/high amounts of cobalt.

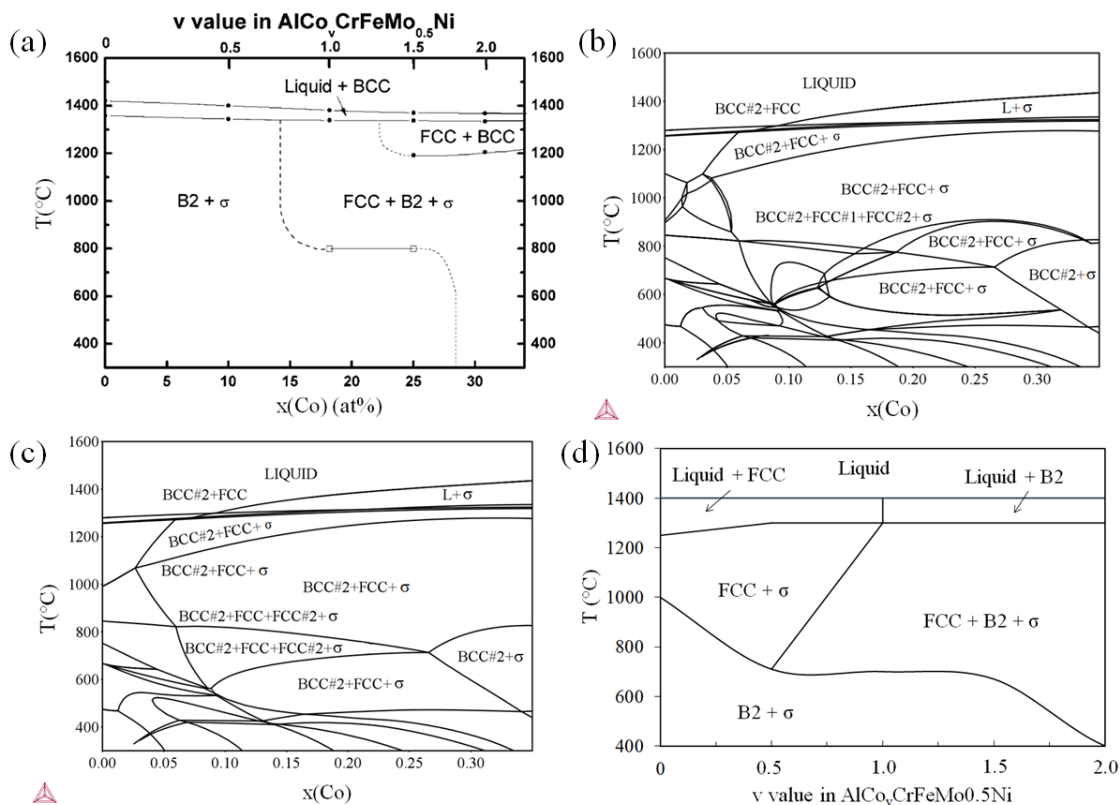


Figure 4. Phase diagrams of AlCo_vCrFeMo_{0.5}Ni HEA, (a) experimentally determined from Ref. [28], (b) calculated in this work using ThermoCalc HEA v2.0 database with no phase filtration, (c) calculated in this work using ThermoCalc HEA v2.0 database considering only the phases in experimental phase diagram, (d) calculated using the thermodynamic approach proposed in this work.

This inconsistency between the experimental and calculated equilibrium phase diagrams can be explained by the sluggish kinetics of HEAs [7]. Thus, the solid state phase transformation that was predicted by equilibrium phase diagram may not occur experimentally. This phenomenon was also observed previously in the literature as well [4]. To further examine the capability of this proposed thermodynamic method in calculating the phase diagrams of HEAs, other experimental phase diagrams from Ref. [28] were also calculated. The results are presented in Figure 5.

As shown in Figure 5 (c) to (f), the same type of total/partial solid state phase transformations were predicted in the calculated phase diagrams which did not completely resemble the experimental observations.

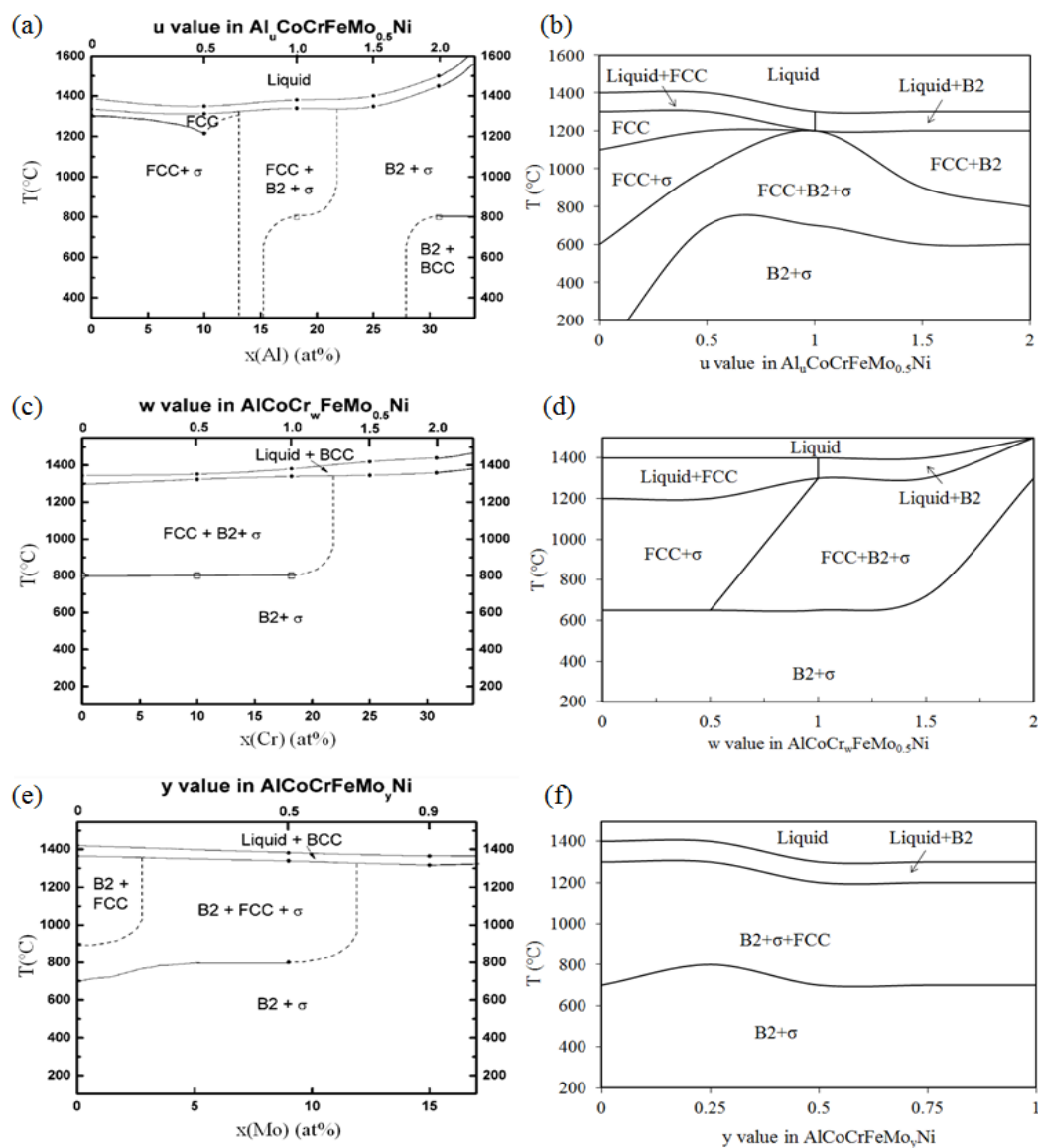


Figure 5. (a) Experimentally determined phase diagram from Ref. [28] and (b) Calculated phase diagram of $\text{Al}_u\text{CoCrFeMo}_{0.5}\text{Ni}$ HEAs, (c) Experimentally determined phase diagram from Ref. [28] and (d) Calculated phase diagram of $\text{AlCoCr}_w\text{FeMo}_{0.5}\text{Ni}$ HEAs, (e) Experimentally determined phase diagram from Ref. [28] and (f) Calculated phase diagram of $\text{AlCoCrFeMo}_y\text{Ni}$ HEAs.

Since, Al is a non-transition metal and the bonding orbitals as well as heat of compound formations differ between transition and non-transition metals [29], the addition of Al can lead to relatively more complex phase diagrams [4]. For instance, in the experimentally determined phase diagram [28] shown in Figure 5 (a), fcc and σ for lower amounts of Al and B2, fcc, B2 and σ for medium amounts of Al and B2 plus σ for higher amounts of Al have been stabilized. However, in the calculated phase diagram (Figure 5 (b)), fcc and σ only stabilized at higher temperatures. Due to the mentioned sluggish diffusions of the atoms in HEA, the microstructures of these alloys are sensitive to the empirical characterization details such as heating/cooling rates and x-ray diffraction (XRD) scan speed.

4. CONCLUSION

In this work, phase diagrams of different metallic alloy systems were calculated, studied and compared to experimental as well as thermodynamically calculated phase diagrams in previous studies. The results revealed the capabilities of the commercial software packages to accurately predict binary and ternary phase diagrams. However, for HEAs, the calculated results using Thermo-Calc did not resemble the experimental phase diagrams. On the other hand, the integrated multicomponent CALPHAD method with AIMD showed more consistent results with respect to the experimentally determined phase diagrams.

ACKNOWLEDGMENTS

The authors would like to acknowledge the funding support provided by the University of Missouri Research Board to complete this work. The supercomputer time

allocation for completing the first principle calculations was provided by the Extreme Science and Engineering Discovery Environment (XSEDE): SDSC Comet cluster, award number TG-DMR140008.

REFERENCES

- [1] M.-H. Tsai, J.-W. Yeh, High-entropy alloys: a critical review, *Materials Research Letters* 2(3) (2014) 107-123.
- [2] D. Miracle, O. Senkov, A critical review of high entropy alloys and related concepts, *Acta Materialia* 122 (2017) 448-511.
- [3] F. Otto, Y. Yang, H. Bei, E.P. George, Relative effects of enthalpy and entropy on the phase stability of equiatomic high-entropy alloys, *Acta Materialia* 61(7) (2013) 2628-2638.
- [4] M.B. Kivvy, M.A. Zaeem, S. Lekakh, Investigating phase formations in cast AlFeCoNiCu high entropy alloys by combination of computational modeling and experiments, *Materials & Design* (2017).
- [5] M.-x. Ren, B.-s. Li, H.-z. Fu, Formation condition of solid solution type high-entropy alloy, *Transactions of Nonferrous Metals Society of China* 23(4) (2013) 991-995.
- [6] J.-W. Yeh, Alloy Design Strategies and Future Trends in High-Entropy Alloys, *JOM* 65(12) (2013) 1759-1771.
- [7] K.-Y. Tsai, M.-H. Tsai, J.-W. Yeh, Sluggish diffusion in Co–Cr–Fe–Mn–Ni high-entropy alloys, *Acta Materialia* 61(13) (2013) 4887-4897.
- [8] J.-C. Zhao, *Methods for phase diagram determination*, elsevier2011.
- [9] H. Nishiura, R.O. Suzuki, K. Ono, L.J. Gauckler, Experimental Phase Diagram in the Ag-Cu₂O-CuO System, *Journal of the American Ceramic Society* 81(8) (1998) 2181-2187.
- [10] D.R. Gaskell, *Introduction to the Thermodynamics of Materials*, CRC Press2008.
- [11] H.L. Lukas, S.G. Fries, B. Sundman, *Computational thermodynamics: the Calphad method*, Cambridge university press Cambridge2007.
- [12] C. Bale, E. BÉlisle, P. Chartrand, S. Decterov, G. Eriksson, K. Hack, I.-H. Jung, Y.-B. Kang, J. Melançon, A. Pelton, FactSage thermochemical software and databases—recent developments, *Calphad* 33(2) (2009) 295-311.

- [13] J.-O. Andersson, T. Helander, L. Höglund, P. Shi, B. Sundman, Thermo-Calc & DICTRA, computational tools for materials science, *Calphad* 26(2) (2002) 273-312.
- [14] U.R. Kattner, The thermodynamic modeling of multicomponent phase equilibria, *JOM* 49(12) (1997) 14-19.
- [15] J. Tomiska, Mathematical conversions of the thermodynamic excess functions represented by the Redlich-Kister expansion, and by the Chebyshev polynomial series to power series representations and vice-versa, *Calphad* 8(4) (1984) 283-294.
- [16] Z.-K. Liu, First-principles calculations and CALPHAD modeling of thermodynamics, *Journal of phase equilibria and diffusion* 30(5) (2009) 517.
- [17] N. Saunders, A.P. Miodownik, CALPHAD (calculation of phase diagrams): a comprehensive guide, Elsevier 1998.
- [18] J. Hafner, Ab-initio simulations of materials using VASP: Density-functional theory and beyond, *Journal of computational chemistry* 29(13) (2008) 2044-2078.
- [19] P.E. Blöchl, Projector augmented-wave method, *Physical Review B* 50(24) (1994) 17953.
- [20] G. Kresse, D. Joubert, From ultrasoft pseudopotentials to the projector augmented-wave method, *Physical Review B* 59(3) (1999) 1758.
- [21] J.P. Perdew, K. Burke, M. Ernzerhof, Generalized gradient approximation made simple, *Physical review letters* 77(18) (1996) 3865.
- [22] D.M. Ceperley, B. Alder, Ground state of the electron gas by a stochastic method, *Physical Review Letters* 45(7) (1980) 566.
- [23] H. Yu, D. Duan, H. Liu, T. Yang, F. Tian, K. Bao, D. Li, Z. Zhao, B. Liu, T. Cui, Ab initio molecular dynamic study of solid-state transitions of ammonium nitrate, *Scientific reports* 6 (2016).
- [24] G. Kresse, J. Hafner, Ab initio molecular dynamics for open-shell transition metals, *Physical Review B* 48(17) (1993) 13115.
- [25] F. Zhang, C. Zhang, S.-L. Chen, J. Zhu, W.-S. Cao, U.R. Kattner, An understanding of high entropy alloys from phase diagram calculations, *Calphad* 45 (2014) 1-10.
- [26] C. Allibert, C. Bernard, N. Valignat, M. Dombre, Co • Cr binary system: experimental re-determination of the phase diagram and comparison with the diagram calculated from the thermodynamic data, *Journal of the Less Common Metals* 59(2) (1978) 211-228.

- [27] L. Kaufman, H. Nesor, Calculation of superalloy phase diagrams: Part I, Metallurgical and Materials Transactions B 5(7) (1974) 1617-1621.
- [28] C.-Y. Hsu, C.-C. Juan, S.-T. Chen, T.-S. Sheu, J.-W. Yeh, S.-K. Chen, Phase Diagrams of High-Entropy Alloy System Al-Co-Cr-Fe-Mo-Ni, JOM 65(12) (2013) 1829-1839.
- [29] C. Gelatt Jr, A. Williams, V. Moruzzi, Theory of bonding of transition metals to nontransition metals, Physical Review B 27(4) (1983) 2005.

IV. INVESTIGATION OF INTERSTITIAL CARBON IMPACT IN MICROSTRUCTURES OF $\text{Al}_x\text{CoCrFeNiCu}$ ($x=0.3, 1.5, 2.8$) HIGH ENTROPY ALLOYS

M. Beyramali Kivy, C.S. Kriewall, M. Asle Zaeem *

Department of Materials Science and Engineering, Missouri University of Science and Technology, 1400 N. Bishop Ave, Rolla, MO 65409, USA

(This manuscript is under preparation for submission to *Metals* journal)

ABSTRACT

Effects of addition of 0.5 at.% interstitial carbon in $\text{Al}_x\text{CoCrFeNiCu}$ high entropy alloys are studied considering three various compositions ($x=0.3, 1.5, 2.8$). Despite of the higher solidification temperature of aluminum carbide compared to chromium carbides, the thermodynamic calculations show stability of Cr_7Cr_3 at the melting point and $\text{Cr}_{23}\text{Cr}_6$ at lower temperatures in the studied alloying system. The experimental characterizations of cast $\text{Al}_{0.3}\text{CoCrFeNiCu}$ and $\text{Al}_{2.8}\text{CoCrFeNiCu}$ HEAs reveal a main phase and a segregated phase containing both Cr and C. In cast $\text{Al}_{1.5}\text{CoCrFeNiCu}$, in addition to these two phases, a Cu-rich phase is also detected. Addition of carbon results in segregation of Cr from $\text{Al}_x\text{CoCrFeNiCu}$ high entropy alloys resulting in formation of chromium carbide phases.

Keywords: High Entropy Alloys; Interstitial carbon; Carbide,

1. INTRODUCTION

Multi-principal element (MPE) alloys also known as high entropy alloys (HEAs) can be designed to have promising properties [1, 2]. Most of the studied HEAs revealed simple microstructures consisting of random solid solutions [1]. Classic design of HEAs

is based on considering five or more substitutional alloying elements with near equi-atomic compositions [2]. However, It is known that changing the compositions of the alloys can dramatically alter their microstructures. For instance, it is shown that the addition of the amounts of aluminum in $Al_xCoCrFeNiCu$ HEAs changes the phases from single phase fcc to double phase fcc and bcc and then single phase bcc [3]. Since 2015 when Wu *et al.* [4] successfully studied the effect of interstitial carbon addition on mechanical properties improvement of equi-atomic FeNiCoCrMn HEA, a new strategy in MPE alloys design were introduced. Their results showed that addition of 0.5 at% carbon did not change the single fcc phase of the FeNiCoCrMn HEA [4]. However, addition of the interstitial carbon increased both yield strength and ultimate tensile strength [4]. Similar strength improvements were observed in the same HEA by doping 0.5 to 1 at% boron [5]. Later, Zhiming Li et al. studied the phases of FeMnCoCr MPE alloy with addition of 0.5 at% interstitial carbon using EDS [6]. Figure 1 [6] illustrates the current state of strength-ductility of the HEAs including these recent HEA designs containing interstitial elements. As shown in this figure, exceptional strength-ductility combination of interstitial HEAs.

In this project, we study the effect of interstitial carbon on the microstructures and properties of $Al_xFeCoCrNiCu$ HEAs. The experimental investigations showed that low amounts of Al in these HEAs stabilizes fcc phase while high concentrations of Al stabilizes bcc phase [7]. We will study possible segregation of elements and formation of different carbides.

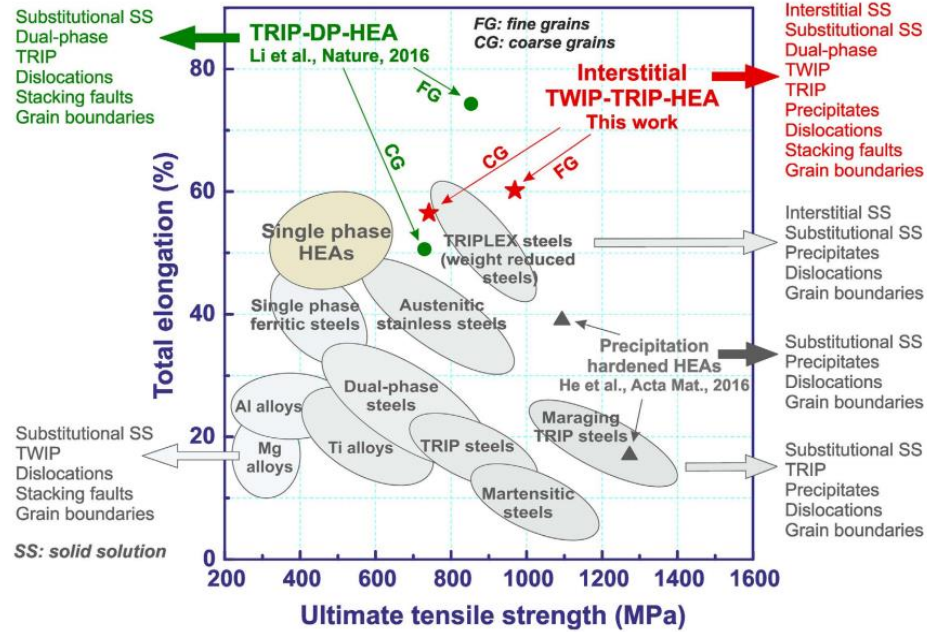


Figure 1. Strength-ductility profiles (at room temperature) for different metallic materials including HEAs. FG indicates fine grains and CG refers to coarse grains [6].

2. METHODOLOGY

Highly pure (> 99.9%) elemental powders (spherical gas atomized ~40 micron) were mixed and melted in graphite crucibles in an induction furnace under argon gas at atmospheric pressure. The samples were held at 1600 °C for one hour and then cooled down to the room temperature (~100 °C/min). The samples were cut and polished for characterization purposes. Scanning electron microscopy (SEM) (FEI Helios NanoLab 600 FIB/FESEM) was used for the phase analyses. Elemental compositions of the phases as well as atomic distributions were studied using Oxford Energy Dispersive Spectrometer (EDS). For the quantitative elemental analysis, both point EDS and EDS maps were done.

For thermodynamic modeling of phase diagrams, Thermo-Calc 2017 software with TCFE9: Steels/Fe-Alloys V9.0 and TCHEA2: High Entropy Alloys V2.0 databases was utilized to investigate the possible carbide formation for different compositions.

3. RESULTS AND DISCUSSION

Crystal structures and solidification temperatures of different possible carbides can be found in Table 1 [8, 9].

Table 1. Structures and solidification temperatures of aluminum and chromium carbides.

Carbide	Crystal Structure	Melting Temperature (°C)
Al_3C_4	Tetrahedral	2200
Cr_3C_2	Orthorhombic	1250
Cr_7C_3	Hexagonal	1665
Cr_{23}C_6	Cubic	1895

Figure 2 shows high temperature phase diagrams (above 1,000 °C) determined by Thermo-Calc. Various alloying elements were added to the Cr-Al-C ternary system and the carbide formations were studied. It should be noted that all the cases are equi-atomic without carbon. In the Cr-Al-C ternary system, formation of Al_3C_4 is evident. However, in all the other cases, despite the higher solidification temperature of Al_3C_4 compared to chromium carbides, the thermodynamic calculation results showed that chromium carbides will possibly form.

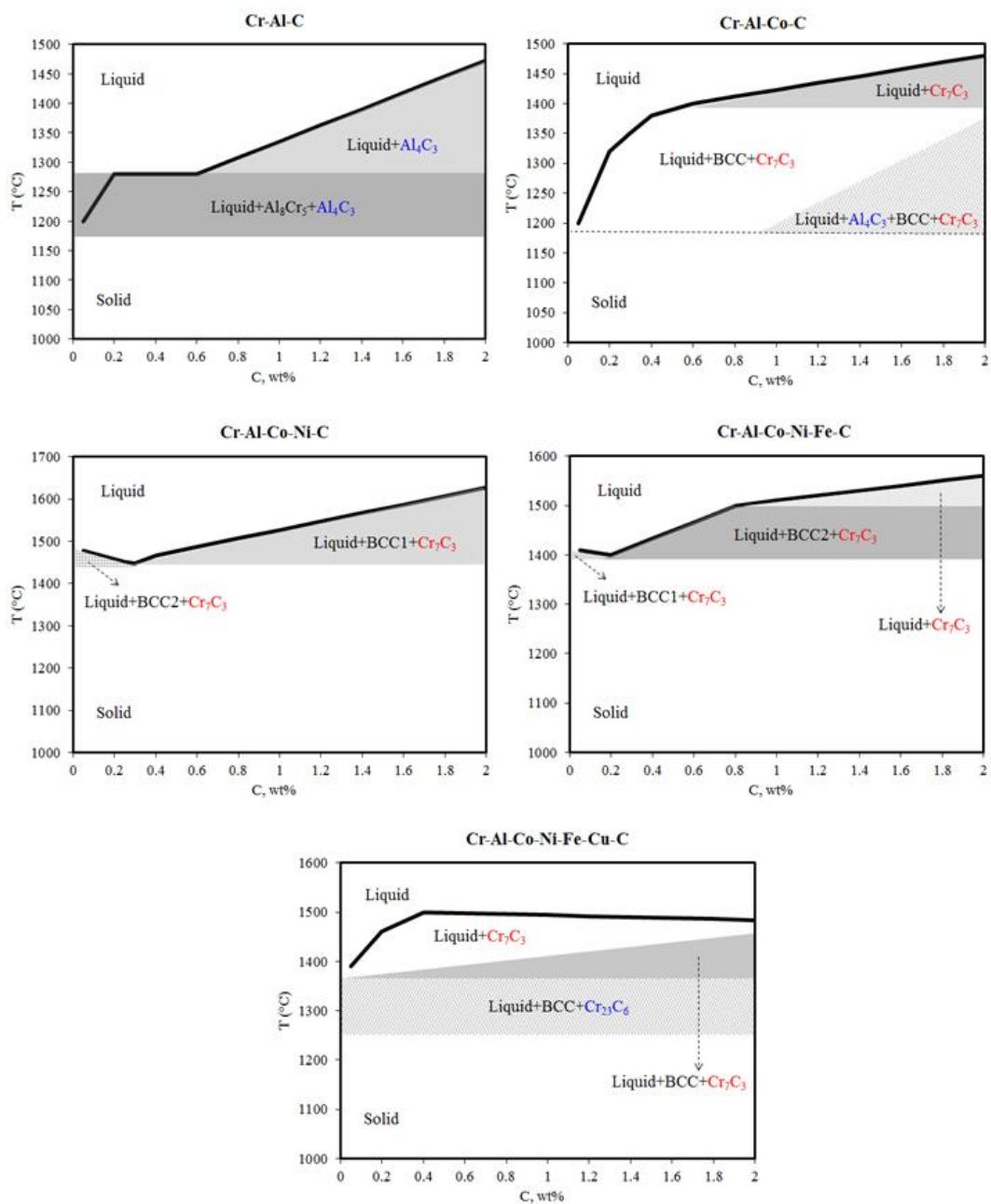


Figure 2. Calculated carbide formations considering addition of different alloying elements to Cr-Al from ternary to six elements HEA.

As it can be seen in most cases Cr_7C_3 is formed, but AlFeCoCrNiCu HEA system both Cr_7C_3 and Cr_{23}C_6 form, and most likely by lowering the temperature on cooling, Cr_{23}C_6 stabilizes.

The SEM-EDS results for the three studied HEAs are shown in Figure 3 to 5, and the quantitative elemental EDS analyses are provided in Table 2. A segregated Cr rich phase was observed in all three alloys. Since carbon and chromium were only observed in this phase, it could be concluded that chromium carbides were possibly formed instead of aluminum carbide. This is consistent with the phase diagram calculations presented in Figure 2. The second phase in $Al_{0.3}CoCrFeNiCu$ and $Al_{2.8}CoCrFeNiCu$ HEAs contained the rest of the alloying elements. This shows that the addition of the interstitial carbon changed the previously reported single phase microstructures for these HEAs [3]. Medium amount of Al in $Al_{1.5}CoCrFeNiCu$ was previously reported to stabilize a microstructure as a mixture of an fcc and a bcc phase [3]. The EDS results in this work showed these two phases, also a Cr-rich third phase which is believed to be $Cr_{23}C_6$.

More experimental characterization analyses including x-ray diffraction (XRD) and electron back-scattered diffraction (EBSD) are being conducted to accurately determine the phases and structures in the studied HEAs in this work.

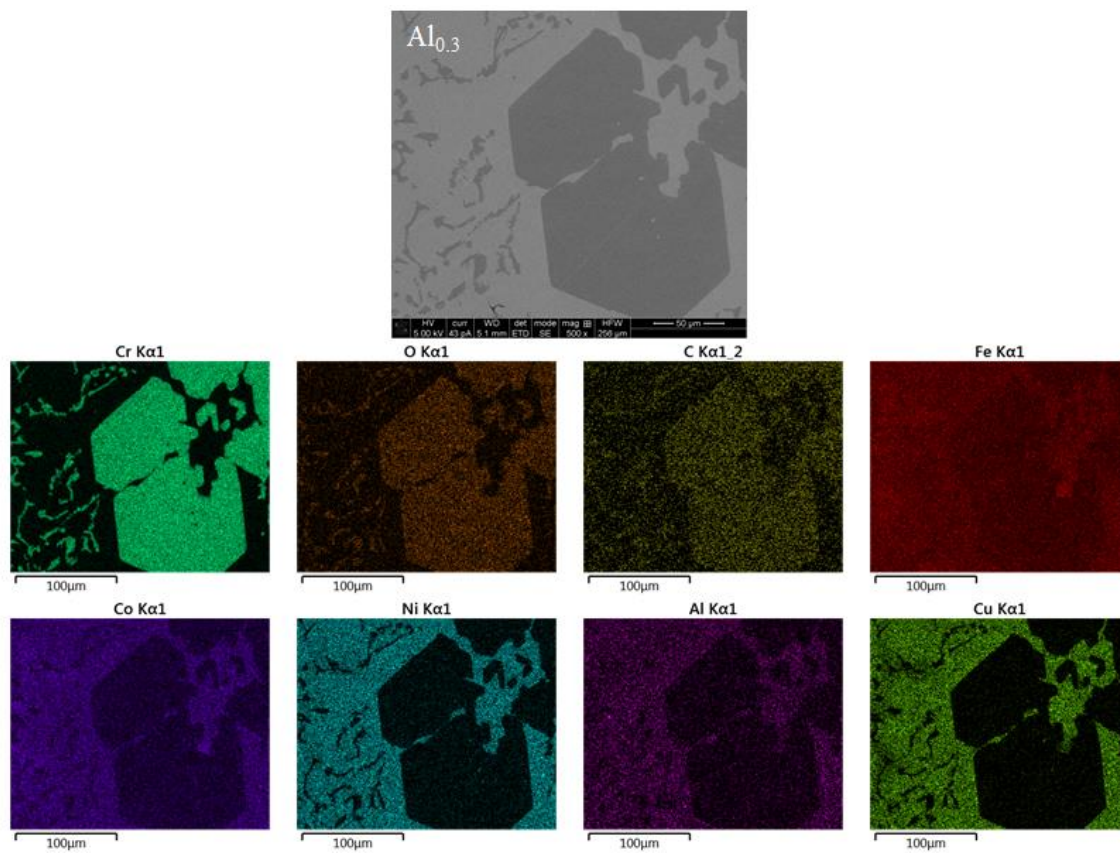


Figure 3. EDS elemental map of $\text{Al}_{0.3}\text{CoCrFeNiCu}$

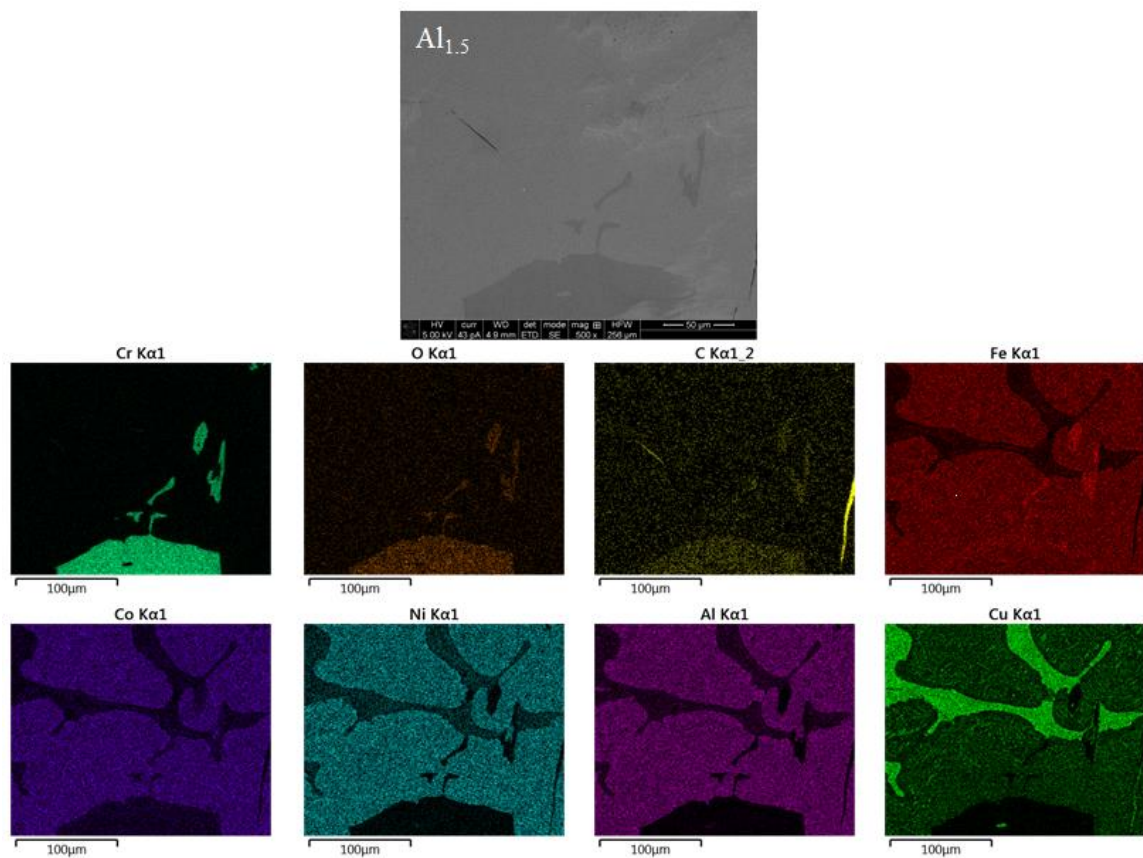


Figure 4. EDS elemental map of $Al_{1.5}CoCrFeNiCu$

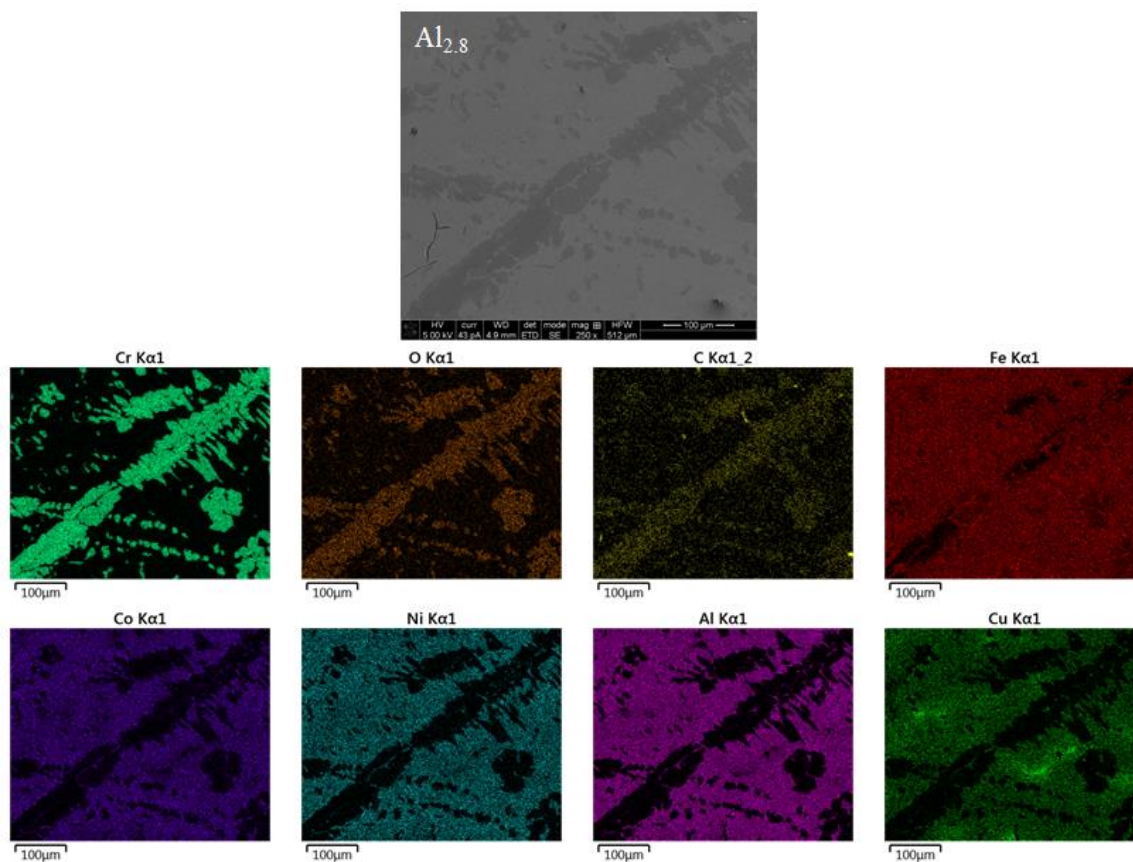


Figure 5. EDS elemental map of $Al_{2.8}CoCrFeNiCu$

Table 2. Quantitative elemental EDS analysis.

Alloy	Phase	Al	Co	Cr	Fe	Ni	Cu	C	O
Al _{0.3}	1	0.00	13	61.02	20.16	3.28	0.00	2.54	0.00
	2	1.29	22.5	2.64	20.63	27.73	24.35	0.66	0.21
Al _{2.8}	1	0.23	3.45	80.37	12.25	0.42	0.30	3.67	0.00
	2	13.10	14.69	0.54	14.12	0.21	41.38	0.71	0.12
Al _{1.5}	1	0.03	8.28	69.04	18.70	1.10	0.00	2.47	0.28
	2	7.71	20.67	0.56	14.09	23.80	32.31	0.68	0.19
	3	2.86	5.87	0.26	5.06	9.81	74.74	0.71	0.16

REFERENCES

- [1] M.B. Kivy, M.A. Zaeem, Generalized stacking fault energies, ductilities, and twinnabilities of CoCrFeNi-based face-centered cubic high entropy alloys, *Scripta Materialia* 139 (2017) 83-86.
- [2] D. Miracle, O. Senkov, A critical review of high entropy alloys and related concepts, *Acta Materialia* 122 (2017) 448-511.
- [3] J.W. Yeh, S.K. Chen, S.J. Lin, J.Y. Gan, T.S. Chin, T.T. Shun, C.H. Tsau, S.Y. Chang, Nanostructured high-entropy alloys with multiple principal elements: novel alloy design concepts and outcomes, *Advanced Engineering Materials* 6(5) (2004) 299-303.
- [4] Z. Wu, C. Parish, H. Bei, Nano-twin mediated plasticity in carbon-containing FeNiCoCrMn high entropy alloys, *Journal of Alloys and Compounds* 647 (2015) 815-822.
- [5] Z. Wang, I. Baker, Interstitial strengthening of a fcc FeNiMnAlCr high entropy alloy, *Materials Letters* 180 (2016) 153-156.

- [6] Z. Li, C.C. Tasan, H. Springer, B. Gault, D. Raabe, Interstitial atoms enable joint twinning and transformation induced plasticity in strong and ductile high-entropy alloys, *Scientific reports* 7 (2017) 40704.
- [7] X. Yang, Y. Zhang, Prediction of high-entropy stabilized solid-solution in multi-component alloys, *Materials Chemistry and Physics* 132(2) (2012) 233-238.
- [8] R. Chattopadhyay, *Surface wear: analysis, treatment, and prevention*: ASM international, (2001).
- [9] V. L. Solozhenko and O. O. Kurakevych, "Equation of state of aluminum carbide Al₄C₃," *Solid state communications*, vol. 133, (2005) 385-388.

SECTION

3. SUMMARY, CONCLUSION, AND RECOMMENDATIONS FOR FUTURE WORK

This Ph.D. research project aimed at integrating computational modeling tools and experiments to study and provide a better understanding of phase formations and deformation mechanism of selected high entropy alloys (HEAs). To study phase formations and phase diagrams of some HEAs, a thermodynamic model was developed and a code was written in Matlab based on: 1) sublattice CALPHAD method combined with Muggianu's methods, separately and 2) solution model CALPHAD (without sublattice) combined with Muggianu's and first principle methods. The calculated phase diagrams of the selected HEAs were more consistent with the experimental results compared with the commercial software, such as Thermo-Calc, FactSage, and Pandat. The presented model for calculating the phase diagrams of multi component alloys can be extended to predict the crystal structures and phases of other alloys and can be used to study and design new material systems.

To investigate the deformation mechanisms and ductilities of CoCrFeNi-based fcc HEA, generalized stacking fault energies (GSFE) were also determined utilizing density functional theory (DFT) calculations. It was shown that addition of Mn, Cu, or high amounts of Al aided dislocation gliding and martensitic transformations, while addition of Ti or Mo promoted dislocation gliding and mechanical twinning. Addition of Mn and/or Cu enhanced the ductility of the studied HEAs, while Al, Ti, or Mo decreased it promoting crack cleavage. A similar explicit DFT approach was also used to study the GSFE and the phase transformations of the dual stage transformation induced plasticity

(TRIP) advanced high strength steels (AHSS), Fe-Mn-Si-Al-C. Mn and Si were shown to decrease the stacking fault energy promoting the martensitic phase transformations, while Al and interstitial C increased the GSFE stabilizing the γ -austenite phase.

Since the addition of interstitial carbon to other alloy systems, such as steel, can improve the mechanical properties, it was added to the $\text{Al}_x\text{FeCoCrNiCu}$ ($x=0.3, 1.5, 2.8$) HEAs to study the role of interstitial elements on phase formations in these alloys. The results showed that the addition of interstitial C promoted segregation of a Cr-rich phase which possibly could be a chromium carbide phase in all of the studied alloys.

- Recommendations for future work
 - ❖ To increase the accuracy of the developed algorithm for calculating the phase diagrams of multicomponent alloy systems, high-throughput DFT calculations and high-throughput experimental data need to be generated to create more complete databases. Also more comprehensive uncertainty analyses need to be considered to evaluate the reliability of predications.
 - ❖ First principle approaches should be applied to study the effects of defects and vacancies on the GSFE and mechanical properties of the HEAs. Since in this study we only concentrated on determining the GSFE for a class of fcc HEAs, the GSFE, deformation mechanisms, and phase transformations of HEAs with other crystal structures such as body-centered cubic and hexagonal closed pack should be investigated. Also, ab initio molecular dynamic simulations should be used to determine crystal structures and properties at high temperatures.

- ❖ To explore possible applications of the HEAs, other properties of the HEAs such as electrical, thermal and magnetic properties should be studied by first principle calculations.
- ❖ To study properties and deformation and failure mechanisms at the nano-scale, the first principle and experimental data can be used to develop advanced semi-empirical inter-atomic potentials enabling large scale atomistic simulations of nano-poly crystalline HEAs.
- ❖ Since the addition of interstitial elements to alloy systems may improve their properties, the effects of different interstitial elements on the microstructures and properties of various HEA systems can be studied.

APPENDIX A.

EFFECT OF ALLOYING ELEMENTS ON TWO-STAGE PHASE
TRANSFORMATION IN Fe-Mn-Si-Al-C ADVANCED HIGH STRENGTH STEEL

**EFFECT OF ALLOYING ELEMENTS ON TWO-STAGE PHASE
TRANSFORMATION IN Fe-Mn-Si-Al-C ADVANCED HIGH STRENGTH
STEEL**

M. Beyramali Kivy and M. Asle Zaeem*

Department of Materials Science and Engineering, Missouri University of Science and
Technology, 1400 N. Bishop Ave, Rolla, MO 65409, USA

(This manuscript is under preparation for submission to *Physica B. Condensed mater*)

ABSTRACT

Effects of unary, binary and ternary combinations of alloying elements on the unstable and intrinsic stacking fault energies (USFE and ISFE) and phase transformations in Fe-Mn-Si-Al-C were studied using density functional theory calculations. Driving forces for transformation of retained fcc- γ -austenite to hcp- ϵ -martensite and later to bcc- α' -martensite were calculated. The results showed that addition of Mn and/or Si elements on the stacking fault planes reduced the ISFE and decreased the hcp to fcc transformation energy promoting the formation of local ϵ -martensite structure. On the other hand, addition of Al and/or C elements on the stacking fault plane of both pure austenite Fe and Fe₈₇Mn₁₄Si₅Al₂C₁ matrices increased the ISFE and USFE which resulted in stabilizing the retained γ -austenite phase. The transformation from ϵ -martensite to α' -martensite was prompted by increasing the amount of Si/Al or using a medium amount of Mn (~14 at.%), while formation of α' -martensite phase was limited when a low (<10 at.%) or a high amount of Mn (>18 at.%) was used.

Keywords: Generalized stacking fault energy; Phase transformation; Density functional theory calculations; high strength steel.

1. INTRODUCTION

Advanced high strength steels (AHSS) or high manganese steels are multiphase and microstructurally complex steels. AHSS have specifically designated chemistries and go through different strengthening mechanisms such as explicit cooling and heating processes [1]. The improved properties of these steels compared to the conventional steels such as their high strength, ductility, and strain hardening rate, make them suitable in wide varieties of applications especially in the automobile manufacturing industries [2]. The strengthening mechanisms of these steels include solid-solution strengthening with medium amount of manganese, precipitation strengthening, grain refinement, and a two-stage phase transformation from fcc- γ -austenite to hcp- ϵ -martensite and later to bcc- α' -martensite [1].

In AHSS since the austenite phase has the highest uniform strain to failure while martensite phase has the highest strength among all the phases, appropriate austenite-martensite mixtures could produce ideal combinations of strength and formability behavior [2, 3]. The transformation induced plasticity (TRIP) behavior caused by γ -austenite transformation to ϵ -martensite is controlled by the unstable and intrinsic stacking fault energies (USFE and ISFE) [4, 5]. Stacking faults are two-dimensional defects that can be generated in materials by mechanical deformations [6]. The generalized stacking fault energy (GSFE) of a material is the total energy per unit area to create a complete stacking fault. The maximum point in a GSFE curve is the USFE which is the least compulsory energy for nucleation of dislocations, and the minimum energy is the ISFE formed by removing one sequence from perfect fcc crystal stacking sequence

[7]. Therefore, calculating both USFE and ISFE is necessary to accurately predict the deformation behavior of materials [8, 9].

Unlike ISFE, the USFE cannot be determined by experiments and can be only calculated theoretically using first principle or atomistic methods such as density functional theory (DFT) and molecular dynamics (MD) simulations [4, 10, 11]. To determine GSFE of materials using DFT calculations, explicit and implicit approaches can be applied. First principle explicit method determines the total energy difference between the perfect and faulted crystals and provides good information about electronic structure variations at the stacking fault [4, 12, 13]. On the other hand, implicit method calculates the energies of the fcc, hcp and double hcp to define the SFE of the fcc structures and offers a homogeneous description of the bulk environment [14, 15]. Both explicit and implicit approaches were employed previously to calculate the ISFE of Fe-X binary systems (X=Ti, V, Cr, Mn, Co, Ni, Cu, Zr, Nb, Mo, Tc, Ru, Rh, Pd, Ag and C) [4, 15, 16]. Also, GSFE of Fe-X binary systems (X=Mn, Al, C and Ni) were computed using first principle approach [13, 17]. However, in most of these works only one atom of each of the alloying elements were considered. Thermodynamic methods were also used to study the effects of alloying elements on ISFE in steels [5, 11, 18], but these methods cannot calculate USFE.

In this work, DFT calculations were employed to study the effects of the alloying elements and their amounts on USFE, ISFE, and the dual-stage transformation in Fe-Mn-Si-Al-C system.

2. METHODOLOGY

In this work, Vienna ab initio simulation package (VASP) [19] was used to perform the DFT simulations. Instead of ultra-soft pseudopotentials, projector augmented wave (PAW) potentials [20, 21] and the generalized gradient approximation (GGA) [22, 23] were used to enhance the accuracy of the calculations. All the structures were relaxed until the ionic optimization convergence was within 0.01 eV/atom. The supercell structures used in this work are presented in Figure 1. The fcc supercell considered for the stacking fault energy calculations consisted of 108 atoms in total with 9 planes along $[111]$ axis and 12 atoms on each plane considering $a=3.57\text{\AA}$ (Figure 1 (a)) [24].

To avoid the saturation of the stacking fault plane with alloying elements, less than 25% of the Fe atoms on the stacking fault plane were substituted by the substitutional alloying elements. The interstitial carbon atoms were added to each structure and then the structure was relaxed. The stacking faults were formed in the perfect fcc structures by a rigid displacement of the atoms above the stacking fault plane along $[\bar{2}11]$ direction in the (111) slip plane [25-27]. This resulted in a $b_p=1/6\langle 211 \rangle_{\{111\}}$ partial Burgers vector (a Shockley partial dislocation) [4, 5, 10, 28] (Figure 1 (c)). Two $b_p=1/6\langle 211 \rangle_{\{111\}}$ Shockley partial dislocations form a $a/2\langle 110 \rangle$ perfect dislocation. An unstable stacking fault (USF) forms due to the shear displacement through half of that Burgers vector, $\gamma_{USF}=1/12\langle 211 \rangle_{\{111\}}$ [17] (Figure 1 (b)). The stacking fault energies (USFE and ISFE) were calculated by applying the ab initio explicit approach for non-magnetic state as the total formation energy difference between defect-free perfect lattice and faulted lattice per unit area:

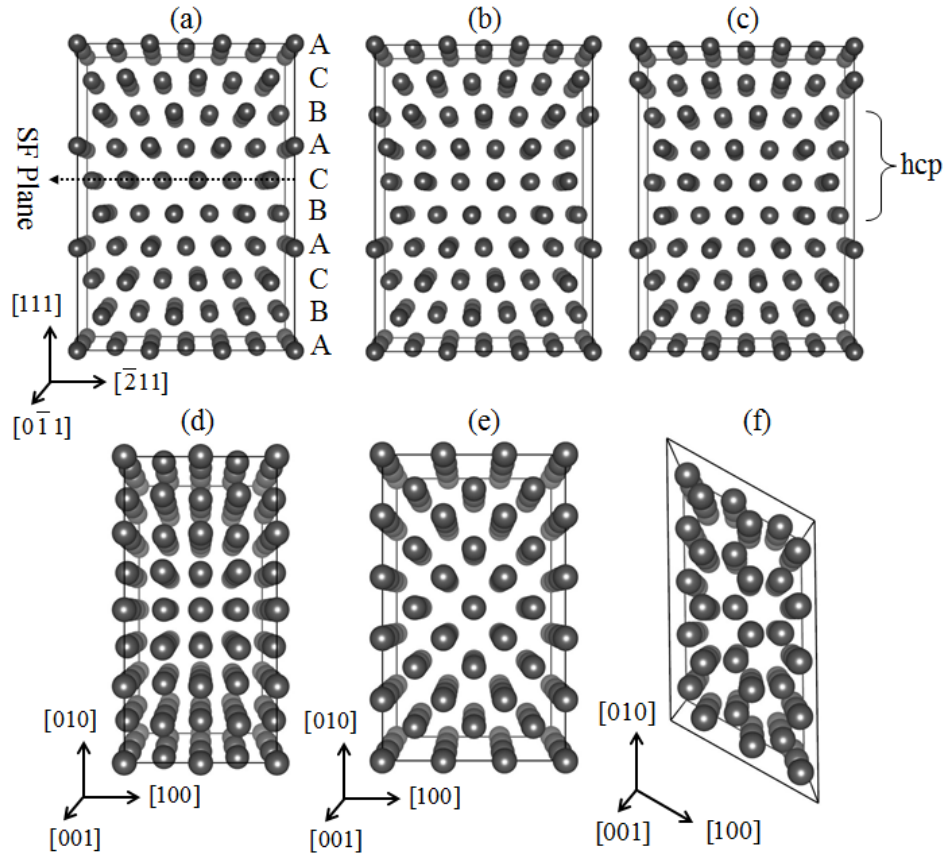


Figure B.1. (a) Perfect fcc structure, (b) unstable stacking fault, and (c) intrinsic stacking fault used for GSFE calculations. (d) fcc, (e) bcc, and (f) hcp structures used for phase transformation calculations.

$$SFE \text{ (mJ / m}^2\text{)} = \frac{E_0 - E_f}{A} \quad (1)$$

where E_0 (mJ) is the formation energy of the perfect undistorted lattice, E_f (mJ) is the total formation energy of the sheared lattice and A (m²) is the area perpendicular to the stacking faults [10, 27, 29].

This work was focused on the investigation of GSFE of an AHSS when altering the composition of the stacking fault plane. Fe₈₄Mn₁₃Si_{2.1}Al_{0.8}C_{0.1} AHSS was considered and to construct the initial structure of the FCC supercell, the elements were distributed

randomly throughout the supercell and a few relaxation steps were taken to find the most stable structures.

In previous works to study the effect of alloying elements on GSFE of Fe, usually one atom of the alloying element is placed on the stacking fault plane of a pure FCC Fe matrix. The results in the literature shows a linear reduction of ISFE as the alloying atom is moved away from the stacking fault plane [13, 16]. This provides some fundamental understanding of effect of single alloying elements on GSFE of pure FE, however in the case of steels where several alloying elements are present in the matrix, the combined effects of different elements should be considered. In this work we want to resemble the actual composition of an AHSS where the alloying elements are distributed throughout the whole matrix. In this case, selecting the position of the stacking fault plane may affect the GSFE calculations as different stacking fault plans and their neighboring plans have different compositions. Therefore, we use three different planes of the supercell (Figure 1 (a)) as stacking fault planes to calculate the corresponding USFE and ISFE for each. The average deviation of the calculated energies were determined and presented as the uncertainty bars in Figure 2.

In order to study the elemental effects on the phase transformations, fcc supercell with 100 atoms and lattice constant of $a=3.57\text{\AA}$ [24] (Figure 1 (d)), bcc supercell with 96 atoms and lattice constant of $a=3.86\text{\AA}$ [30] (Figure 1 (f)) and hcp supercell with 96 atoms and lattice constants of $a=b=3.47\text{\AA}$ and $c=3.96\text{\AA}$ [31] (Figure 1 (e)) were considered and ΔE of different structures with the same compositions were calculated.

3. RESULTS AND DISCUSSION

3.1. STACKING FAULT ENERGIES

USFE and ISFE of both pure austenite Fe and $\text{Fe}_{87}\text{Mn}_{14}\text{Si}_5\text{Al}_2\text{C}_1$ systems were calculated considering different alloying elements on their stacking fault planes with various compositions. To present the result in a more distinguishable way, the USFE and ISFE results are presented separately in Figure 2 (a) and (b) respectively for all the studied cases. The USFE and ISFE of nonmagnetic pure fcc-austenite Fe were calculated to be $500 \pm 25 \text{ mJ/m}^2$ and $-410 \pm 20 \text{ mJ/m}^2$, respectively. These values were in agreement with published results in the literature [4, 10, 12, 17]. As it can be seen, the reported energy values in Figure 2 are with respect to pure austenite Fe energy values. To investigate the effects of different alloying elements on the USFE and ISFE of Fe-Mn-Si-Al-C system, different perfect fcc structures with various atomic positions were relaxed and the structure with the minimum formation energy were selected. Three different planes of the selected fcc structure were chosen as the stacking fault planes and both USFE and ISFE (35 mJ/m^2 and 9 mJ/m^2 respectively) were calculated. The average deviation of the calculated energy values were presented in Figure 2 as average energy (dashed lines).

3.2. EFFECT OF SINGLE ELEMENT ON USFE AND ISFE

As shown in Figure 2(b), addition of Mn and/or Si on the stacking fault plane of austenite Fe decreased the ISFE. In the case of $\text{Fe}_{87}\text{Mn}_{14}\text{Si}_5\text{Al}_2\text{C}_1$, regardless of which plane is chosen as the stacking fault plane, the calculated ISFE values were higher than that of the pure Fe. Addition of Mn and/or Si slightly reduced the ISFE of $\text{Fe}_{87}\text{Mn}_{14}\text{Si}_5\text{Al}_2\text{C}_1$ with respect to the average energy value.

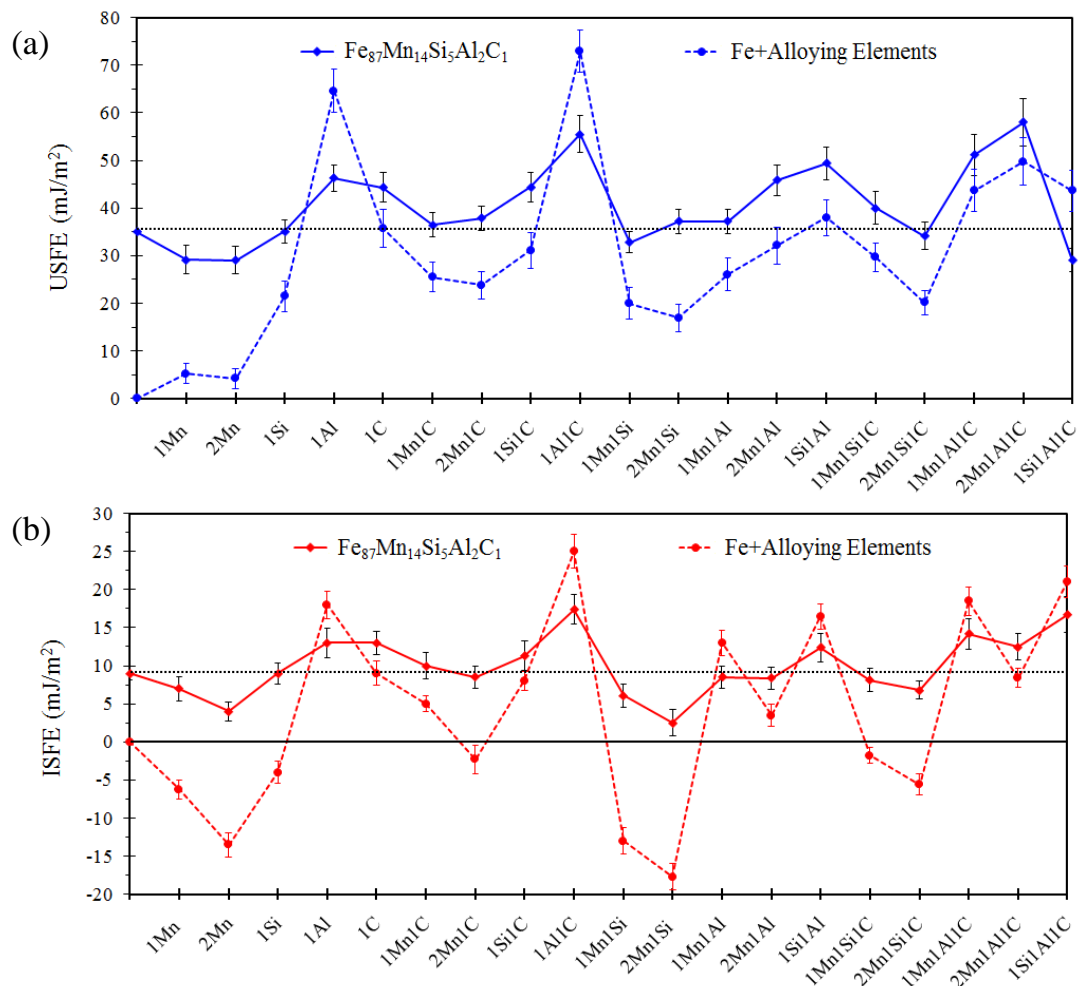


Figure B.2. (a) The calculated USFE, and (b) ISFE with respect to pure austenite Fe versus different alloying elements at the stacking fault plane. The solid lines at zero mJ/m² show relative energies of pure fcc iron and dashed lines show the average USFE and ISFE of Fe₈₇Mn₁₄Si₅Al₂C₁ considering three different stacking fault planes of relaxed structure.

It has been reported in some previous articles that increasing of Mn has parabolic effect on the ISFE where the ISFE initially decreases up to around 15-20 wt% (or ~13 at%) of Mn and then increases [13, 18, 32-34]. Also, it is suggested in the literature that the effect of Mn on the ISFE can be explained by thermochemical free energy difference between fcc- γ -austenite and hcp- ϵ -martensite [18, 35]. Calculated results in this work

also revealed that Mn had higher effect on ISFE compared to Si. On the other hand, the addition of Mn and/or Si in both austenite Fe and $\text{Fe}_{87}\text{Mn}_{14}\text{Si}_5\text{Al}_2\text{C}_1$ matrices increased the USFE compared to pure austenite iron. However, Mn and/or Si decreased the USFE with respect to the average ISFE of $\text{Fe}_{87}\text{Mn}_{14}\text{Si}_5\text{Al}_2\text{C}_1$. In the contrary, the addition of Al and/or interstitial C to both of the matrices, increased the USFE and ISFE, but it is worthy to note that in the matrix consisting all the alloying elements, the effects of Al and/or C were less intense than in austenite Fe matrix. These results are in agreement with the results reported in the literature [5]. However, according to some articles [36], ISFE of steels are relatively unresponsive to the small concentrations of carbon but in this work, due to the computational limitations, ~ 0.93 at% of C was considered which is relatively high compared to the experimental concentration.

3.3. EFFECT OF BINARY AND TERNARY ELEMENTS

In addition to the single elements, the effects of selected combinations of binary and ternary elements on the GSFE were studied. As illustrated in Figure 2, ISFE behavior can be qualitatively explain based on the effects of the elements individually. For instance, the addition of Al and interstitial C to the austenite Fe matrix increased the ISFE to 25 mJ/m^2 with respect to pure austenite Fe. This energy is higher than the calculated energies considering either only Al or only interstitial C. Placing Al and interstitial C atoms on the stacking fault plane of $\text{Fe}_{87}\text{Mn}_{14}\text{Si}_5\text{Al}_2\text{C}_1$ system increased the ISFE to 17.4 mJ/m^2 with respect to pure austenite Fe. To further investigate the effect of Mn as a primary alloying element in these types of TRIP-AHSS along with other alloying elements on the GSFE, different binary and ternary combinations were considered. It is shown in Figure 2 that generally increasing the amount of Mn on the stacking fault planes

of both matrices from 1 atom to 2 atoms decreased the calculated ISFE. This was regardless of other alloying elements on the stacking fault planes. Addition Mn and Si to austenite Fe matrix reduced the ISFE with respect to pure austenite Fe. Also, addition of Mn, Si and interstitial C to the same matrix decreased the ISFE of pure austenite Fe. Calculated ISFE by addition of Mn and Al and/or C to the austenite Fe showed higher ISFE compared to pure austenite Fe. As presented in Figure 2, $\text{Fe}_{87}\text{Mn}_{14}\text{Si}_5\text{Al}_2\text{C}_1$ matrix showed similar ISFE trends with respect to the alloying elements however, the sensitivity of ISFE behavior in $\text{Fe}_{87}\text{Mn}_{14}\text{Si}_5\text{Al}_2\text{C}_1$ matrix to the stacking fault plane composition was relatively lower than that in austenite Fe matrix. This suggested that neglecting the influences of the elements that are not isolated on the stacking fault plane is not recommended. Once again, these results are in agreement with the results published in the literature [11, 37, 38], however it is shown that increasing Mn in austenite steels has parabolic effect on the ISFE with the minimum at different concentrations of Mn depending upon the other alloying elements [18]. This behavior will be discussed later in this work by calculating the driving force of phase transformation. Furthermore, the effects of Si, Al and interstitial C were studied in this work as well considering different combinations of them. The results showed that the addition of 1Si-1C and 1Si-1Al on the stacking fault plane decreased the ISFE more than addition of 1Si-1Al-1C did for both austenite iron and $\text{Fe}_{87}\text{Mn}_{14}\text{Si}_5\text{Al}_2\text{C}_1$ systems. Finally, the effects of binary/ternary combinations of the alloying elements on the USFE behavior of austenite iron as well as $\text{Fe}_{87}\text{Mn}_{14}\text{Si}_5\text{Al}_2\text{C}_1$ system were computed and presented in Figure 2. The results revealed that the addition of any of the alloying elements to the pure austenite Fe increased the USFE. Addition of Mn concentration from one atom to two atoms on the stacking fault

plane decreased the USFE of austenite Fe matrix for Mn, Mn-C, Mn-Si, and Mn-Si-combinations. On the contrary, the USFE in Mn-Al and Mn-Al-C increased by increasing the Mn concentration on the stacking fault. Furthermore, the results showed that addition of Al and/or C to both matrices intensely increased the USFE. Considering 1Si-1C and 1Si-1Al on the stacking fault planes of both matrices had similar calculated USFE values.

Similar to the ISFE, the calculated USFE for $\text{Fe}_{87}\text{Mn}_{14}\text{Si}_5\text{Al}_2\text{C}_1$ system were less sensitive to the stacking fault plane composition compared to the austenite Fe system. According to the GSFE results, it can be concluded that the addition of Mn and/or Si aids the martensitic transformation by decreasing the ISFE and addition of Al and/or interstitial C stabilizes the γ -austenite phase. The calculated uncertainty values showed that considering same stacking fault plane compositions with different neighboring plane compositions also affected both calculated USFE and ISFE. Therefore, not only presence of the alloying elements in these steels will change the GSFE behavior, the position of these elements also with respect to the stacking fault planes will affect the GSFE behavior.

3.4. ELEMENTAL EFFECTS ON DUAL-STAGE TRANSFORMATION BEHAVIOR

To analyze the driving forces for the fcc γ -austenite to hcp ϵ -martensite and hcp ϵ -martensite to bcc α' -martensite, the formation energy difference between these three structures were calculated. The results are presented in Figure 3. To study the effect of alloying elements on two-stage phase transformations, two types of supercell crystal matrices were considered.

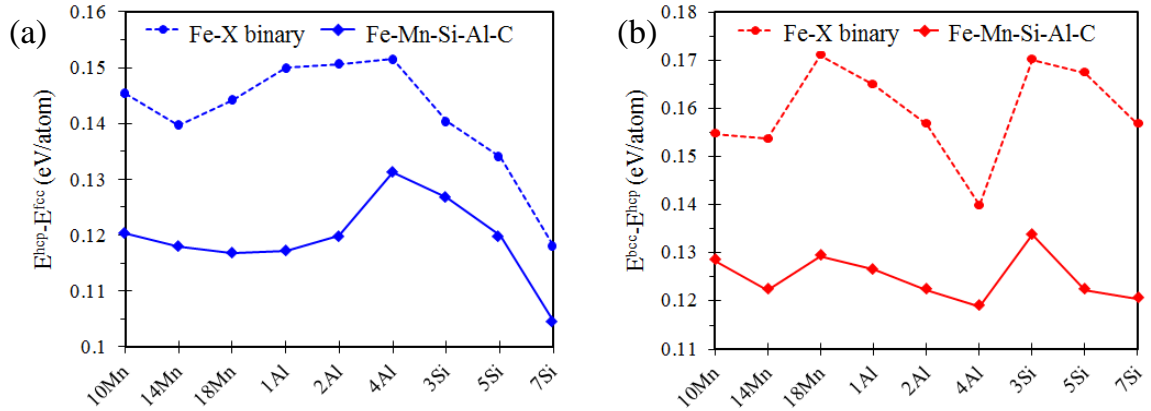


Figure B.3. Calculated Energy Difference between (a) fcc and hcp structures and (b) hcp and bcc structures.

In the first case, some of the Fe atoms in a pure iron matrix were replaced with particular concentrations of one alloying element (Fe-X binary in Figure 3) and in the other case, a matrix consisting Fe, Mn, Al and interstitial C was considered (Fe-Mn-Si-Al-C in Figure 3).

The illustrated results in Figure 3 showed that the addition of Si (3 at%, 5 at% and 7 at%) decreased the hcp-fcc transformation energy sustaining the formation of ϵ -martensite. Moreover, the addition of Si stabilized the formation of α' -martensite by decreasing the bcc-hcp transformation energy as well. Thus, it can be concluded that the addition of Si aids the completion of the dual-stage transformation (fcc \rightarrow hcp \rightarrow bcc). In both considered supercells, the effect of the addition of Si had relatively the same trend but higher ΔE values for Fe-Si binaries. Furthermore, as presented in Figure 3, the addition of Al increased the hcp-fcc transformation energy restraining the formation of ϵ -martensite phase. However, the addition of Al decreased the bcc-hcp transformation energy allowing the formation of α' -martensite phase. This means the formation of ϵ -

martensite decreases by increasing the Al but the possibly formed ϵ -martensite crystals tend to transform into α' -martensite phase in both the pure iron matrix as well as the matrix consisting Fe, Mn, Si, Al and interstitial C. These Si and Al elemental effects explained the ISFE behavior presented in Figure 3. The addition of Mn had a parabolic-like effect on the phase transformation behavior. This means the addition of Mn from 10 at% to 14 at% (medium-Mn) decreased the fcc \rightarrow hcp \rightarrow bcc transformation energies sustaining the formation of α' -martensite phase. Nonetheless, at higher amounts of Mn (18 at%), the fcc \rightarrow hcp and hcp \rightarrow bcc transformation energies increased. This phenomenon showed that the medium amounts of Mn aided the dual-stage transformation (fcc \rightarrow hcp \rightarrow bcc) more compared to lower and higher amounts of Mn. These results are in agreement with the literature [39-41].

4. CONCLUSION

In this work, ab initio calculation approach was used to study the deformation mechanisms of $\text{Fe}_{87}\text{Mn}_{14}\text{Si}_5\text{Al}_2\text{C}_1$ TRIP-AHSS and effects of different alloying elements on the generalized stacking fault energies and two-stage phase transformations were calculated in fcc-Fe matrix as well as the fcc-matrices with $\text{Fe}_{87}\text{Mn}_{14}\text{Si}_5\text{Al}_2\text{C}_1$ compositions. The results can be summarized as below.

- Addition of Mn and/or Si on the stacking fault planes of fcc austenite Fe matrix or $\text{Fe}_{87}\text{Mn}_{14}\text{Si}_5\text{Al}_2\text{C}_1$ matrix decreased the relative ISFE compared to the pure austenite Fe or average ISFE of relaxed $\text{Fe}_{87}\text{Mn}_{14}\text{Si}_5\text{Al}_2\text{C}_1$ respectively. On the contrary, adding Al and/or interstitial C to the fcc austenite Fe matrix increased the ISFE compared to pure austenite Fe. In the fcc-matrices consisting of $\text{Fe}_{87}\text{Mn}_{14}\text{Si}_5\text{Al}_2\text{C}_1$, these elemental

effects followed the same trend, however the ISFE for all of these cases were higher than ISFE of pure austenite Fe.

- Addition of Mn, Al, Si and interstitial C with any combination increased the USFE compared to pure austenite Fe for both matrices. However, Al and/or C increased the calculated relative USFE more than Mn and/or Si.
- Generally, the calculated GSFE of $\text{Fe}_{87}\text{Mn}_{14}\text{Si}_5\text{Al}_2\text{C}_1$ matrix were less sensitive to changing the stacking fault plane compositions compared to austenite Fe matrix.
- Addition of Si decreased the hcp-fcc and bcc-hcp transformation energies allowing the dual-stage phase transformation (fcc→hcp→bcc). Addition of Al on the other hand restrained the hcp formation but aided the hcp→bcc transformation. Although addition of Mn decreased the hcp-fcc and bcc-hcp transformation energies assisting the formation of hcp and bcc structures, higher amounts of Mn (17 at% in this work) restrained the martensitic transformation by increasing the bcc-hcp transformation energy.

ACKNOWLEDGMENTS

The authors are grateful for the computer time allocation provided by the Extreme Science and Engineering Discovery Environment (XSEDE).

REFERENCES

- [1] R. Kuziak, R. Kawalla, S. Waengler. Advanced high strength steels for automotive industry, Archives of civil and mechanical engineering 8 (2008) 103-117.
- [2] D.K. Matlock, J.G. Speer, E. De Moor, P.J. Gibbs. Recent developments in advanced high strength sheet steels for automotive applications: an overview, Jestech 15 (2012) 1-12.

- [3] R.H. Wagoner, G.R. Smith. Advanced High Strength Steel Workshop, Arlington, Virginia, USA (2006) 1-122.
- [4] K. Limmer, J. Medvedeva, D. Van Aken, N. Medvedeva. Ab initio simulation of alloying effect on stacking fault energy in fcc Fe, *Computational Materials Science* 99 (2015) 253-255.
- [5] A. Das. Revisiting stacking fault energy of steels, *Metallurgical and Materials Transactions A* 47 (2016) 748-768.
- [6] W.D. Callister, D.G. Rethwisch. *Materials science and engineering: an introduction*, Wiley New York, 2007.
- [7] C. Wang, H. Wang, T. Huang, X. Xue, F. Qiu, Q. Jiang. Generalized-stacking-fault energy and twin-boundary energy of hexagonal close-packed Au: A first-principles calculation, *Scientific reports* 5 (2015).
- [8] A. Hunter, I. Beyerlein, T. Germann, M. Koslowski. Influence of the stacking fault energy surface on partial dislocations in fcc metals with a three-dimensional phase field dislocations dynamics model, *Physical Review B* 84 (2011) 144108.
- [9] H. Van Swygenhoven, P. Derlet, A. Frøseth. Stacking fault energies and slip in nanocrystalline metals, *Nature materials* 3 (2004) 399-403.
- [10] E. Asadi, M.A. Zaeem, A. Moitra, M.A. Tschopp. Effect of vacancy defects on generalized stacking fault energy of fcc metals, *Journal of Physics: Condensed Matter* 26 (2014) 115404.
- [11] R. Xiong, H. Peng, H. Si, W. Zhang, Y. Wen. Thermodynamic calculation of stacking fault energy of the Fe–Mn–Si–C high manganese steels, *Materials Science and Engineering: A* 598 (2014) 376-386.
- [12] T. Hickel, A. Dick, B. Grabowski, F. Körmann, J. Neugebauer. Steel Design from Fully Parameter-Free Ab Initio Computer Simulations, *steel research international* 80 (2009) 4-8.
- [13] N. Medvedeva, M. Park, D.C. Van Aken, J.E. Medvedeva. First-principles study of Mn, Al and C distribution and their effect on stacking fault energies in fcc Fe, *Journal of Alloys and Compounds* 582 (2014) 475-482.
- [14] P. Denteneer, W. van Haeringen. Stacking-fault energies in semiconductors from first-principles calculations, *Journal of Physics C: Solid State Physics* 20 (1987) L883.
- [15] A. Reyes-Huamantínco, P. Puschnig, C. Ambrosch-Draxl, O.E. Peil, A.V. Ruban. Stacking-fault energy and anti-Invar effect in Fe-Mn alloy from first principles, *Physical Review B* 86 (2012) 060201.

- [16] A. Abbasi, A. Dick, T. Hickel, J. Neugebauer. First-principles investigation of the effect of carbon on the stacking fault energy of Fe–C alloys, *Acta Materialia* 59 (2011) 3041-3048.
- [17] S. Kibey, J. Liu, M. Curtis, D. Johnson, H. Sehitoglu. Effect of nitrogen on generalized stacking fault energy and stacking fault widths in high nitrogen steels, *Acta materialia* 54 (2006) 2991-3001.
- [18] O.A. Zambrano. Stacking Fault Energy Maps of Fe–Mn–Al–C–Si Steels: Effect of Temperature, Grain Size, and Variations in Compositions, *Journal of Engineering Materials and Technology* 138 (2016) 041010-041010.
- [19] J. Hafner. Ab-initio simulations of materials using VASP: Density-functional theory and beyond, *Journal of computational chemistry* 29 (2008) 2044-2078.
- [20] P.E. Blöchl. Projector augmented-wave method, *Physical Review B* 50 (1994) 17953.
- [21] G. Kresse, D. Joubert. From ultrasoft pseudopotentials to the projector augmented-wave method, *Physical Review B* 59 (1999) 1758.
- [22] J.P. Perdew, K. Burke, M. Ernzerhof. Generalized gradient approximation made simple, *Physical review letters* 77 (1996) 3865.
- [23] D.M. Ceperley, B. Alder. Ground state of the electron gas by a stochastic method, *Physical Review Letters* 45 (1980) 566.
- [24] Y. Nishihara, Y. Nakajima, A. Akashi, N. Tsujino, E. Takahashi, K.-i. Funakoshi, Y. Higo. Isothermal compression of face-centered cubic iron, *American Mineralogist* 97 (2012) 1417-1420.
- [25] J.A. Zimmerman, H. Gao, F.F. Abraham. Generalized stacking fault energies for embedded atom FCC metals, *Modelling and Simulation in Materials Science and Engineering* 8 (2000) 103.
- [26] V. Vitek. Intrinsic stacking faults in body-centred cubic crystals, *Philosophical Magazine* 18 (1968) 773-786.
- [27] M. Beyramali Kivy, M. Asle Zaeem. Generalized stacking fault energies, ductilities, and twinnabilities of CoCrFeNi-based face-centered cubic high entropy alloys, *Scripta Materialia* 139 (2017) 83-86.
- [28] J. Wang, H. Huang. Shockley partial dislocations to twin: another formation mechanism and generic driving force, *Applied physics letters* 85 (2004) 5983-5985.
- [29] J.G. Lee. *Computational materials science: an introduction*, Crc Press, 2011.

- [30] H. Fjellvåg, B.C. Hauback, T. Vogt, S. Stølen. Monoclinic nearly stoichiometric wüstite at low temperatures, *American Mineralogist* 87 (2002) 347-349.
- [31] D.R. Lide. CRC handbook of chemistry and physics, CRC press, 2004.
- [32] Y.-K. Lee, C. Choi. Driving force for $\gamma \rightarrow \epsilon$ martensitic transformation and stacking fault energy of γ in Fe-Mn binary system, *Metallurgical and Materials Transactions A* 31 (2000) 355-360.
- [33] J. Nakano. A thermo-mechanical correlation with driving forces for hcp martensite and twin formations in the Fe-Mn-C system exhibiting multicomposition sets, *Science and Technology of Advanced Materials* (2016).
- [34] S.W. Lee, H.-C. Lee. The mechanical stability of austenite and cryogenic toughness of ferritic Fe-Mn-Al Alloys, *Metallurgical Transactions A* 24 (1993) 1333-1343.
- [35] K. Datta, R. Delhez, P. Bronsveld, J. Beyer, H. Geijselaers, J. Post. A low-temperature study to examine the role of ϵ -martensite during strain-induced transformations in metastable austenitic stainless steels, *Acta materialia* 57 (2009) 3321-3326.
- [36] P. Brofman, G. Ansell. On the effect of carbon on the stacking fault energy of austenitic stainless steels, *Metallurgical and Materials Transactions A* 9 (1978) 879-880.
- [37] M. Koyama, T. Sawaguchi, K. Tsuzaki. Selective appearance of ϵ -martensitic transformation and dynamic strain aging in Fe-Mn-C austenitic steels, *Philosophical Magazine* 92 (2012) 3051-3063.
- [38] G. Lehnhoff, K. Findley. The Martensitic Transformation and Strain-Hardening Behavior of Austenitic Steels During Fatigue and Tensile Loading, *JOM* 66 (2014) 756-764.
- [39] O. Grässel, L. Krüger, G. Frommeyer, L. Meyer. High strength Fe-Mn-(Al, Si) TRIP/TWIP steels development—properties—application, *International Journal of Plasticity* 16 (2000) 1391-1409.
- [40] S. Cotes, M. Sade, A.F. Guillermet. Fcc/Hcp martensitic transformation in the Fe-Mn system: Experimental study and thermodynamic analysis of phase stability, *Metallurgical and Materials Transactions A* 26 (1995) 1957-1969.
- [41] J. Han, A.K. da Silva, D. Ponge, D. Raabe, S.-M. Lee, Y.-K. Lee, S.-I. Lee, B. Hwang. The effects of prior austenite grain boundaries and microstructural morphology on the impact toughness of intercritically annealed medium Mn steel, *Acta Materialia* 122 (2017) 199-206

APPENDIX B.

DETAILS OF FIRST PRINCIPLES CALCULATIONS AND SUPPLEMENTAL
INFORMATION

First principle approach including DFT and *ab initio* molecular dynamics (AIMD) were utilized in this Ph.D. project to investigate the phase stabilities, surface energies and generalized stacking fault energies of different studied HEAs. Vienna ab initio simulation package (VASP) v.5.3.3 available on the extreme science and engineering discovery environment (XSEDE) were used to perform the calculations. Projector augmented wave (PAW) potentials [1, 2], instead of ultra-soft pseudopotentials, and the generalized gradient approximation (GGA) [3, 4] were used to enhance the accuracy of the calculations. Depending on the objective of the tasks, different structures with various lattice constants and atomic/elemental distributions were considered.

In order to calculate the phase stabilities to study the phase formations in AlFeCoNiCu HEAs, formation energies of different crystal structures including fcc, bcc and hcp were calculated applying DFT simulations. Total number of 96 atoms and 6x6x6 Monkhorst pack K-points mesh were considered. The unit-cell sizes were changed by changing the lattice constants to find the equilibrium lattice (the cell-size with minimum formation energy). For instance, for equi-atomic FeCoCu, 3 unit-cells of fcc, bcc and hcp crystal structures were considered and then the supercell were made based on the minimum required unit-cells. For fcc, bcc and hcp structures, unit-cells with 8 to 343 Å³, 3.38 to 216 Å³, and 5.5 to 104.5 Å³ were considered respectively. The atoms of the alloying elements were randomly distributed in the supercells manually. To increase the reliability of the results, different atomic positions for each element were also considered. The structures were relaxed (ionic relaxation at each particular volume size by allowing calculating forces, stress tensors ionic positions) until the ionic optimization convergence was within 0.001 eV/atom, and then simulations were converged considering the quasi-

Newton algorithm and Fermi smearing [5]. Using the same sampling K-points technique, the AIMD calculations are more computationally expensive compared to DFT simulations, less number of total atoms was used generally. It should be mentioned that since the Gamma point (center of the Brillion zone) is not considered as a special point, the AIMD calculations were not done on Gamma point only and instead, K-meshing was considered to be consistent with the DFT calculations. This increased the intensity and cost of the calculations, therefore 40 atoms were considered. Before performing the AIMD calculations, all the structures were relaxed using DFT calculations. NPT (constant number of atoms, iso-bar and iso-thermal) ensemble simulations were done considering Parinello-Rahman dynamics with Langevin thermostat (allowing cell shape and cell volume variations) [6-8]. The heating rate of $\sim 10^{14}$ K/sec was assumed for the AIMD calculations.

To study the plastic deformation mechanisms of CoCrFeNi-based HEAs, fcc supercells along $[111]$, $[\bar{2}11]$ and $[0\bar{1}1]$ axes consisting of 108 atoms (9 planes along $[111]$ and 12 atoms on each plane) were built. DFT calculations considering PAW potentials were performed, and exchange correlation functions were analyzed using the Perdew-Burke-Ernzerhof (PBE) GGA. Different lattice constants (3.56 Å, 3.58 Å, 3.59 Å and 3.60 Å) were assumed for different HEA compositions based on the experimental measurements available in the literature. The stacking faults were imposed to the defect-free fcc structure by a rigid displacement of the atoms above the stacking fault plane along $\langle 211 \rangle$ direction within $\{111\}$ slip plane [9, 10], which results in a $b_p = 1/6 \langle 211 \rangle_{\{111\}}$ partial Burgers vector (a Shockley partial dislocation) [11-14]. Two $b_p = 1/6 \langle 211 \rangle_{\{111\}}$ Shockley partial dislocations form a $a/2 \langle 110 \rangle$ perfect dislocation. An unstable stacking

fault (USF) forms due to the shear displacement through half of that Burgers vector, $\gamma_{USF} = a/2\langle 211 \rangle\{111\}$ [15]. Utilizing the DFT explicit approach for non-magnetic state, fault energies were calculated to be the total formation energy difference between defect-free lattice and faulted lattice per unit area:

$$FE \text{ (eV / m}^2\text{)} = \frac{E_0 - E_f}{A}, \quad (1)$$

where FE is the fault energy (USFE, ISFE, or UTE), E_0 (eV) is the formation energy of the perfect undistorted lattice, E_f (eV) is the total energy of the sheared lattice, and A is the area perpendicular to the stacking fault [12, 16]. When different layers along $[\bar{2}_{11}]$ direction within (111) slip plane were considered as fault planes, the calculated GSFE curve was altered due to different compositions of the fault planes. The surface energies were calculated by using defect-free supercells with an addition of $3a$ vacuum on top of the (111) plane. Then the difference between the perfect supercell and supercell with vacuum on top per unit area on (111) plane was the calculated surface energy. In addition to different stacking fault planes, different random atomic positions in the fcc supercells was also considered to increase the reliabilities of the results. All the structures including defect free and also faulted supercells were relaxed (ionic relaxation for each supercell by allowing calculating forces, stress tensors ionic positions) until the ionic optimization convergence was within 0.001 eV/atom, and then simulations were converged considering the quasi-Newton algorithm and Fermi smearing. The visualized illustrations of the supercells and generalized stacking fault configurations can be found in Figure C.2, C.3 and C.4.

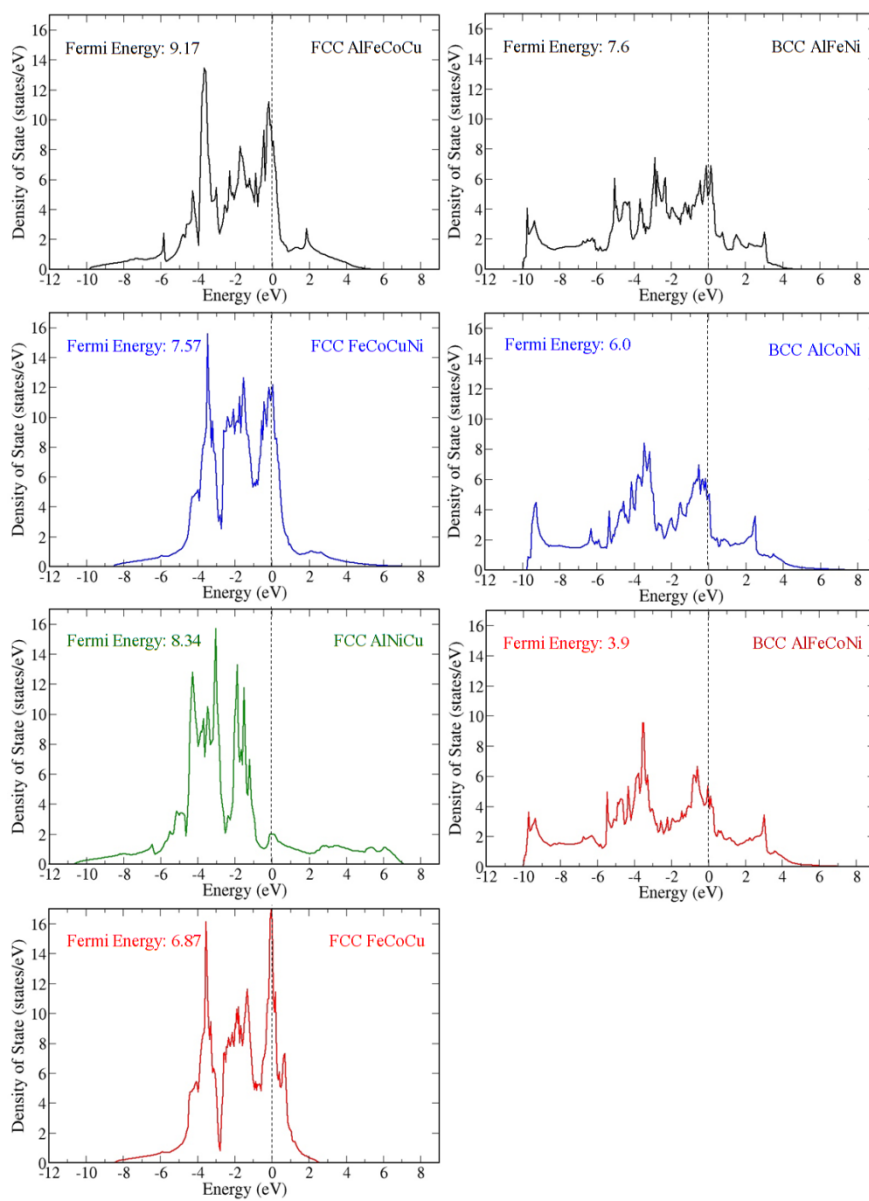


Figure C.1. Calculated total density of states of the selected crystals in AlFeCoNiCu HEA, for the Paper I

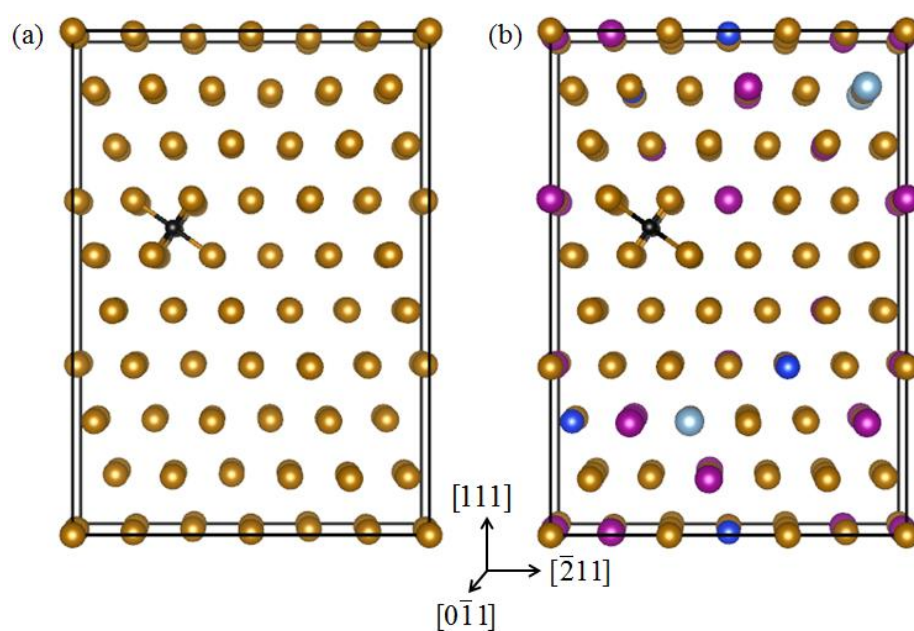


Figure C.2. Schematic supercells of Fe-Mn-Si-Al-C high strength steels for (a) single C (b) single C in the experimental composition. Brown, purple, dark blue, light blue and black indicate Fe, Mn, Si, Al and C respectively. The GSFPE results considering supercells like these two (108 atoms) are presented in Figure B.2.

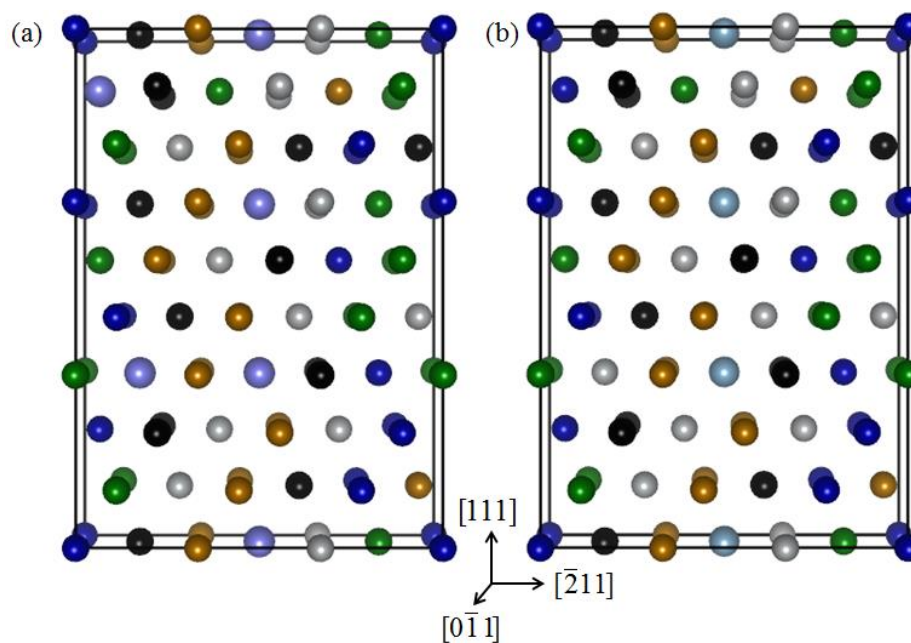


Figure C.3. Schematic supercells for (a) single $\text{CoCrFeNiCuTi}_{0.5}$ (b) $\text{CoCrFeNiCuAl}_{0.3}$ for Paper II. Green, black, grey, brown, dark blue, light blue and light purple indicate Cu, Cr, Ni, Fe, Co, Al and Ti respectively. These supercells consist of 108 atoms.

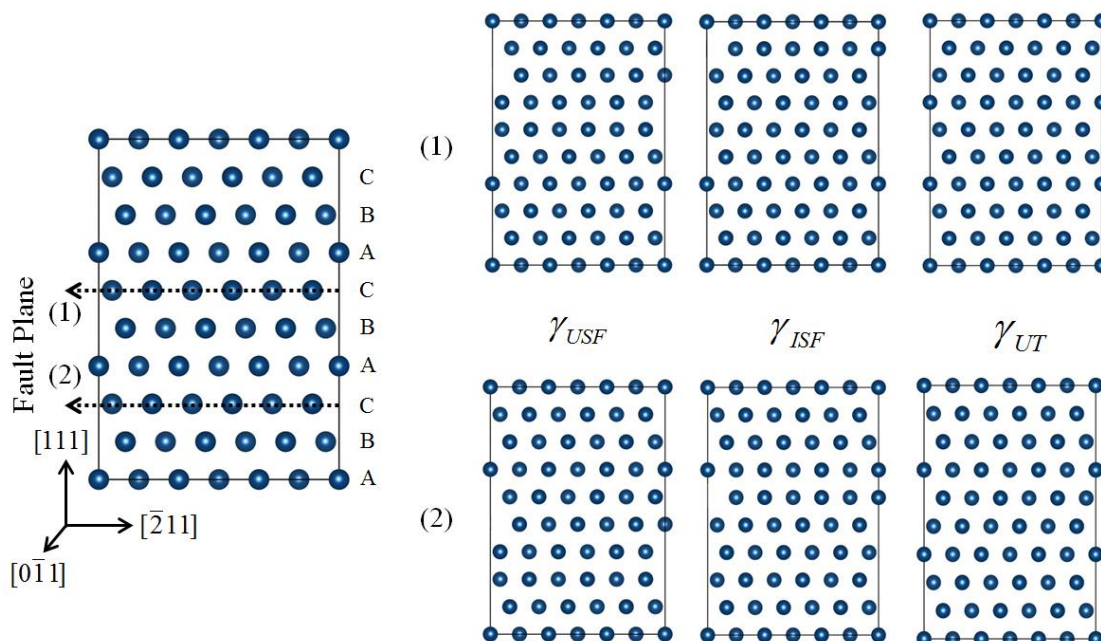


Figure C.4. Schematic fcc supercells for GSFE calculations considering two different planes as stacking fault planes and their corresponding unstable stacking fault, intrinsic stacking fault and unstable twinning configurations, for Paper II.

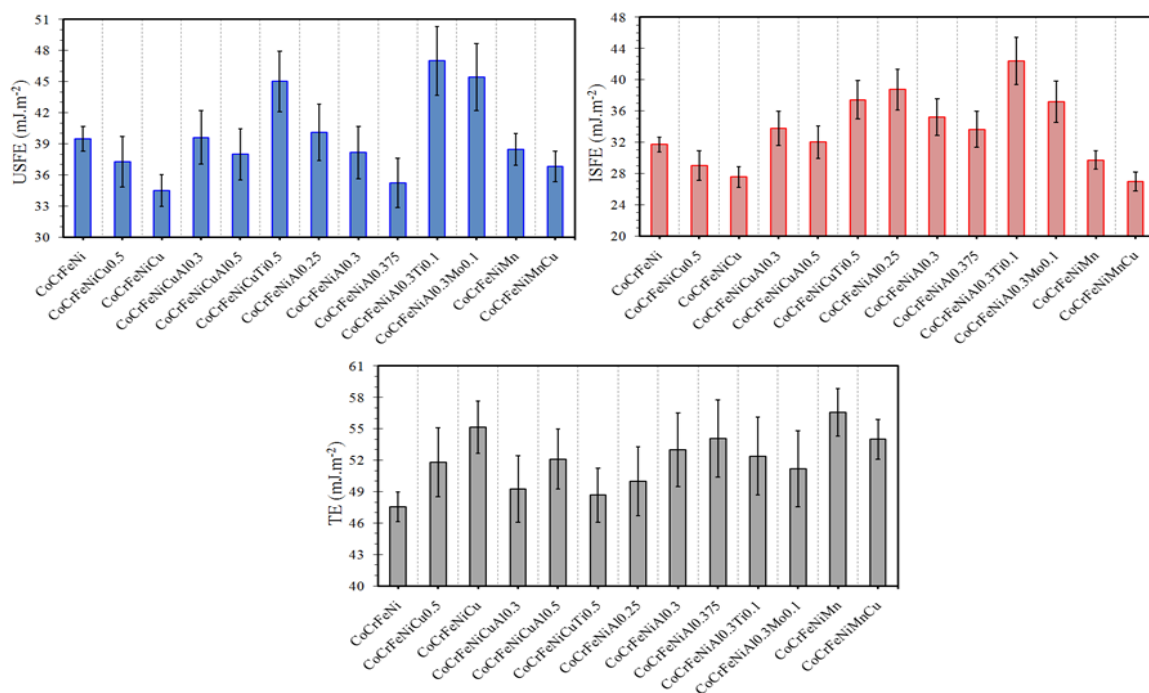


Figure C.5. Calculated generalized stacking fault energies for Paper II.

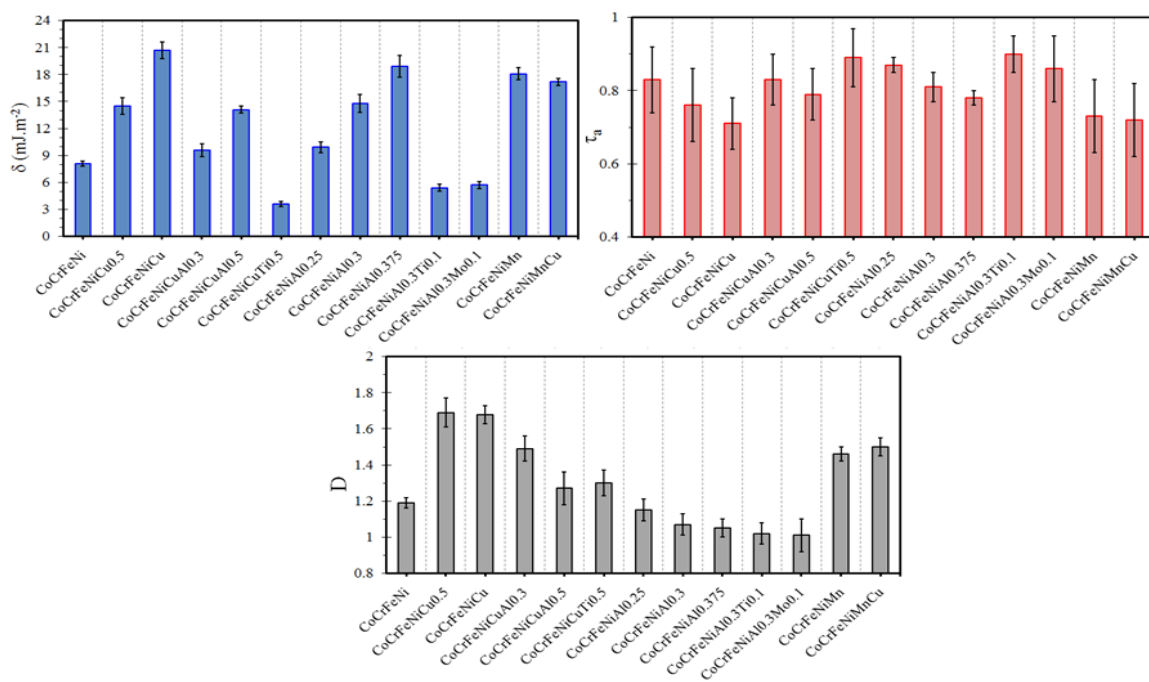


Figure C.6. Calculated relative barrier height, twinnability and Rice criterion ductility for Paper II.

REFERENCES

- [1] P. E. Blöchl, "Projector augmented-wave method," *Physical Review B*, vol. 50, p. 17953, 1994.
- [2] G. Kresse and D. Joubert, "From ultrasoft pseudopotentials to the projector augmented-wave method," *Physical Review B*, vol. 59, p. 1758, 1999.
- [3] J. P. Perdew, K. Burke, and M. Ernzerhof, "Generalized gradient approximation made simple," *Physical review letters*, vol. 77, p. 3865, 1996.
- [4] D. M. Ceperley and B. Alder, "Ground state of the electron gas by a stochastic method," *Physical Review Letters*, vol. 45, p. 566, 1980.
- [5] G. Kresse, O. Marsman, and J. Furthmüller, "VASP the guide," <http://cms.mpi.univie.ac.at/vasp/vasp.pdf> Retrieved April, 2016.
- [6] M. P. Allen and D. J. Tildesley, *Computer simulation of liquids*: Oxford university press, 1989.
- [7] M. Parrinello and A. Rahman, "Polymorphic transitions in single crystals: A new molecular dynamics method," *Journal of Applied physics*, vol. 52, pp. 7182-7190, 1981.
- [8] G. Kresse and O. Lebacqz, "Vasp manual," ed, 2013.
- [9] J. A. Zimmerman, H. Gao, and F. F. Abraham, "Generalized stacking fault energies for embedded atom FCC metals," *Modelling and Simulation in Materials Science and Engineering*, vol. 8, p. 103, 2000.
- [10] V. Vitek, "Intrinsic stacking faults in body-centred cubic crystals," *Philosophical Magazine*, vol. 18, pp. 773-786, 1968.
- [11] K. Limmer, J. Medvedeva, D. Van Aken, and N. Medvedeva, "Ab initio simulation of alloying effect on stacking fault energy in fcc Fe," *Computational Materials Science*, vol. 99, pp. 253-255, 2015.
- [12] E. Asadi, M. A. Zaeem, A. Moitra, and M. A. Tschopp, "Effect of vacancy defects on generalized stacking fault energy of fcc metals," *Journal of Physics: Condensed Matter*, vol. 26, p. 115404, 2014.
- [13] A. Das, "Revisiting stacking fault energy of steels," *Metallurgical and Materials Transactions A*, vol. 47, pp. 748-768, 2016.

BIBLIOGRAPHY

- [1] D. Miracle and O. Senkov, "A critical review of high entropy alloys and related concepts," *Acta Materialia*, vol. 122, pp. 448-511, 2017.
- [2] M. B. Kivy, M. A. Zaeem, and S. Lekakh, "Investigating phase formations in cast AlFeCoNiCu high entropy alloys by combination of computational modeling and experiments," *Materials & Design*, 2017.
- [3] S. Guo, C. Ng, J. Lu, and C. Liu, "Effect of valence electron concentration on stability of fcc or bcc phase in high entropy alloys," *Journal of applied physics*, vol. 109, p. 103505, 2011.
- [4] F. Zhang, C. Zhang, S. L. Chen, J. Zhu, W. S. Cao, and U. R. Kattner, "An understanding of high entropy alloys from phase diagram calculations," *CALPHAD*, vol. 45, pp. 1-10, 2014.
- [5] Y. Zhang, T. Zuo, Y. Cheng, and P. K. Liaw, "High-entropy alloys with high saturation magnetization, electrical resistivity, and malleability," *Scientific reports*, vol. 3, 2013.
- [6] C. Zhang, F. Zhang, S. Chen, and W. Cao, "Computational thermodynamics aided high-entropy alloy design," *Jom*, vol. 64, pp. 839-845, 2012.
- [7] C. Lee, Y. Chen, C. Hsu, J. Yeh, and H. Shih, "The Effect of Boron on the Corrosion Resistance of the High Entropy Alloys Al_{0.5}CoCrCuFeNiB_x," *Journal of the Electrochemical Society*, vol. 154, pp. C424-C430, 2007.
- [8] S.-T. Chen, W.-Y. Tang, Y.-F. Kuo, S.-Y. Chen, C.-H. Tsau, T.-T. Shun, *et al.*, "Microstructure and properties of age-hardenable Al_xCrFe_{1.5}MnNi_{0.5} alloys," *Materials science & engineering. A, Structural materials: properties, microstructure and processing*, vol. 527, pp. 5818-5825, 2010.
- [9] T.-T. Shun and Y.-C. Du, "Microstructure and tensile behaviors of FCC Al_{0.3}CoCrFeNi high entropy alloy," *Journal of Alloys and Compounds*, vol. 479, pp. 157-160, 2009.
- [10] M.-H. Chuang, M.-H. Tsai, W.-R. Wang, S.-J. Lin, and J.-W. Yeh, "Microstructure and wear behavior of Al_xCo_{1.5}CrFeNi_{1.5}Ti_y high-entropy alloys," *Acta Materialia*, vol. 59, pp. 6308-6317, 2011.
- [11] C. Huang, Y. Zhang, J. Shen, and R. Vilar, "Thermal stability and oxidation resistance of laser clad TiVCrAlSi high entropy alloy coatings on Ti-6Al-4V alloy," *Surface and Coatings Technology*, vol. 206, pp. 1389-1395, 2011.

- [12] X.-W. Qiu, "Microstructure and properties of AlCrFeNiCoCu high entropy alloy prepared by powder metallurgy," *Journal of Alloys and Compounds*, vol. 555, pp. 246-249, 2013.
- [13] A. Durga, K. H. Kumar, and B. Murty, "Phase Formation in Equiatomic High Entropy Alloys: CALPHAD Approach and Experimental Studies," *Transactions of the Indian Institute of Metals*, vol. 65, pp. 375-380, 2012.
- [14] M. Yao, "Mechanical Behavior of High Entropy Alloys," *Max-Planck Institute*, vol. Dusseldorf, 2012.
- [15] L. Tsao, C. Chen, and C. Chu, "Age hardening reaction of the Al 0.3CrFe 1.5MnNi 0.5 high entropy alloy," *Materials & Design*, vol. 36, pp. 854-858, 2012.
- [16] M.-H. Tsai and J.-W. Yeh, "High-entropy alloys: a critical review," *Materials Research Letters*, vol. 2, pp. 107-123, 2014.
- [17] M. B. Kiviy and M. A. Zaeem, "Generalized stacking fault energies, ductilities, and twinnabilities of CoCrFeNi-based face-centered cubic high entropy alloys," *Scripta Materialia*, vol. 139, pp. 83-86, 2017.
- [18] J.-W. Yeh, "Alloy Design Strategies and Future Trends in High-Entropy Alloys," *JOM*, vol. 65, pp. 1759-1771, 2013.
- [19] Y. Zhang, T. T. Zuo, Z. Tang, M. C. Gao, K. A. Dahmen, P. K. Liaw, *et al.*, "Microstructures and properties of high-entropy alloys," *Progress in Materials Science*, vol. 61, pp. 1-93, 2014.
- [20] B. Gludovatz, A. Hohenwarter, D. Catoor, E. H. Chang, E. P. George, and R. O. Ritchie, "A fracture-resistant high-entropy alloy for cryogenic applications," *Science*, vol. 345, pp. 1153-1158, 2014.
- [21] Z. Li, C. C. Tasan, H. Springer, B. Gault, and D. Raabe, "Interstitial atoms enable joint twinning and transformation induced plasticity in strong and ductile high-entropy alloys," *Scientific reports*, vol. 7, p. 40704, 2017.
- [22] U. Hsu, U. Hung, J. Yeh, S. Chen, Y. Huang, and C. Yang, "Alloying behavior of iron, gold and silver in AlCoCrCuNi-based equimolar high-entropy alloys," *Materials Science and Engineering: A*, vol. 460, pp. 403-408, 2007.
- [23] Y.-S. Huanga, L. Chenb, H.-W. Luic, M.-H. Caid, and J.-W. Yeh, "Microstructure, hardness, resistivity and thermal stability of sputtered oxide films of AlCoCrCu0.5NiFe high-entropy alloy," 2007.
- [24] T.-K. Chen, T. Shun, J. Yeh, and M. Wong, "Nanostructured nitride films of multi-element high-entropy alloys by reactive DC sputtering," *Surface and Coatings Technology*, vol. 188, pp. 193-200, 2004.

- [25] L. Wang, C. Chen, J. Yeh, and S. Ke, "The microstructure and strengthening mechanism of thermal spray coating $\text{Ni}_x\text{Co}_{0.6}\text{Fe}_{0.2}\text{Cr}_{0.2}\text{Si}_{0.2}\text{AlTi}_{0.2}$ high-entropy alloys," *Materials Chemistry and Physics*, vol. 126, pp. 880-885, 2011.
- [26] O. Senkov, G. Wilks, D. Miracle, C. Chuang, and P. Liaw, "Refractory high-entropy alloys," *Intermetallics*, vol. 18, pp. 1758-1765, 2010.
- [27] C. Liu, H. Wang, S. Zhang, H. Tang, and A. Zhang, "Microstructure and oxidation behavior of new refractory high entropy alloys," *Journal of Alloys and Compounds*, vol. 583, pp. 162-169, 2014.
- [28] M. F. del Grosso, G. Bozzolo, and H. O. Mosca, "Determination of the transition to the high entropy regime for alloys of refractory elements," *Journal of Alloys and Compounds*, vol. 534, pp. 25-31, 2012.
- [29] O. Senkov, S. Senkova, C. Woodward, and D. Miracle, "Low-density, refractory multi-principal element alloys of the Cr–Nb–Ti–V–Zr system: Microstructure and phase analysis," *Acta Materialia*, vol. 61, pp. 1545-1557, 2013.
- [30] X. Yang and Y. Zhang, "Prediction of high-entropy stabilized solid-solution in multi-component alloys," *Materials Chemistry and Physics*, vol. 132, pp. 233-238, 2012.
- [31] O. Senkov, G. Wilks, J. Scott, and D. Miracle, "Mechanical properties of $\text{Nb}_{25}\text{Mo}_{25}\text{Ta}_{25}\text{W}_{25}$ and $\text{V}_{20}\text{Nb}_{20}\text{Mo}_{20}\text{Ta}_{20}\text{W}_{20}$ refractory high entropy alloys," *Intermetallics*, vol. 19, pp. 698-706, 2011.
- [32] O. Senkov, S. Senkova, and C. Woodward, "Effect of aluminum on the microstructure and properties of two refractory high-entropy alloys," *Acta Materialia*, vol. 68, pp. 214-228, 2014.
- [33] C. Hsu, "Effect of Aluminum Content on Microstructure and Mechanical Properties of $\text{Al}_x\text{CoCrFeMo}_{0.5}\text{Ni}$ High-Entropy Alloys," *JOM*, vol. 65, 2013.
- [34] F. Wang and Y. Zhang, "Effect of Co addition on crystal structure and mechanical properties of $\text{Ti}_{0.5}\text{CrFeNiAlCo}$ high entropy alloy," *Materials Science and Engineering: A*, vol. 496, pp. 214-216, 2008.
- [35] T.-T. Shun, C.-H. Hung, and C.-F. Lee, "The effects of secondary elemental Mo or Ti addition in $\text{Al}_{10.3}\text{CoCrFeNi}$ high-entropy alloy on age hardening at 700°C ," *Journal of Alloys and Compounds*, vol. 495, pp. 55-58, 2010.
- [36] H. Fang, K. Chen, X. Chen, L. Huang, G. Peng, and B. Huang, "Effect of Zr, Cr and Pr additions on microstructures and properties of ultra-high strength Al-Zn-Mg-Cu alloys," *Materials Science and Engineering: A*, vol. 528, pp. 7606-7615, 2011.

- [37] J. Cheng, X. Liang, and B. Xu, "Effect of Nb addition on the structure and mechanical behaviors of CoCrCuFeNi high-entropy alloy coatings," *Surface and Coatings Technology*, 2013.
- [38] C.-Y. Hsu, C.-C. Juan, S.-T. Chen, T.-S. Sheu, J.-W. Yeh, and S.-K. Chen, "Phase Diagrams of High-Entropy Alloy System Al-Co-Cr-Fe-Mo-Ni," *JOM*, vol. 65, pp. 1829-1839, 2013.
- [39] C.-Y. Hsu, T.-S. Sheu, J.-W. Yeh, and S.-K. Chen, "Effect of iron content on wear behavior of AlCoCrFe_xMo 0.5 Ni high-entropy alloys," *Wear*, vol. 268, pp. 653-659, 2010.
- [40] C.-C. Juan, C.-Y. Hsu, C.-W. Tsai, W.-R. Wang, T.-S. Sheu, J.-W. Yeh, *et al.*, "On microstructure and mechanical performance of AlCoCrFeMo 0.5 Ni_x high-entropy alloys," *Intermetallics*, vol. 32, pp. 401-407, 2013.
- [41] Z. Wang, I. Baker, Z. Cai, S. Chen, J. D. Poplawsky, and W. Guo, "The effect of interstitial carbon on the mechanical properties and dislocation substructure evolution in Fe 40.4 Ni 11.3 Mn 34.8 Al 7.5 Cr 6 high entropy alloys," *Acta Materialia*, vol. 120, pp. 228-239, 2016.
- [42] H. Zhang, Y. Pan, and Y.-Z. He, "Synthesis and characterization of FeCoNiCrCu high-entropy alloy coating by laser cladding," *Materials & Design*, vol. 32, pp. 1910-1915, 2011.
- [43] B. A. Welk, R. E. Williams, G. B. Viswanathan, M. A. Gibson, P. K. Liaw, and H. L. Fraser, "Nature of the interfaces between the constituent phases in the high entropy alloy CoCrCuFeNiAl," *Ultramicroscopy*, vol. 134, pp. 193-199, 2013.
- [44] H. R. Sistla, J. W. Newkirk, and F. F. Liou, "Effect of Al/Ni ratio, heat treatment on phase transformations and microstructure of Al_xFeCoCrNi_{2-x} (x= 0.3, 1) high entropy alloys," *Materials & Design*, vol. 81, pp. 113-121, 2015.
- [45] H. Zhang, Y. Pan, Y. He, and H. Jiao, "Microstructure and properties of 6FeNiCoSiCrAlTi high-entropy alloy coating prepared by laser cladding," *Applied Surface Science*, vol. 257, pp. 2259-2263, 2011.
- [46] X. Ye, M. Ma, Y. Cao, W. Liu, X. Ye, and Y. Gu, "The Property Research on High-entropy Alloy Al_xFeCoNiCuCr Coating by Laser Cladding," *Physics Procedia*, vol. 12, pp. 303-312, 2011.
- [47] S. Ma, S. Zhang, M. Gao, P. Liaw, and Y. Zhang, "A Successful Synthesis of the CoCrFeNiAl_{0.3} Single-Crystal, High-Entropy Alloy by Bridgman Solidification," *JOM*, vol. 65, pp. 1751-1758, 2013.

- [48] X.-W. Qiu, Y.-P. Zhang, L. He, and C.-g. Liu, "Microstructure and corrosion resistance of AlCrFeCuCo high entropy alloy," *Journal of Alloys and Compounds*, vol. 549, pp. 195-199, 2013.
- [49] M. C. Gao and D. E. Alman, "Searching for next single-phase high-entropy alloy compositions," *Entropy*, vol. 15, pp. 4504-4519, 2013.
- [50] D. B. Miracle, J. D. Miller, O. N. Senkov, C. Woodward, M. D. Uchic, and J. Tiley, "Exploration and Development of High Entropy Alloys for Structural Applications," *Entropy*, vol. 16, pp. 494-525, 2014.
- [51] U. R. Kattner, "The thermodynamic modeling of multicomponent phase equilibria," *JOM*, vol. 49, pp. 14-19, 1997.
- [52] R. Raghavan, K. Hari Kumar, and B. Murty, "Analysis of phase formation in multi-component alloys," *Journal of Alloys and Compounds*, vol. 544, pp. 152-158, 2012.
- [53] C. Ng, S. Guo, J. Luan, S. Shi, and C. Liu, "Entropy-driven phase stability and slow diffusion kinetics in an Al_{0.5}CoCrCuFeNi high entropy alloy," *Intermetallics*, vol. 31, pp. 165-172, 2012.
- [54] F. Otto, Y. Yang, H. Bei, and E. P. George, "Relative effects of enthalpy and entropy on the phase stability of equiatomic high-entropy alloys," *Acta Materialia*, vol. 61, pp. 2628-2638, 2013.
- [55] S. Wang, "Atomic Structure Modeling of Multi-Principal-Element Alloys by the Principle of Maximum Entropy," *Entropy*, vol. 15, pp. 5536-5548, 2013.
- [56] L. Xie, P. Brault, A.-L. Thomann, and J.-M. Bauchire, "AlCoCrCuFeNi high entropy alloy cluster growth and annealing on silicon: A classical molecular dynamics simulation study," *Applied Surface Science*, vol. 285, pp. 810-816, 2013.
- [57] P. Liaw, T. Egami, and Y. Zhang, "Title," unpublished].
- [58] S.-W. Kao, J.-W. Yeh, and T.-S. Chin, "Rapidly solidified structure of alloys with up to eight equal-molar elements—a simulation by molecular dynamics," *Journal of Physics: Condensed Matter*, vol. 20, p. 145214, 2008.
- [59] M. Widom, W. P. Huhn, S. Maiti, and W. Steurer, "Hybrid Monte Carlo/molecular dynamics simulation of a refractory metal high entropy alloy," *Metallurgical and Materials Transactions A*, vol. 45, pp. 196-200, 2014.

- [60] G. Kresse and J. Furthmüller, "Efficiency of ab-initio total energy calculations for metals and semiconductors using a plane-wave basis set," *Computational materials science*, vol. 6, pp. 15-50, 1996.
- [61] W. Kohn and L. J. Sham, "Self-consistent equations including exchange and correlation effects," *Physical review*, vol. 140, p. A1133, 1965.
- [62] J. P. Perdew, J. A. Chevary, S. H. Vosko, K. A. Jackson, M. R. Pederson, D. J. Singh, *et al.*, "Atoms, molecules, solids, and surfaces: Applications of the generalized gradient approximation for exchange and correlation," *Physical Review B*, vol. 46, p. 6671, 1992.
- [63] S. Middleburgh, D. King, G. Lumpkin, M. Cortie, and L. Edwards, "Segregation and migration of species in the CrCoFeNi high entropy alloy," *Journal of Alloys and Compounds*, 2014.
- [64] Z.-s. NONG, J.-c. ZHU, H.-l. YU, and Z.-h. LAI, "First principles calculation of intermetallic compounds in FeTiCoNiVCrMnCuAl system high entropy alloy," *Transactions of Nonferrous Metals Society of China*, vol. 22, pp. 1437-1444, 2012.
- [65] F. Tian, L. Varga, N. Chen, S. Jiang, and L. Vitos, "Ab initio design of elastically isotropic TiZrNbMoVx high-entropy alloys," *Journal of Alloys and Compounds*, vol. 599, pp. 19-25, 2014 2014.
- [66] S. Huang, W. Li, S. Lu, F. Tian, J. Shen, E. Holmström, *et al.*, "Temperature dependent stacking fault energy of FeCrCoNiMn high entropy alloy," *Scripta Materialia*, vol. 108, pp. 44-47, 2015.
- [67] P. Richet, "Viscosity and configurational entropy of silicate melts," *Geochimica et Cosmochimica Acta*, vol. 48, pp. 471-483, 1984.
- [68] A. G. Whittington, M. A. Bouhifd, and P. Richet, "Amorphous materials: Properties, structure, and durability. The viscosity of hydrous NaAlSi₃O₈ and granitic melts: Configurational entropy models," *American Mineralogist*, vol. 94, pp. 1-16, 2009.
- [69] C.-C. Tung, J.-W. Yeh, T.-t. Shun, S.-K. Chen, Y.-S. Huang, and H.-C. Chen, "On the elemental effect of AlCoCrCuFeNi high-entropy alloy system," *Materials letters*, vol. 61, pp. 1-5, 2007.
- [70] J.-M. Wu, S.-J. Lin, J.-W. Yeh, S.-K. Chen, Y.-S. Huang, and H.-C. Chen, "Adhesive wear behavior of Al_xCoCrCuFeNi high-entropy alloys as a function of aluminum content," *Wear*, vol. 261, pp. 513-519, 2006.

- [71] C.-M. Lin and H.-L. Tsai, "Equilibrium phase of high-entropy FeCoNiCrCu 0.5 alloy at elevated temperature," *Journal of Alloys and Compounds*, vol. 489, pp. 30-35, 2010.
- [72] X. Wang, Y. Zhang, Y. Qiao, and G. Chen, "Novel microstructure and properties of multicomponent CoCrCuFeNiTi_x alloys," *Intermetallics*, vol. 15, pp. 357-362, 2007.
- [73] H.-P. Chou, Y.-S. Chang, S.-K. Chen, and J.-W. Yeh, "Microstructure, thermophysical and electrical properties in Al_xCoCrFeNi (0 ≤ x ≤ 2) high-entropy alloys," *Materials Science and Engineering: B*, vol. 163, pp. 184-189, 2009.
- [74] T.-T. Shun, C.-H. Hung, and C.-F. Lee, "The effects of secondary elemental Mo or Ti addition in Al 0.3 CoCrFeNi high-entropy alloy on age hardening at 700 C," *Journal of Alloys and Compounds*, vol. 495, pp. 55-58, 2010.
- [75] B. Cantor, "Multicomponent and high entropy alloys," *Entropy*, vol. 16, pp. 4749-4768, 2014.

VITA

Mohsen Beyramali Kivy was born on March 21, 1986 in Khalkhal, Iran and raised in Tehran, Iran. Since his parents are retired teachers, Mohsen was always interested in being in school. He graduated from high school in 2004 with mathematics and physics major. He was qualified in a nationwide college entrance exam and attended University of Tehran, one of the most prestigious universities in the area. Mohsen graduate from School of Engineering, University of Tehran, in 2009 with a Bachelor of Science in Chemical Engineering. During his undergraduate studies, Mohsen worked on several projects as an undergraduate researcher. He was part of a team for designing and constructing a lab-scale shell & tube heat exchanger. He also worked on synthesizing and scaling-up a Zeolite based fluidized catalytic cracking catalyst in catalyst and nanostructure laboratory. In 2013, Mohsen was admitted for Ph.D. in Materials Science and Engineering, Missouri S&T. He commenced his work on his doctoral research project on experimental and first principle studies of high entropy alloys. During his Ph.D., Mohsen had experience on working as a lab instructor and an undergraduate course lecturer. In June 2017, he married Caitlin Kriewall, Ph.D. candidate in the Materials Science and Engineering Department, Missouri S&T. His Ph.D. in Materials Science and Engineering was awarded in December of 2017 from Missouri S&T.